DOCTOR OF PHILOSOPHY

Ab-initio and Experimental NEXAFS Spectroscopy Investigations of Graphene: growth and post-processing effects

Rojas Verastegui, Wudmir

Award date:
2018

Awarding institution:
Bangor University

[Link to publication](#)

Ab-initio and Experimental NEXAFS Spectroscopy Investigations of Graphene: growth and post-processing effects

By

Wudmir Yudy Rojas Verastegui

Submitted in partial fulfillment for the degree of
Doctor of Philosophy

College of Physical and Applied Sciences
School of Electronic Engineering

May 2018

To my parents Nery and Mavila, my sister Sadith,
my wife Hilda and our dear sons Dylan and Cedric.

Acknowledgements

My deepest gratitude to my parents, Mavila and Nery, for their infinite and unconditional support ever since I started my carrier in science as an undergraduate and even more when I made my decision to purse my doctoral degree after a long break away from research; I will gladly tell you both: mission accomplished Mum & Dad!. I thank my sister Sadith for her constant enthusiasm and support likewise. This last sentence of acknowledgment I have saved for my dear wife Hilda, and our beloved sons, Dylan and Cedric, to whom I express all my gratitude, love and admiration, and in particular, Cedric who arrived in the world when I was not present and became a source of joy and happiness. I could not complete this journey without their support, trust, and care, especially over the last six years since I started my Master's in Brazil away from them and from home.

<div align="right">

Wudmir Y. Rojas
Spring 2018, Bangor
Wales, United Kingdom

</div>

Abstract

Fully commercial exploitation of graphene properties through its integration in the Si-dominated electronic technologies needs to reach challenging growth and processing standards. Indeed, fabrication and subsequent processing of graphene using current methodologies, such as chemical vapor deposition oriented to industrial fabrication, require discriminating and assessing strain and corrugation in order to achieve practical use. For the first time, a combination of *ab initio* simulations and experimental hyperspectral near-edge X-ray absorption fine structure (NEXAFS) data was successfully employed to monitor mechanical deformation in graphene (i.e., strain and corrugation) at wafer-scale dimensions. Notably, this innovative assessment offers promise towards wafer-scale characterization to inform industrial manufacturing. To this end, the first study presented in this thesis examines the atomic sensitivity to corrugation of the dichroic ratio, orbital vector approximation, and unsupervised machine learning methods. Significantly, the orbital vector approach proved to be the method with the highest sensitivity as reflected by the measured α parameter, which also strongly depends on the frequency of the defects. In the second study of this thesis, a new methodology to assess strain with the aid of theoretical samples taken as standards is presented. The most significant results are its accurate strain estimation of chemical vapor deposition-grown graphene on Cu substrates and reasonably accurate estimation of transferred multilayers of graphene onto SiC substrates. In the last study, a method to simulate characteristic angle-resolved NEXAFS spectra (spectral fingerprints) of representative topological defects on graphene is presented and proves to effectively analyze the correlation between the spatial extent of the defect and its spectral fingerprints. This theoretical database of point defects can contribute to the analysis and interpretation of complex experimental spectroscopic data.

Contents

i

Publications

- W. Y. Rojas, A. D. Winter, J. G. Grote, S. S. Kim, R. R. Naik, A. D. Williams, C. Weiland, E. Principe, D. A. Fischer, S. Banerjee, D. Prendergast, E. M. Campo. *Strain and bond length dynamics upon growth and transfer of graphene by NEXAFS spectroscopy from first principles and experiment*. **Langmuir 2018, 34 (4), 1783-1794**.

- A. D. Winter, W. Y. Rojas, A. D. Williams, S. S. Kim, F. Ouchen, D. A. Fischer, C. Weiland, E. Principe, S. Banerjee, C. Huynh, R. R. Naik, Y. Liu, A. Mehta, J. Grote, D. Prendergast, and E. M. Campo.*Monitoring Deformation in Graphene Through Hyperspectral Synchrotron Spectroscopy to Inform Fabrication*. **The Journal of Physical Chemistry C 2017, 121 (29), 15653-15664**.

- E. M. Campo, D. Yates, B. Berson, W. Y. Rojas, A. D. Winter, M. Ananth, J. J. Santiago-Aviles, and E. M. Terentjev. *Tomography of Electrospun Carbon Nanotube Polymeric Blends by Focus Ion Beam: Alignment and Phase Separation Analysis from Multicontrast Electron Imaging*. **Macromolecular Materials and Engineering 2017**.

- W. Y. Rojas, D. Prendergast, A.G. Kuzne, A. Mehta, S. Banerjee and E. M. Campo. *Building databases of topological defect fingerprints on graphene by NEXAFS spectroscopy: Theory and Data*. **In preparation.**

- A. D. Winter, W. Y. Rojas, E. Larios, P. Albrech, T. Bossing, S. Banerjee, D. Prendergast and E. M. Campo. *Probing on the Molecular Bonding of DMSO-DiI-*

MWCNT: a route to Biological MWCNT Surface Modification Examined through Synchrotron Spectroscopies. **In preparation.**

Authorship and Collaborations

This thesis was the result of a joint effort among external collaborators and members of the Laboratory for Matter Dynamics whose corresponding contributions are specified here. W. Y. Rojas performed all the calculations, assisted Dr. E. M. Campo on the designing of the theoretical "experiments" and handled all the data treatment, inclusive of the ongoing curation procedures, in cooperation with NIST. He also co-wrote the publications he authored. Calculations were also the result of a close collaborative with Dr. David Prendergast at the Molecular Foundry in Lawrence Berkeley National Laboratory and Professor Dr. Sarbajit Banerjee at Texas A&M.

Chapter 3

- Experimental samples were synthesized by Dr. A. Williams and and Dr. S. Kim, from Dr. James Grote's and Dr. Rajesh Naik's research groups, Air Force Research Lab, USA.

- NEXAFS Spectral normalization, calibration and background subtraction of experimental samples were performed by Dr. A. D. Winter, under the supervision of Dr. E. M. Campo, Laboratory for Matter Dynamics, Bangor University, UK.

- Experimental data treatment routine was performed by Dr. A. D. Winter in collaboration with W. Y. Rojas., under the supervision of Dr. E. M. Campo, Laboratory for Matter Dynamics, Bangor University, UK.

- Helium Ion Microscopy characterization performed by Dr. Chuong Huynh, Carl Zeiss Microscopy, USA.

- DBSCAN analysis was supervised by Dr. Y. Liu and Dr. Apurva Mehta's group at Stanford Synchrotron Radiation Laboratory, USA and Dr. E. M. Campo and executed by Dr. A. D. Winter and W. Y. Rojas.

Chapter 4

- Experimental samples were synthesized by Dr. A. Williams and and Dr. S. Kim, from Dr. James Grote's and Dr. Rajesh Naik's research groups, Air Force Research Lab, USA.

- NEXAFS Spectral normalization, calibration and background subtraction of experimental samples were performed by Dr. A. D. Winter, under the supervision of Dr. E. M. Campo, Laboratory for Matter Dynamics, Bangor University, UK.

- Helium Ion Microscopy characterization performed by Dr. Chuong Huynh, Carl Zeiss Microscopy, USA.

List of Figures

x

List of Tables

1

Introduction

1.1 Graphene

1.1.1 Definition, Electronic Structure and Basic Properties

Graphene is a two-dimensional crystal with unique physical and chemical properties caused by its reduced dimensionality—i.e., a one carbon atom thickness—in stark contrast with bulk materials. Carbon atoms in graphene are arranged in honeycomb lattice. Initial theoretical investigations of graphene have been reported in 1947 by Wallace.[1] This study developed despite the fact that a decade prior Landau and Peierls argued that two-dimensional materials would be impossible due to thermodynamic instability.[2,3] Wallace's pioneering work established some fundamental electronic properties of graphene such the electron-hole symmetry and the linear dispersion of band structures near the Dirac point. However, it was not until 2004 that A. Geim and K. Novoselov,[4] for the first time, successfully reported studies of electric transport on isolated graphene obtained by the micro-mechanical cleavage technique, i.e., mechanical exfoliation. Typically, the stacking of up to ten monolayers is still considered graphene.[5] As per today, graphene is still the most studied among 2D crystals. However, other types of 2D compounds have been studied recently, namely hexagonal boron nitride, transition metal di- and three-chalcogenides, phosphorene, monochalcogenides, and antimonene.[6]

The versatility of carbon atoms to form sp^2 orbitals as a result of hybridization between one s orbital and two p orbitals (p_x and p_y) is responsible for the hexagonal lattice in graphene through the sp^2-sp^2 bonding (σ bonding) whereas the non-hybridized p_z-p_z bonding (π bonding) with neighboring carbon atoms determine

the electronic properties in graphene, as schematically shown in Figure 1.1.
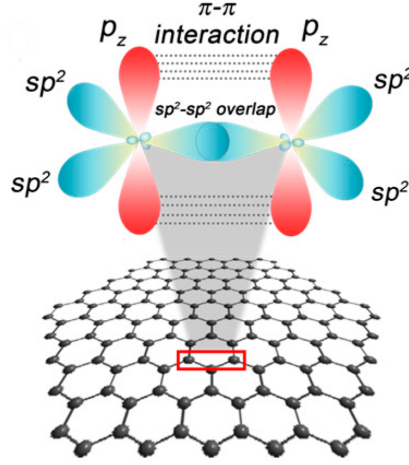
Figure 1.1: Schematic representation of covalent σ bonds between two sp^2 orbitals in pristine graphene along with π bonds between nearby p_z orbitals. Adapted from ref.[7]

The characteristic conductance of graphene has its origin in the hexagonal distribution of carbon atoms, in particular, the formation of valence and conduction bands by means of the π bonding and π^* antibonding bands that crossover at the unique Dirac point E_D,[1] as shown in Figure 1.2. This Dirac point, which in undoped graphene is equal to the Fermi energy E_F, takes place at the vertex of the Brillouin zone, corresponding to the high symmetry point K, as sketched in the inset of Figure 1.2 (shaded in grey). Graphene is defined as a zero-gap semiconductor and its approximately linear energy-momentum dispersion at the Dirac point E_D exhibited in its band structure—identified as the point where π^* and π bands touch each other (i.e., called Dirac's cone in a 3D representation of the graphene band structure). In fact, it is a common practice to neglect the contribution of σ bonding and σ^* antibonding states to the electronic properties of graphene in view of their large energy separation around the Fermi energy E_F.

Ever since the first isolation and subsequent experimental measurement of electrical properties of graphene supported in a SiO_2 substrate,[4] vast investigations have been conducted that reveal further stunning properties. In addition to the zero-band gap feature and the linear dispersion correlation exhibited by the charge carriers nearby the Dirac point up to concentrations of 10^{13} cm^{-2}, the quantum Hall effect was observed at room temperature.[4,5] This proved the behavior of charge car-
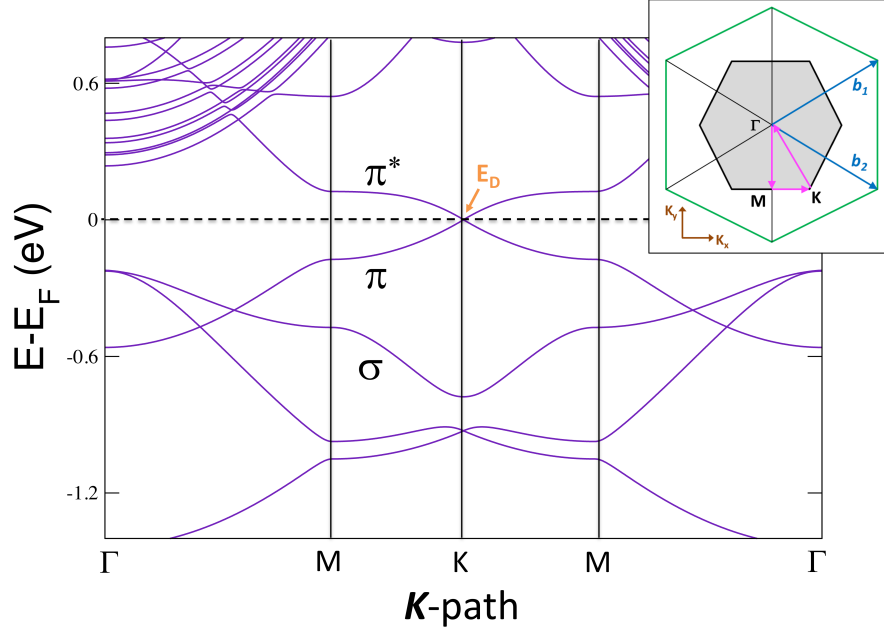
Figure 1.2: Density functional theory band structure of pristine graphene under the generalized gradient approximation (GGA). The inset displays the Brillouin zone (grey hexagon), the reciprocal lattice vectors (b_1 and b_2) and K-path along the high symmetry points Γ-M-K-Γ (arrows in magenta). Linear dispersion occurs near the Dirac point E_D and also $E_D = E_F$.

riers as massless relativistic particles, which in fact serves as an indication of quality.[8,9] The high carrier mobility at room temperature in exfoliated graphene is definitely the most attractive property, hence tagging graphene as the material of choice for the post-silicon industry. This tagging has developed despite its lack of a band gap necessary for logic electronic devices. Mobilities of 10–15k cm^{2}V^{-1}s^{-1} are usually reported in exfoliated graphene.[4,10] In addition, mobilities on the order of 200k cm^{2}V^{-1}s^{-1} have been reported when extrinsic disorders are eliminated.[11] These are clearly higher mobility values than 1.4k cm^{2}V^{-1}s^{-1} in Si and 8.5k cm^{2}V^{-1}s^{-1} in GaAs.[12] Moreover, epitaxially-grown graphene monolayers on Si side provided measurement of mobility on the order of 29k cm^{2}V^{-1}s^{-1}.[13]

In addition to the exceptional electrical properties, graphene exhibits an extraordinary breaking strength 40 Nm^{-1}, which corresponds to a defect-free layer, and Young's modulus of 1TPa. Also, it can reach elastic stretching records over other materials up to 20%.[14] It has been shown that free-standing graphene can absorb a considerable fraction of white light (2.3%). The absorption process is governed

exclusively by the fundamental fine structure constant ($\alpha \approx 1/137$),[a] and has its origin in the 2D structure and on the lack of energy gap.[15] Remarkable thermal conductivities of up to $(5.3\pm0.48)\times10^3$ Wm^{-1}K^{-1} at room temperature were measured from graphene suspended in a trench built on a Si/SiO$_2$ substrate.[16] These measurements show notably higher transport capabilities as compared to copper and single wall carbon nanotubes (CNT). These properties of graphene are also summarized in Table 1.1. Additionally, great impermeability properties have also been observed under ambient conditions in graphene. This is a consequence of its dense delocalized cloud induced by its π bonding states, which block diffusion through graphene even of hydrogen and helium gases.[17] Graphene is known to be relatively chemically inactive; however, it can be functionalized either by covalent or non-covalent functional groups that diversify its intrinsic electronic properties and which have been widely explored the last few years.[18]

Property	Values	Property	Values
Hybridized form	sp^2	Optical absorption coefficient	~2.3%
Dimensions	2D	Tensile strength	~40 Nm^{-1}
Band gap	Zero	Elastic limit	~20%
Crystal system	Hexagonal	Young's modulus	~1 TPa
Carrier mobility (at T=293 K)	200×10^3 cm^{2}V^{-1}s^{-1}	Maximum current density	> 108 Acm^{-1}
Thermal conductivity	~5300 Wm^{-1}K^{-1}	Mean free path (at T=293 K)	~1000 nm

Table 1.1: Unique physical properties of single layer graphene at room temperature (T=293 K).

---

[a]The fine structure constant $\alpha = e^2/\hbar c \approx$ 1/137 (where $\hbar$ is the reduced Plank's constant and c the speed of light) defines the correlation between relativistic electrons and light, studied in quantum electrodynamics.

1.1.2   Synthesis and Applications

Synthesis

At present, fabrication techniques at industrial scale can be deployed in two main groups; one where exfoliation of graphene[b] plays the main role (top-down synthesis) and another where graphene is grown on a substrate (bottom-up synthesis). Any synthetic method aims at assuring desired properties and morphologies, meeting the specifications from target applications, being scalable to mass production, and ensuring stability and well-controlled fabrication processes. Graphene can be found in powdered form or inner stable colloidal suspensions (i.e., platelets, flakes, etc.) when fabricated by exfoliation in liquid phase. It can also be found as films when fabrication is supported on substrates. In Figure 1.3 are shown the main synthesis techniques of graphene usually employed for mass-scale production. We briefly provide a description on those methods below.
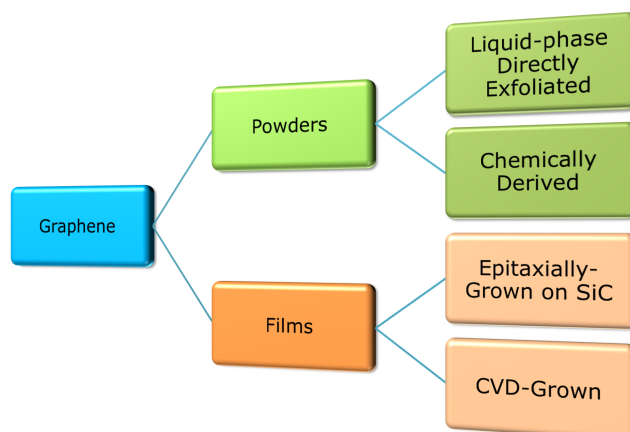
Figure 1.3: Morphologies of graphene according to fabrication method employed. Adapted from ref.[19]

Liquid-phase exfoliation   is an inexpensive fabrication technique. Efficient exfoliation occurs when van der Waals forces between graphene layers in graphite are weakened while keeping uniform sizes of graphene flakes, and is typically achieved using sonication or shear or mechano-chemical ball-milling procedures in water-surfactants or organic solutions.[20–22] This technique is known to produce

---

[b]With exception of "Scotch-tape" exfoliation of graphene from highly oriented pyrolytic graphite (HOPG), other exfoliation methods for large scale production are performed in liquid-phase.

a wide distribution in the layers of flakes with thickness in the range of 10–100 nm. This broad distribution has a negative impact on electronic properties despite fewer impurities and conservation of the conjugated feature in graphene.[23] Microwave radiation and annealing are used as post-exfoliation treatments to remove residual solvent or air bubbles trapped between layers. This enhances the volume of exfoliated graphite layers as well as reducing scrolling effects. The liquid phase offers the advantage of avoiding severe damage in graphene layers caused by removal of solvent residuals upon drying, therefore, any subsequent use of a solution of graphene must necessarily account for the existence of solvents or any other additives.[24]

Chemically derived graphene is a simple and scalable method, in liquid phase as well, to produce reduced graphene oxide (rGO), which is a material with additional functionalities due to the presence of chemical agents but that preserves some of the characteristic properties of pristine graphene. To produce rGO, graphite oxide is first chemically synthesized using, i.e., potassium permanganate and sulfuric and nitric acids deriving in vast population of oxygen groups, as well as water bonded to epoxide, carboxyl, and hydroxyl groups; then it is subjected to an exfoliation process to obtain graphene oxide (GO) sheets, and lastly followed by reduction of those graphene oxide (GO) entities. A drawback of this method is that oxidation processes promote covalent functionalization affecting critically the intrinsic structure of graphene, thus, distinctive carrier mobilities are not present in GO and rGO even when reduction processes have been able to partially restored the conjugate structure characteristic of graphene.[25,26]

Chemical vapor deposition (CVD) is a technique to growth graphene films on substrate of Cu foil (although other transition metals are frequently employed) from hydrogen and methane precursors.[27] Indeed, it has been shown that rectangular graphene films of at least 20×20 in^2 can be produced by the CVD-based process.[28] Typically, such procedures involve support-assisted[c] transfer of CVD-grown graphene to applications-specific substrates. In fact, non-conductive substrates are of great importance for nanoelectronics. This is despite the fact that removal of earlier subjacent Cu foil by chemical etching and subsequent washing induces damage

---

[c]The goal of the support is to prevent breaking the graphene during transfer thus it is the main factor that determines the quality of transferred graphene.

in the graphene layer. Intrinsic properties, including carrier-mobility, of graphene fabricated with CVD are typically much better than those obtained by liquid-phase techniques but still worse than scotch-tape exfoliated graphene.

Epitaxial growth on SiC   of graphene exhibits higher quality and uniformity than that grown by CVD. Indeed, relatively large-scale layers can be produced on SiC which is necessary for electronic applications at wafer scale.[29] This technique is not as low-cost as CVD. Growth is typically achieved in the hexagonal 6H-SiC, a polytype of SiC, on both faces, i.e., Si-terminated (0001) and C-terminated (000$\bar{1}$). Graphene growth in the Si-face is homogeneous and the number of layers are controlled by the heating temperature. The existence of a buffer layer, carbon atoms arranged in non-flat hexagons, is characteristic in the Si-face. On the contrary, the C-face offers different characteristics such as multilayer growth of graphene, however, nucleation spreads over the entire surface and the not-layer-by-layer growth mechanism tends to induce inhomogeneous multilayers.[30] Additionally, rotational staking in the C-face has shown linear band dispersion around the K symmetry point in the Brillouin zone due to weak interlayer interaction, resulting in high electron mobilities.

Applications

A vast variety of applications for graphene has been envisioned. In particular in field effect transistors (FET). It comprises of a source, drain, an active channel that connects the source and drain through which charge carriers are transported, and a gate that controls the conductivity of the channel. Most of the current FETs employ silicon as the preferred material for the channel. In current silicon-based FETs, the performance is increased by dimensional reduction of their components which will be limited by fundamental physics laws, such quantum tunneling effect. In this scenario, graphene is potentially well suited to continue improving FETs performance by virtue of its one atom thickness, its high carrier transport properties and its two-dimensional crystal structure.

In the electronic industry, where Si-based technologies are still leading the market, mass-production techniques still need to overcome inherent limitations of distinctive graphene properties.[31] Large amounts of graphene powders from exfoliation can be manufactured for liquid-based and films applications in energy storage,

with potential for applications as paints, inks, transparent electrodes, conductive supplements in battery electrodes, and as conductive fillers in nanocomposites, if stability and thickness homogeneity can be improved.[24,32] In addition, the high sensitivity to gases and versatility for functionalization makes rGO a good candidate for biosensors[33] and optoelectronics since affordable chemically alterations can be achieved through chemical, thermal, or electrochemical procedures.[34] Construction of field-emission devices is achieved by controlling alignment of rGO fillers in composites to enhance carrier mobilities, as well as thin-film transistors based on rGO inner a matrix of an insulating material that can turn it semiconducting.[26] Although enhancement of electrical conductivity is greatly achieved it is still much less below the mobilities reported by CVD or epitaxial growth techniques.

CVD growth is mostly preferred for fabricated high-quality films of graphene at the wafer level; for instance, Graphene Square company produces graphene films on Cu foil with sizes up to 1×1 m^2, electric resistance in the range of 250–400 Ω/sq, mobilities > 3500 cm^{2}V^{-1}s^{-1}, and transmittance greater than 97%, which are ideal for flexible displays, touch screens, super-capacitors, solar cells, LED lighting, electromagnetic wave barriers, and transistor devices, depending on successful quality after transfer of films to target substrates.[35] Epitaxially-grown graphene can be used for similar applications, and perhaps with greater advantages due to high-mobilities and ability to grow multilayers on the same SiC substrate, but still dependent on the transfer process in applications based on substrates other than SiC. Also, the high-cost production makes this technique less popular than CVD.

1.2 Fabrication Processing Effects

In this thesis we have used graphene obtained by CVD then transferred to SiC substrates. Thus, we are focusing on post-processing effects derived mainly from the transfer process and the CVD method. Transfer processes without any support layer and direct growth of CVD graphene on target substrates are available, but nevertheless, these methods do not reach the levels comparable to transfer process, i.e., low-cost and large-scale production.

A support layer is required to be flexible enough to guarantee good adhesion to both the surface of graphene and the target substrate. Another requirement is its mechanical strength, so graphene films can avoid damage during transfer, and

also that the support should be easily removed after transfer. Currently, polymer-based support layers are typically employed during transfer. Efficient transfer needs a low surface-energy polymer so adhesion forces are weak enough with the graphene surface to facilitate easy removal through dissolution. On the contrary, a target substrate should have higher surface energy to promote good conformation with graphene, consequently minimizing structural deformations on transferred graphene. Indeed, acid etching and oxygen plasma are known to be surface energy enhancers. In addition, polymer and graphene have opposite thermal expansion coefficients that may also induce strain and wrinkles; see Chapters 3 and 4. Some polymers widely used as support layers are Poly(methyl methacrylate)(PMMA), Polydimethylsiloxane (PDMS), Thermal release tape (TRT), and some Natural polymers.

PMMA is one of the first materials reported in CVD processes. It is hard to remove from graphene surface, leaving residues that affect the carrier mobilities of graphene.[36,37] Post-transfer methods to clean graphene from PMMA residues has been employed, namely annealing at high-temperature in H_2/Ar gas environment,[38] laser-assisted removal,[39] or electrolyte cleaning,[40] but unfortunately these all introduce more defects in graphene. PDMS is inexpensive and widely employed in lithography, and it has very large-scale conformal properties with the target substrate. However, poor adhesion between graphene and the target substrate produces broken graphene flakes.[41,42] Among the advantages offered by TRT is its efficient adhesion to a substrate at room temperature; it is easily removed at temperatures greater than 100 °C, and allows the transfer of large areas of graphene onto flexible substrates. However, TRT itself lacks of the increased performance of non-flexible target substrates such as wafers and glass.[28] A hot-pressing method applied after Cu etching achieves transfer onto rigid substrates as well.[43] Additionally, since TRT does not use water during the process, it is suitable for applications where target substrates are sensitive to it. Natural polymers have also been used with interesting achievements, such as purer and higher graphene quality than those obtained with PMMA and PDMS, however the full removal of adsorbed polymer residues is very complicated.

Transfer processes using other non-polymer support layers have also been explored in the attempt to achieve ultra-clean graphene. For example, the use of naphthalene support layers results in ultra-clean graphene upon transfer, and it

is suitable for target substrates that require inorganic solvents and lower temperatures treatments ($\sim 60°$C).[44] However, naphthalene-assisted transfer is not good for rigid substrates since it is not as flexible as polymers. As mentioned earlier, graphene support-free transfer improves the quality of graphene by avoiding polymer and organic residues typically found in supported layer transfer. However, elimination of the Cu substrate makes graphene become vulnerable to cracks due to external forces in the etching solution.

Clearly, specific applications are strongly linked to the adequate selection of underlaying growth and subsequent transfer processes. Effects of growth and processing on graphene quality are still uncertain and further investigations are required before intrinsic properties of graphene can be fully exploited.[19] In this work, as introduced earlier, the utility of NEXAFS to gain insights into graphene fabrication is explored.

1.3 NEXAFS Spectroscopy

Spectroscopy is based on the physical responses through reflection, transmission, or absorption mechanisms between the electromagnetic radiation and matter. The discovery of X-rays in 1895 by Röntgen[45] has boosted developments of several spectroscopic techniques where the decay of the excited state is monitored; some of these are X-ray emission spectroscopy (XES),[46] resonant inelastic X-ray scattering (RIXS),[47] resonant elastic X-ray scattering (REXS),[48] X-ray microscopy,[49] angle-resolved photoemission spectroscopy (ARPES),[50] and X-ray absorption spectroscopy (XAS).[46]

A very important feature of XAS is the presence of absorption edges, the fundamental and element-specific phenomenon exploited in experiments. For instance, in Figure 1.4 the dependency of the absorption cross-section with respect to X-ray energy for the element gold is shown where distinctive discontinuities—so called edges—can be identified (red). By zooming into the L-edge, additional sub-edges can be seen in Figure 1.4. Such discontinuities are the result of excitation of a specific core electron to the continuum. Elastic Rayleigh and inelastic Compton scattering are also shown in Figure 1.4 but with negligible contributions to the X-ray regime because of their low cross-sections.[51]

The labels K, L, M correspond to the principal quantum number n equal to 1, 2, and 3, respectively, where occupancy of quantum states is dictated by the Pauli
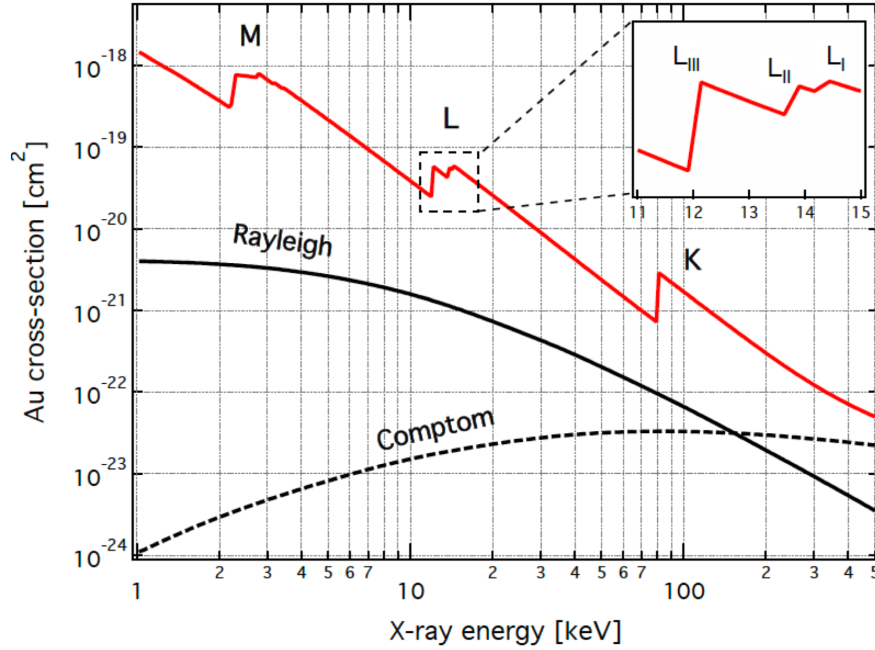
Figure 1.4: Cross-section versus X-ray energy of Au atom. XAS (red) exhibit characteristic features—edges. Rayleigh and Compton scattering are of lower intensity (black). The inset shows details of L-edge absorption. Adapted from ref.[52]

exclusion principle. Figure 1.5 shows absorption edges in ascending energies, for instance the K-edge is associated with a photo-absorption in the $(1s)^2$, similarly L_I, L_{II} and L_{III} edges are associated with photo-absorptions in the levels $(2s)^2$, $(2p_{1/2})^2$ and $(2p_{3/2})^4$, respectively. In the absence of Spin-Orbit interactions, the occurrence and intensity of transitions are dictated by the dipole selection rules, i.e., $\triangle\, l = \pm 1$, $\triangle\, m = 0, \pm 1$;[d] and the dipole transition matrix element $\langle \Psi_f | \hat{H} | \Psi_i \rangle$, where $\hat{H}$ is the interaction Hamiltonian, whereas Ψ_f and Ψ_i correspond to the final and initial states.

At present, XAS has become available in most synchrotron facilities around the world and is widely used in materials research. Indeed, XAS is usually divided in two regimes known as near edge X-ray absorption fine structure (NEXAFS)[e] and extended X-ray absorption fine structure (EXAFS). NEXAFS covers the region (be-

---

[d] l and m are the orbital angular momentum and magnetic momentum quantum numbers, respectively.

[e] X-ray absorption near edge (XANES) and NEXAFS often refer to the same soft (low energy) regime.
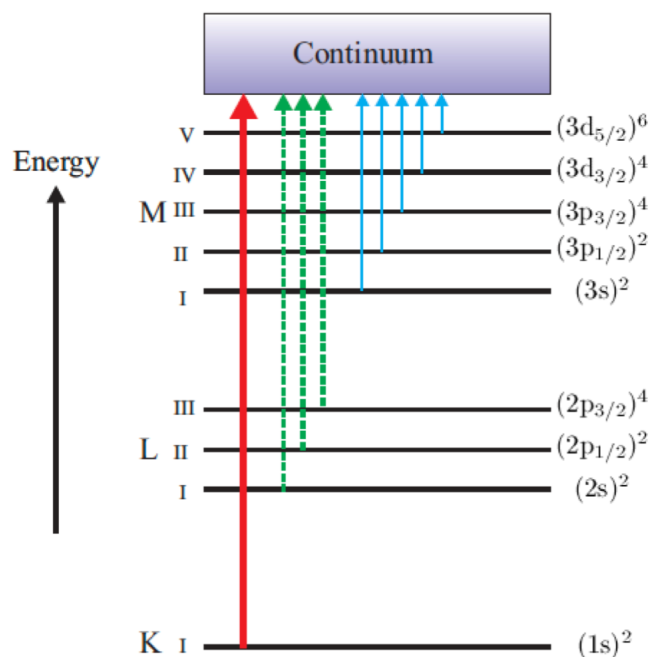
Figure 1.5: Nomenclature utilized to identify absorption edges. The K-edge refers to an electron excitation from $1s$ core state to unoccupied states, and so on. Transitions are governed by the dipole selection rules. Reproduced from ref.[53]

low and above) the absorption edge up to ∼50 eV in the upper limit where the EXAFS spectrum typically begins. NEXAFS features are induced by transitions to unfilled states above the ionization threshold, thus strongly affecting the surrounding environment of the absorbing atom and the electronic structure configuration of the material. In some materials there is a small pre-edge feature, shown in the inset of Figure 1.6, as a result of transitions to bound states (partially filled valence states), which are also heavily affected by the local environment of the absorbing atom.

The X-ray absorption process occurs when an electron from the core of an absorbing atom is excited to higher partially- or fully-unoccupied electronic states by an incident X-ray photon, resulting in highly unstable photoelectron and a core-hole. The excited photoelectron decays nearly intermediately (femtosecond lifetimes) either by emitting fluorescent radiation or by radiation-less Auger emission, as schematically shown in Figure 1.7. Both decay processes are detected experimentally. NEXAFS spectra are angle dependent with the polarization vector of the X-ray beam relative to the orientation of the sample; this particular feature is ad-
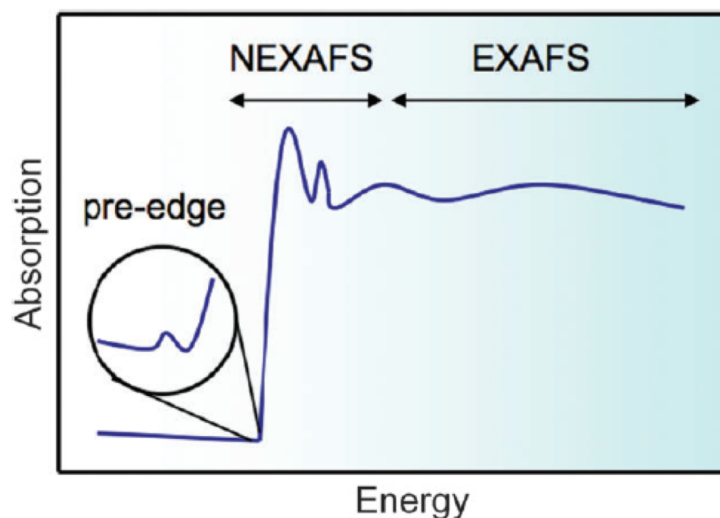
Figure 1.6: Representation of typical divisions on X-ray absorption fine structure spectrum. Reproduced from ref.[54]

vantageous to determine spatial orientation of a molecular orbital typically by tilting the sample. For instance, in the context of carbon materials, such as graphene where electronic states have preferential orientation, an X-ray beam with nearly normal incident angle produces maximum spectrum intensity of the σ^* resonance (σ^* is parallel to the sample plane) while the minimum intensity on π^* resonance (π^* is normal to the sample plane).

1.4 Synchrotron Light Source

Synchrotron light is an electromagnetic radiation emitted when charged electrons traveling at relativistic speeds are forced by magnetic fields to move radially.[53] Early synchrotron facilities dedicated to high energy experiments were built during the 1960s, but synchrotron radiation was used in a parasitic mode. It was not until the mid-seventies that dedicated synchrotron facilities were constructed; currently, there are around 50 dedicated synchrotron facilities around the world.[55] Radiation was produced by bending magnets on the first dedicated synchrotrons which are known as the second generation of light sources. Subsequent development and optimization of magnetic components such as wigglers and undulators situated in straight sections led to the third generation of synchrotron light sources. In many experiments the brightness or the flux per unit source area and per unit solid an-

13
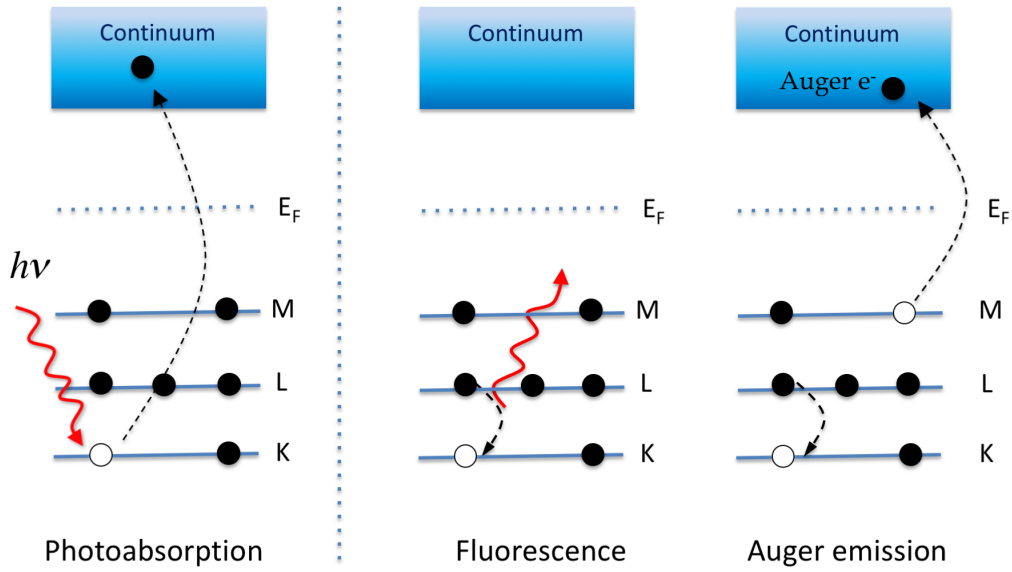
Figure 1.7: Schematic representation of X-ray photo-absorption of core electron to unoccupied states (continuum in solids) and subsequent decay process either by fluorescence or Auger emission; the former emitting radiation and latter emitting electrons. Adapted from ref.[53]

gle[56] is the relevant radiation property since the beam must scan very small areas. In this context, undulators are excellent sources of high-intensity radiation at the present time. Further improvements of light sources are still plausible, and much research is being conducted at this time. It should also be noted that free electron lasers capable of generating extremely short coherent light pulses featuring high intensities and brightness are currently being developed, and will yield a fourth generation of synchrotron radiation sources.[57]

At present, a typical synchrotron light source facility has four main components necessary to operate. In essence, these components are designed to accelerate electrons since their generation until they reach the operational final energies being used in experiments. The first part of the synchrotron is the linear accelerator (LINAC), as seen in Figure 1.8. Here electrons are generated as bunches aided by the radio frequency (RF) cavity, by an electron gun of 100 KeV and further linear acceleration to reach energies around 120 MeV. After being accelerated, electrons are injected to the booster ring, sketched as an inner circle in Figure 1.8. The booster provides further acceleration up to 750 MeV, facilitated by the RF cavities, where the beam gains energy in every cycle. The next step consists of injecting the electron
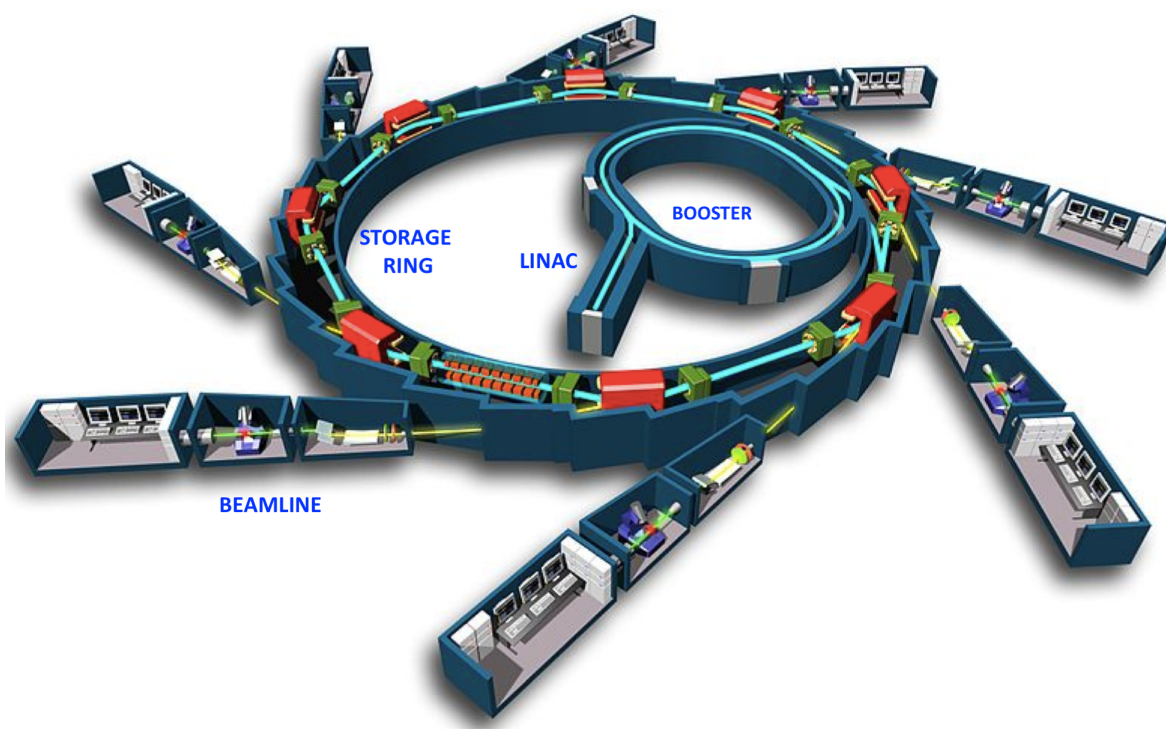
Figure 1.8: Schematic illustration of the principal components of a third generation synchrotron. Adapted from ref.[58]

beam into either the vacuum ultraviolet (VUV) or into the X-ray ring to further increase beam energy to 825 MeV or 2.8 GeV, respectively (outer circle in Figure 1.8). While the electron beam is in the storage ring, it will emit photons as a result of its change in angular momentum while energy loss is compensated with the aid of RF cavities. These emitted photons are known as the synchrotron radiation that needs to be collimated to become monochromatic before being used in the beamline. The last component is the beamline end-station, where the synchrotron radiation is utilized in specific detectors. For instance, the U7A beamline at NSLS Brookhaven in USA, uses a toroidal grating monochromator.

1.5 Computational Approaches to Materials by Design

The advent of sophisticated characterization techniques, combined with powerful computational approaches and data analytics, is paving the way towards the design

of materials in a computer, where properties have been predicted prior to synthesis.[59] This approach is shifting the historic Edisonian approach to materials discovery, to aim for a time and resource-optimized materials by design paradigm. The impacts of this paradigm shift are long-reaching.[60–62] They include close coordination of experiment and theory along with the deployment of data analytics with the purpose of fully gaining knowledge from the combined "experiment." In addition, Materials by Design advocates for data curation and sharing, with which the Laboratory of Matter Dynamics fully endorses. All data in this work is in the process of being curated and shared in the NIST Materials Resource Registry.

1.6 Machine Learning: The DBSCAN Method

As a sub-field of artificial intelligence, machine learning is composed of a set of algorithms capable of learning information from existing data without introducing any previously established physical model. The impact of machine learning in materials science has been rapidly increasing in recent years and remains promising in research and discovery of new materials. Indeed, accurate predictions of material properties like phase diagrams and crystal structures as well as interatomic potentials and energy functionals to boost accuracy of material simulations have been reported.[63–67] Machine learning comprises supervised and unsupervised algorithms, although both methods use a dataset of observations usually named as training data. However, what can be achieved in each method is determined by the kind of training data used.[68]

In supervised learning, the algorithm tries to find a function that best describes the correlation between input and output training datasets, thus, making accurate predictions given a new set of input data. This method is widely employed in materials science. In unsupervised learning, there is no prior output data, and the goal is to find a relationship among input data values. Unsupervised learning is useful for broad analysis such as classification and discovery of hidden patterns and clustering in the input dataset.

Density-Based Spatial Clustering of Applications with Noise (DBSCAN) is an unsupervised data clustering method.[69] The algorithm is used to group data into clusters of different shapes and to separate clusters of high density of observations (closely packed points) from clusters of low density of observations for a given set of points in certain space. A typical flow-chart comprises three steps: first, breaking

up the dataset in n dimensions; second, for each individual point from the dataset, form an n dimensional shape nearby the point, and subsequently count the number of points that are inside the shape; third, iteratively increase the cluster through inspection of each point that contributes to the cluster, and count the number of other surrounding points. DBSCAN does not need to define the number of clusters in advance, it is robust to noise and outliers, it does not require ordering of the points in the dataset, and it is effective uncovering clusters of random shapes.

1.7   Aims of the Thesis

The aim of this thesis is to exploit the high sensitivity of Near Edge X-ray Absorption Fine Structure (NEXAFS) spectroscopy to the bonding architecture surrounding an absorbing atom in the context of current graphene technologies. This measurement capability is explored to analyze the impact of synthesis and transfer approaches through a novel combination of theory, experiment, and data. We examine graphene's characteristic π^* (Chapter 3) and σ^* (Chapter 4) resonances. In addition, NEXAFS sensitivity is further exploited to develop characteristic spectra of a set of defects on graphene through a theoretical approach that is detailed in Chapter 5. In both cases we intend to contribute to the database repository for further applications in the spirit of the Materials Genome Initiative.[61]

Outline

In this document we have given a brief introduction encompassing the definition, electronic structure, and properties of graphene, followed by a short review of common techniques frequently employed to produce graphene, synthesis-processing effects, and target applications (Chapter 1). A description of the X-ray absorption process, synchrotron light sources and the Materials Genome Initiative project are also provided in Chapter 1. The theoretical formalism of Density Functional Theory (DFT) and NEXAFS spectroscopy used in this work, together with details of High Performance Computing (HPC) facilities and experimental details (i.e., fabrication and characterization), as well as a concise description of the features of the Hyperspectral NEXAFS technique are introduced in Chapter 2. In Chapter 3 the results based on the π^* resonance from theory and experiment to assess three data analysis methods of characterization of out-of-plane defects in graphene (i.e., orbital vector

approximation, dichroic ratio, and DBSCAN) are presented. A method to analyze data at the wafer level is also explored. In Chapter 4 we present a technique based on the correlation between σ^* energy position and lattice parameter to determine strains of graphene, preferably on an in-plane distribution. Charge transfer, band structure, and substrate screening effects are also studied in this chapter. Chapter 5 is devoted to study the impact of defects on NEXAFS spectra of graphene from first-principles. All energetic, structural, and electronic characterizations are presented, along with results from angle-resolved NEXAFS spectra and their dependence with distance away from the perturbation induced by defects. The main conclusions and future work are summarized in Chapter 6.

2

Research Background

In this chapter, the components needed to calculate and measure NEXAFS spectra are described in the context of quantum physics. Facilities needed to obtain both experimental and theoretical data are also identified and the physics behind the NEXAFS processes are described. Hyperspectral NEXAFS imaging is also detailed, including the need for data analytic approaches to information extraction from complex data sets.

2.1 Density Functional Theory

2.1.1 The Many-Body Problem

Quantum physics is a theory for determining complex processes occurring in atoms, molecules, or any nanostructure with dimensions ranging from a few Angstroms to hundreds of nanometers. Mathematically, matter can be defined as a group of interacting particles, i.e, electrons and nuclei. To describe the behaviour of any many-electron system one must usually find an approximate solution of the non-relativistic time-independent Schrödinger Equation,[70]

$$\hat{H}\Psi = E\Psi, \tag{2.1}$$

where $\hat{H}$ is the Hamiltonian operator of any system with M nuclei and N electrons given in atomic units[a] by

---

[a] $\hbar = m_e = e = 1/4\varepsilon_0 = 1$

$$\hat{H} = -\frac{1}{2}\sum_i \nabla_i^2 - \frac{1}{2}\sum_\alpha \frac{1}{m_\alpha}\nabla_\alpha^2 + \sum_i \sum_{i>j} \frac{1}{r_{ij}} - \sum_i \sum_\alpha \frac{Z_\alpha}{r_{\alpha i}} + \sum_\alpha \sum_{\beta>\alpha} \frac{Z_\alpha Z_\beta}{R_{\alpha\beta}}, \quad (2.2)$$

or

$$\hat{H} = \hat{T}_e + \hat{T}_n + \hat{V}_{ee} + \hat{V}_{en} + \hat{V}_{nn}, \quad (2.3)$$

where the first, second, third, fourth and fifth terms of the right-hand side of Equations 2.2 and 2.3 correspond to the operators for electronic and nuclear kinetic energy, the electron-electron interaction potential, electron-nuclei potential and nuclear repulsion potential, respectively. In addition, $r_{i/j}$, $r_{\alpha/\beta}$, $Z_{\alpha/\beta}$, and m_α are the electron and nuclear coordinates, the nuclear charge, and the nuclear mass respectively. In solving the equation, the aim is to find the total energy levels ε_i as well as the wave function $\psi_i(\{\vec{r}_j\}, \{R_\alpha\})$ for electrons and nuclei.

2.1.2 The Born-Oppenheimer Approximation

The solution of a many-body Hamiltonian is possible with the use of specific approximations that simplify the Schrödinger Equation. The first simplification is the Born-Oppenheimer approximation (BO),[71] which is based on the fact that electron speed is much higher than nuclear speed, so nuclear motion can be almost static (from the electronic point of view) because the electrons can quickly adjust their state in response to any slower nuclear movement. A direct result of this approximation allows us to neglect the nuclear kinetic operator in the molecular Hamiltonian and split the total molecular wave function Ψ into two terms, one electronic and the other nuclear. The electronic wave function will depend on the electronic coordinates r_i and parametrically on nuclear coordinates r_α while the nuclear wave function will be a function of nuclear coordinates only

$$\Psi = \Psi_e(\vec{r}_i; \vec{r}_\alpha)\Phi_{nucl}(\vec{r}_\alpha), \quad (2.4)$$

In this way, we will separate the equation for the electronic and nuclear particles. Since we are interested in the electronic formulation of the problem, we write the

electronic equation as

$$\hat{H}_e \Psi_e = E_e \Psi_e,\tag{2.5}$$

and the electronic Hamiltonian as

$$\hat{H}_e = \hat{T}_e + \hat{V}_{ee} + \hat{V}_{en},\tag{2.6}$$

where $\hat{V}_{nn}$ is a constant and $\hat{H}$ becomes $\hat{H}_e$ after applying the BO approach.[b] Although we have eliminated at some degree the nuclear degrees of freedom, one still needs to deal with a large number of electrons.

2.1.3 The Hohenberg-Kohn Theorems

In 1964, Hohenberg and Kohn (HK)[72] proved a couple of theorems that are the foundations of DFT, stated as follows:

Theorem 1. *For any system of interacting particles the external potential v_{ext} is (to within a constant) a unique functional of the density $\rho(r)$; since, in turn, v_{ext} fixes $\hat{H}$ we see that the full many particle ground state is a unique functional of $\rho(r)$.*

Essentially, this means that all electronic properties of the system are completely determined by the electronic density $\rho(r)$. As a consequence, the energy E can be expressed as a functional of the electronic density, $E[\rho]$. Therefore, we can use the electron density as the main variable instead of the wave functions that were employed in Hartree-Fock theory.

To explore the implications of this theorem, let us considering as a starting point the electronic Hamiltonian of Equation 2.6 which was obtained after applying the BO approach,

$$\hat{H} = \hat{T}_e + \hat{V}_{en} + \hat{V}_{ee};\tag{2.7}$$

also for practical purposes we rewrite $\hat{V}_{en}$ as

---

[b]From now on we simply call our electronic Hamiltonian as $\hat{H}$ unless we state the contrary.

$$\hat{V}_{en} = \hat{V}_{ext} = \sum_i v_{ext}(r_i), \tag{2.8}$$

where $v_{ext}(r_i) = -\sum_\alpha Z_\alpha / r_{i\alpha}$ is the external potential operator that acts over the i-th electron, as it has an external origin with respect to the electron system.

Hohenberg and Kohn demonstrated that the electron density determines the external potential for a fixed number of electrons, so we assert the electron density contains all the necessary information to describe the system. Then, we can write Equation 2.7 in terms of expectation values which are functionals of the electronic density

$$E[\rho] = T[\rho] + V_{ext}[\rho] + V_{ee}[\rho], \tag{2.9}$$

with

$$V_{ext} = \int \rho(r) v_{ext}(r) dr, \tag{2.10}$$

then we have the expression for the energy functional as

$$E[\rho] = T[\rho] + \int \rho(r) v_{ext}(r) dr + V_{ee}[\rho], \tag{2.11}$$

This energy functional $E[\rho]$ plays a central role in the DFT approach since if it were known we would have solved the Schrödinger equation. Ensuring that a particular density is the ground state density can be determined with the aid of the second HK theorem.

Theorem 2. *A universal energy functional $E[\rho]$ can be defined for any external potential v_{ext}. For any particular v_{ext} the exact ground state energy of the system E_0 is the global minimum of $E[\rho]$, and the density $\rho(r)$ that minimizes the functional is the exact ground state $\rho_0(r)$.*

The practical meaning is that we are able to find the energy using the variational principle

$$E_0 = E[\rho_0] \leqslant \int \rho(r)v(_{ext}r)dr + T[\rho] + V_{ee}[\rho] = E[\rho]. \tag{2.12}$$

In other words, for a given trial electron density $\rho(r)$, which satisfies the necessary boundary conditions such as $\rho(r) \geq 0$ and $\int \rho(r)dr = N$, then $E[\rho]$ represents an upper bound to the true ground state energy E_0. Unfortunately, these theorems do not provide us any useful recipe for estimating E_0 from ρ_0 since we do not know the expression of the functional $E[\rho]$.

2.1.4 The Kohn-Sham Equations

Since the Hohenberg-Kohn theorems restated the intractable many-electron problem in a form that is in principle solvable, the next step is to come up with a practical solution. Kohn and Sham (KS), in 1965,[73] proposed that it is possible to reduce the many-body quantum problem to an exactly equivalent set of one-electron equations, solved self-consistently. They proposed a method that in principle allows us to obtain exact results.

The KS *ansatz* considers a fictitious reference system of N non-interacting electrons (referred by the letter s) that feel the same external potential $v_{ext}(r_i)$ and generates the same density as the interacting system

$$\rho_s = \rho_0. \tag{2.13}$$

By solving the set of equations for the system s it is possible (at least in principle) to obtain the exact density of the interacting system. This reference system has the Hamiltonian

$$\hat{H}_s = \sum_{i=1}^{N} \left[-\frac{1}{2}\nabla_i^2 + v_{ext}^{KS}(r_i) \right] = \sum_{i=1}^{N} h_i^{KS}, \tag{2.14}$$

where h_i^{ks} is the one electron KS Hamiltonian.

Due to the nature of the system s and taking into account the Pauli exclusion principle it is possible to use a ground state wave function for the reference system $\psi_{s,0}$ which can be described by the Slater Determinant[74] of the KS spin-orbitals φ_i^{KS}, where the spatial part $\phi_i^{KS}(r_i)$ of each spin-orbital is an eigenfunction of the

one-electron KS Hamiltonian h_i^{KS}. Thus we have $\varphi_i^{KS} = \phi_i^{KS}(r_i)\sigma_i$ where σ_i is the spin function ($\uparrow$ or $\downarrow$), finally leading us to the eigenvalue equation

$$h_i^{KS}\phi_i^{KS} = \varepsilon_i^{KS}\phi_i^{KS}, \tag{2.15}$$

where ε_i^{ks} is the KS energy.

Considering the reference system s it is possible to define the difference in kinetic energy between the real and fictitious system as

$$\Delta T[\rho] = T[\rho] - T_s[\rho] \tag{2.16}$$

where ΔT is the kinetic energy difference between the real and reference systems with the same electronic density. Similarly, we have the next difference

$$\Delta V_{ee}[\rho] = V_{ee}[\rho] - \frac{1}{2}\int\int\frac{\rho(r_1)\rho(r_2)}{r_{12}}dr_1dr_2, \tag{2.17}$$

where r_{12} is the distance between the positions $r_1(x_1, y_1, z_1)$ and $r_2(x_2, y_2, z_2)$. The term $\frac{1}{2}\int\int\frac{\rho(r_1)\rho(r_2)}{r_{12}}dr_1dr_2$ is the classical expression for the electronic repulsion potential energy assuming they are immersed in a continuous electronic charge distribution ρ.

Replacing Equations 2.16 and 2.17 in Equation 2.11, we have

$$E[\rho] = \int\rho(r)v_{ext}(r)dr + T_s[\rho] + \frac{1}{2}\int\int\frac{\rho(r_1)\rho(r_2)}{r_{12}}dr_1dr_2 + \Delta T[\rho] + \Delta V_{ee}[\rho], \tag{2.18}$$

in this equation the functionals ΔT and ΔV_{ee} are unknown. From now on we define the exchange and correlation functional energy E_{xc} as

$$E_{xc}[\rho] = \Delta T[\rho] + \Delta V_{ee}[\rho]. \tag{2.19}$$

Here E_{xc} contains the kinetic correlation energy, the exchange energy, and the Coulomb correlation energy. Rewriting Equation 2.18 as

$$E[\rho] = \int\rho(r)v_{ext}(r)dr + T_s[\rho] + \frac{1}{2}\int\int\frac{\rho(r_1)\rho(r_2)}{r_{12}}dr_1dr_2 + E_{xc}[\rho], \tag{2.20}$$

we note that except for the fourth term,[c] E_{xc}, in Equation 2.20 the other three terms can be evaluated from the KS electronic density.

In order to solve Equation 2.20 it is necessary to calculate the ground state density. At this point remember we defined $\rho_s(\vec{r})$ as $\rho_0(\vec{r})$. The electronic density of a system of N particles is calculated from the single Slater Determinant of spin-orbitals as

$$\rho = \rho_s = \sum_{i=1}^{N} |\phi_i^{ks}|^2.$$
(2.21)

Now we have to rewrite each term of $E[\rho]$ as an explicit one-particle function of ρ, thus we have

$$\int \rho(r) v_{ext}(r) dr = -\sum_{\alpha} Z_{\alpha} \int \frac{\rho(r_1)}{r_{1\alpha}} dr_1,$$
(2.22)

which is easy to calculate if we know $\rho(r_1)$. The kinetic energy of our reference system can be expressed using the spatial part of the orthonormal KS spin-orbitals as

$$T_s[\rho] = -\frac{1}{2} \sum_{i} \langle \phi_i^{ks}(1) | \nabla^2 | \phi_i^{ks}(1) \rangle,$$
(2.23)

Therefore Equation 2.20 becomes

$$E_0 = -\sum_{\alpha} Z_{\alpha} \int \frac{\rho(r_1)}{r_{1\alpha}} dr_1 - \frac{1}{2} \sum_{i} \langle \phi_i^{ks}(1) | \nabla^2 | \phi_i^{ks}(1) \rangle + \int \int \frac{\rho(r_1)\rho(r_2)}{r_{12}} dr_1 dr_2 + E_{xc}[\rho].$$
(2.24)

It is possible to determine E_0 from the one-particle electronic density as long as we know both the Kohn-Sham orbitals ϕ_i^{KS} and the exchange-correlation energy functional E_{xc}. The KS orbitals ϕ_i^{KS} are the orbitals of the reference system (fictitious system of non-interacting electrons) without any physical meaning. They are a useful tool that allows us to calculate the real electronic density from Equation 2.21.

The Kohn-Sham orbitals are obtained following the second HK theorem, which states that we can find the ground state energy from the variational principle, namely,

---

[c]Although E_{xc} is functional of ρ, the expression to calculate it is unknown.

changing the density to minimize $E[\rho]$ or equivalently varying the orbitals ϕ_i^{KS} to find the density that satisfies the KS equation:[75]

$$h^{KS}\phi_i^{KS}(1) = \varepsilon_i^{KS}\phi^{KS}(1), \qquad (2.25)$$

$$\left[-\frac{1}{2}\nabla^2 + v_s(1)\right]\phi_i^{KS}(1) = \varepsilon_i^{KS}\phi^{KS}(1), \qquad (2.26)$$

$$\left[-\frac{1}{2}\nabla_i^2 - \sum\frac{Z_\alpha}{r_{1\alpha}} + \int\frac{\rho(r_2)}{r_{12}}dr_2 + V_{xc}\right]\phi_i^{KS}(1) = \varepsilon_i^{KS}\phi^{KS}(1). \qquad (2.27)$$

This exchange-correlation potential V_{xc} is the functional derivative of the exchange-correlation energy E_{xc} with respect to the density as is shown below[d]

$$V_{xc}(r) = \frac{\delta E_{xc}[\rho(r)]}{\delta\rho(r)}. \qquad (2.28)$$

This v_{xc} term contains all the remaining contributions of the potential that we do not know exactly.

The Kohn-Sham picture leads to a single electron problem and regroups all the unknown part into the exchange-correlation term. Hence, it is necessary to find realistic E_{xc} functionals to get very accurate predictions of physical properties. Widely used E_{xc} functionals are presented in the next section.

2.1.5 Exchange-Correlations Functionals

To have a formulation that describes the $E_{xc}[\rho]$ functional, three main approximations have been developed. The Local Density Approximation (LDA),[73] the Local Spin Density Approximation (LSDA) and the Generalized Gradient Approximation (GGA).[76]

In the LDA formulation, the exchange-correlation energy per electron at each point $\vec{r}$ in space is assumed to be the exchange-correlation energy per electron in

---

[d]If you are familiar with Hartree-Fock theory, the one electron Kohn-Sham operator $h^{ks}(1)$ is similar to the Fock operator except the exchange operator is replaced by the exchange-correlation potential V_{xc}

a homogeneous electron gas (*Jellium*[77]) which has the same density as the electron gas considered at the same point in space. Its analytic expression is given by

$$E_{xc}^{LDA}[\rho] = \int \rho(r)\varepsilon_{xc}[\rho(r)]dr, \tag{2.29}$$

considering the functional derivative of E_{xc}^{LDA} we have

$$V_{xc}^{LDA} = \frac{\delta E_{xc}^{LDA}}{\delta\rho} = \varepsilon_{xc}[\rho] + \rho\frac{\partial\varepsilon_{xc}[\rho]}{\partial\rho}, \tag{2.30}$$

within this approximation it is possible to split E_{xc} into exchange ε_x and correlation ε_c parts

$$\varepsilon_{xc}[\rho] = \varepsilon_x[\rho] + \varepsilon_c[\rho], \tag{2.31}$$

the $\varepsilon_x(\rho)$ in the uniform electron gas model was given by Dirac, defined as

$$\varepsilon_x[\rho] = -\frac{3}{4}\left(\frac{3}{\pi}\right)^{1/3}[\rho(r)]^{1/3}, \tag{2.32}$$

whereas the correlation part $\varepsilon_c(\rho)$ was computed by Ceperly and Alder[78] using the Quantum Monte Carlo method. Therefore, it is possible to calculate the approximate value of E_{xc} and subsequently $V_{xc}[\rho]$.

In the LSDA formulation, electrons with different spin orientations are described by two different spatial orbitals $\phi_{i\uparrow}^{ks}$ and $\phi_{i\downarrow}^{ks}$. In this way, we separate the total electronic density in a sum of spin-up and down electronic densities

$$\rho(r) = \rho^\uparrow(r) + \rho^\downarrow(r). \tag{2.33}$$

as a consequence, E_{xc} becomes a functional of both densities (or of the total density and the magnetic moment $\rho_m(r) = \rho^\uparrow(r) - \rho^\downarrow(r)$)

$$E_{xc}^{LSDA}[\rho^\uparrow, \rho^\downarrow] = \int \rho(r)\varepsilon_{xc}[\rho^\uparrow(r), \rho^\downarrow(r)]dr, \tag{2.34}$$

the procedure to obtain the LSDA is analogous to the LDA procedure. In fact, LDA is a special case of LSD for spin-compensated cases. The way we calculate the E_{xc} energy in LDA/LSDA means we assume that the exchange-correlation potentials depend only on the local values of density. But density in physical systems—atoms and molecules—often varies drastically with r. Hence the next step is to supply information about how density changes with r.

In the GGA approximation, we try to improve the LDA/LSDA approximation by introducing a dependence on the gradient of the electronic density to take into account the possible inhomogeneity of the electron gas. Thus the E_{xc} is given by

$$E_{xc}^{GGA}[\rho^{\uparrow}, \rho^{\downarrow}] = \int f[\rho^{\uparrow}(r), \rho^{\downarrow}(r), \nabla\rho^{\uparrow}(r), \nabla\rho^{\downarrow}(r)]dr. \qquad (2.35)$$

where f is a functional of spin density and its gradient. Again, it is possible to split E_{xc}^{GGA} in exchange and correlation parts: $E_{xc}^{GGA} = E_{x}^{GGA} + E_{c}^{GGA}$ and follow a procedure analogous to LDA.

As a final note, we have noticed during the derivation of the Kohn-Sham picture that KS orbitals as well as eigenvalues are not the real quasi-particle spectrum. This means that calculating any single-particle property, i.e., band structure, DOS and so on, is in principle not allowed. Nevertheless, It has been noted that KS eigenvalues do resemble to the quasi-particle eigenstates thus it has become a common practice to use them as such in electronic structure calculation.

2.1.6 The Pseudopotential Approximation

Materials are determined by chemical bonds between atomic species through their electronic states where only outer most states (valence electronic states) participate in bonding formation. While, inner most states (core electronic states) have less or null participation in the bonding formation.

Computational cost of DFT calculations are reduce by taking advantage of our previous argument. This is the so-called pseudopotential (PP) approximation.[79] In principle, core electrons remain unmodified during the bond formation so an effective potential that only accounts for the shielded core effect (which affects the valence electrons) is constructed. Figure 2.1 shows the PP and pseudo wave functions compared against all electron functions. Further details of the PP approach

can be found in Phillips and Kleinman's work.[80]
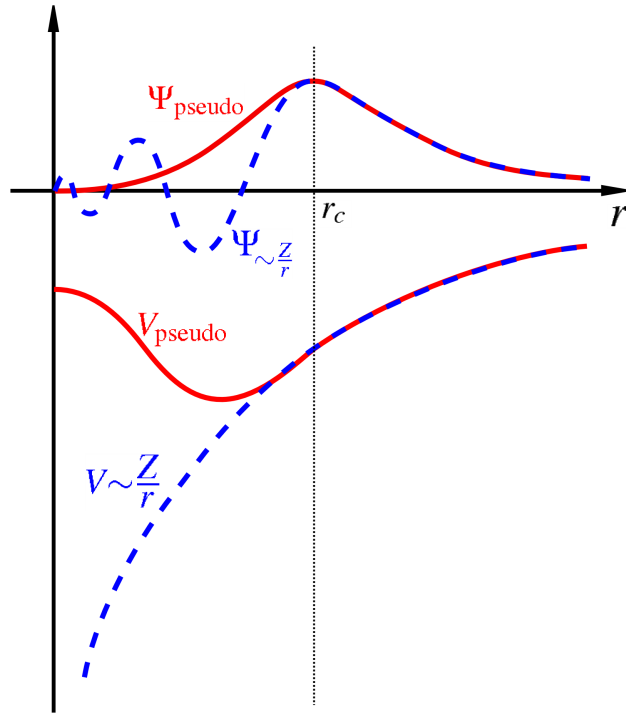
Figure 2.1: Both real wave function and Coulomb potential of nucleus (in blue) match the corresponding pseudo wave function and pseudopotential (in red) above a certain cutoff radius r_c.

2.2 *Ab initio* Simulation of NEXAFS Spectroscopy

In the semi-classical radiation theory framework to describe emission/absorption events of individual electromagnetic wave by a charged particle, the electromagnetic field is treated classically, particles and Coulomb interactions between them are treated quantically, and the time-dependent perturbation theory is applied to the Hamiltonian associated with the interaction between a particle and electromagnetic field.[81,82]

2.2.1 Fermi's Golden Rule

Let us derive the corresponding time-dependent Schrödinger equation of a charged particle in the presence of an electromagnetic field, i.e., express the Hamiltonian as a function of the scalar and vector potentials of the field. Assuming that there is no electromagnetic field that interact with the particle, then the Hamiltonian is

$$\hat{H}_0 = \frac{\hat{P}^2}{2m} + U(\mathbf{r}, t) \tag{2.36}$$

where $U(\mathbf{r}, t)$ accounts for non-electromagnetic forces and $\hat{P} \equiv -i\hbar\nabla$ is the momentum operator. In the presence of an electromagnetic field the Hamiltonian is obtained by a direct substitution of (according to the minimal coupling principle)

$$\hat{H}_0 \longrightarrow \hat{H} - q\Phi(\mathbf{r}, t)$$
$$\hat{P} \longrightarrow \hat{P} - q\mathbf{A}(\mathbf{r}, t) \tag{2.37}$$

where $\Phi(\mathbf{r}, t)$ is the scalar potential, $\mathbf{A}(\mathbf{r}, t)$ is the the vector potential and q is the particle charge.[e] Replacing Equation 2.37 in Equation 2.36 gives

$$\hat{H} - q\Phi(\mathbf{r}, t) = \frac{1}{2m}(\hat{P} - q\mathbf{A})^2 + U(\mathbf{r}, t) \tag{2.38}$$

If non-electromagnetic forces are not present, i.e., $U(\mathbf{r}, t) = 0$, then the time-dependent

---

[e] Scalar and vector potentials define the magnetic and electric field as $\mathbf{B} = \nabla \times \mathbf{A}$ and $\mathbf{E} = -\nabla\Phi - \frac{\partial \mathbf{A}}{\partial t}$, respectively.

Schrödinger equation is

$$i\hbar\frac{\partial\Psi}{\partial t} = \left[\frac{1}{2m}(\hat{P} - q\mathbf{A})^2 + q\Phi(\mathbf{r},t)\right]\Psi \tag{2.39}$$

The Schrödinger Equation 2.39 is a function of the gauge dependent potentials $\Phi(\mathbf{r},t)$ and $\mathbf{A}(\mathbf{r},t)$ which define the unique $\mathbf{E}$ and $\mathbf{B}$ fields in a non-exclusively fashion.[†] Taking the so-called Coulomb gauge that makes $\nabla \cdot \mathbf{A}(\mathbf{r},t) = 0$ leads to a wavefunction multiplied by a phase-factor, i.e., $e^{iq\chi(\mathbf{r},t)/\hbar}$, as a result, expectation values become gauge independent. Thus, we can safely apply the gauge transformation

$$\Psi'(\mathbf{r},t) = \Psi(\mathbf{r},t)\exp\left[iq\chi(\mathbf{r},t)/\hbar\right]$$
$$\mathbf{A}(\mathbf{r},t) \longrightarrow \mathbf{A}'(\mathbf{r},t) = \mathbf{A}(\mathbf{r},t) + \nabla\chi(\mathbf{r},t) \tag{2.40}$$
$$\Phi(\mathbf{r},t) \longrightarrow \Phi'(\mathbf{r},t) = \Phi(\mathbf{r},t) - \frac{\partial\chi(\mathbf{r},t)}{\partial t}$$

By applying the Coulomb gauge, it is possible to neglect the scalar potential for distance very far from the radiation source, giving the electric field as a function of the vector potential which can be written as a set of harmonic plane waves as follow

$$\mathbf{E} = -\frac{\partial\mathbf{A}}{\partial t}$$
$$\mathbf{A}(\mathbf{r},t) \propto \boldsymbol{\varepsilon}e^{i(\mathbf{k}\cdot\mathbf{r}-\omega t)} \tag{2.41}$$

where $\boldsymbol{\varepsilon}$ is the polarization vector, $\boldsymbol{k}$ is the wave vector and ω the angular frequency. Considering a single harmonic plane wave as

$$\mathbf{A}(\mathbf{r},t) = 2A_0\mathbf{u}_k\cos\left(\mathbf{k}\cdot\mathbf{r} - \omega t\right) = A_0(\mathbf{u}_k e^{i(\mathbf{k}\cdot\mathbf{r}-\omega t)} + \mathbf{u}_k e^{-i(\mathbf{k}\cdot\mathbf{r}-\omega t)}) \tag{2.42}$$

Then the electric field can be expressed as

$$\mathbf{E} = -2\omega A_0\boldsymbol{\varepsilon}\sin(\mathbf{k}\cdot\mathbf{r} - \omega t) \tag{2.43}$$

[†]Potentials are a function of an arbitrary function $\chi(\mathbf{r},t)$ as, $\mathbf{A}(\mathbf{r},t) \longrightarrow \mathbf{A'}(\mathbf{r},t) = \mathbf{A}(\mathbf{r},t) + \nabla\chi(\mathbf{r},t)$ and $\Phi(\mathbf{r},t) \longrightarrow \Phi'(\mathbf{r},t) = \Phi(\mathbf{r},t) - \partial\chi(\mathbf{r},t)/\partial t$

In the Coulomb gauge, the Hamiltonian from Equation 2.39 is

$$\hat{H} = \frac{1}{2m}(\hat{P} - q\mathbf{A})^2 = \hat{H}_0 + \hat{H}' \tag{2.44}$$

where $\hat{H}_0 = \hat{P}^2/2m$, then $\hat{H}'$ is

$$\hat{H}' = \hat{H} - \hat{H}_0 = \frac{1}{2m}\left[(\hat{P} - q\mathbf{A})^2 - \hat{P}^2\right] = -\frac{q}{2m}(\hat{P} \cdot \mathbf{A} + \mathbf{A} \cdot \hat{P}) + \frac{q^2\mathbf{A}^2}{2m} \tag{2.45}$$

Since vector potential $\mathbf{A}$ and momentum operator $\hat{P}$ commute each other, we have

$$\hat{H}' = -\frac{q}{m}\mathbf{A} \cdot \hat{P} + \frac{q^2\mathbf{A}^2}{2m} \tag{2.46}$$

$\hat{H}'$ will be treated as a perturbation. In the first-order approximation of the transition probability the term $\mathbf{A}^2$ is set to zero, then $\hat{H}'$ is[9]

$$\hat{H}' = -\frac{q}{m}\mathbf{A} \cdot \hat{P} \tag{2.47}$$
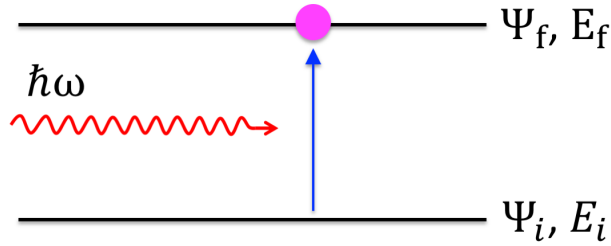
Figure 2.2: Schematic illustration of absorption process of an electron from an initial state Ψ_i, at energy E_i, to a final state Ψ_f at energy E_f.

Considering that resonance condition is satisfied $\omega_{fi} = (E_f - E_i)/\hbar > 0$, which represent the absorption process that promote an electron from an initial to a final

---

[9]From $\nabla \cdot \mathbf{A} = 0$ and Equation 2.42, it is shown that ε and k are orthogonal, thus **E**, k and **B** form a set of orthogonal vectors to each other.

state,[h] as depicted in Figure 2.2. Also, let us assume a single harmonic plane wave perturbation on the electron, then $\hat{H}'$ become

$$\hat{H}' = -\frac{q}{m}\mathbf{A} \cdot \hat{P} = \frac{e}{m}A_0(\omega)\hat{P} \cdot (\boldsymbol{\varepsilon}e^{i(\mathbf{k}\cdot\mathbf{r}-\omega t)} + \boldsymbol{\varepsilon}e^{-i(\mathbf{k}\cdot\mathbf{r}-\omega t)})$$
$$\equiv \hat{\nu}(\mathbf{r},\omega)e^{-i\omega t} + \hat{\nu}^{\dagger}(\mathbf{r},\omega)e^{+i\omega t} \tag{2.48}$$

where

$$\hat{\nu}(\mathbf{r},\omega) = \frac{e}{m}A_0(\omega)\boldsymbol{\varepsilon} \cdot \hat{P}e^{i\mathbf{k}\cdot\mathbf{r}} \tag{2.49}$$

Then the transition rate from an initial state Ψ_i to a final state Ψ_f is given by

$$W_{fi} \equiv \frac{\partial}{\partial t}P_{fi} = \frac{2\pi}{\hbar}|\nu_{fi}|^2\delta(E_f - E_i - \hbar\omega) \tag{2.50}$$

where

$$\nu_{fi} \equiv \langle\Psi_f \mid \hat{\nu}(\mathbf{r},\omega) \mid \Psi_i\rangle \approx \langle\Psi_f \mid \hat{P}e^{i\mathbf{k}\cdot\mathbf{r}} \mid \Psi_i\rangle \tag{2.51}$$

2.2.2 Dipole Approximation

The exponential dependence of the transition matrix element can be expanded as powers series:[i]

$$e^{i\mathbf{k}\cdot\mathbf{r}} = 1 + i\mathbf{k}\cdot\mathbf{r} - \frac{1}{2}(\mathbf{k}\cdot\mathbf{r})^2 + \cdots \tag{2.52}$$

Since the only transition that contributes significantly is the dipole transition ($\mathbf{k}\cdot\mathbf{r} \sim 2\pi r/\lambda \ll 1$), then we can conveniently approximate the exponential to the first term of the expansion ($e^{i\mathbf{k}\cdot\mathbf{r}} \approx 1$) giving the so-called electric-dipole approximation. Thus, considering $\hat{P} = \frac{im}{\hbar}[\hat{H}_0, \mathbf{r}]$ and the dipole approach, the transition matrix element of Equation 2.51 become

---

[h]It should be mentioned that absorption and stimulated emission due to a single harmonic plane wave perturbation are equally likely. Here we focus only in absorption process.

[i]Approximation to the first term of the power series gives dipole transitions, the second ($\mathbf{k} \cdot \mathbf{r}$) gives the quadrupole, and so on.

$$\langle \Psi_f \mid \hat{P} e^{i\mathbf{k}\cdot\mathbf{r}} \mid \Psi_i \rangle \approx \langle \Psi_f \mid \hat{P} \mid \Psi_i \rangle = \frac{im}{\hbar} \langle \Psi_f \mid \hat{H}_0 \mathbf{r} - \mathbf{r}\hat{H}_0 \mid \Psi_i \rangle$$

$$= \frac{im}{\hbar} \langle \Psi_f \mid E_f \mathbf{r} - \mathbf{r} E_i \mid \Psi_i \rangle \qquad (2.53)$$

$$= im \frac{(E_f - E_i)}{\hbar} \langle \Psi_f \mid \mathbf{r} \mid \Psi_i \rangle$$

where the transition matrix element $\langle \Psi_f \mid \mathbf{r} \mid \Psi_i \rangle$, a function of the position operator $\mathbf{r}$, is often known as the dipole moment. Rewriting Equation 2.50 we have

$$W_{fi} = \frac{\pi e^2 A_0^2}{2\hbar c^2} \omega^2 |\boldsymbol{\varepsilon} \cdot \langle \Psi_f \mid \mathbf{r} \mid \Psi_i \rangle|^2 \delta(E_f - E_i - \hbar\omega) \qquad (2.54)$$

We can define the absorption cross section σ_{abs} as the transition rate W_{fi} per unit of incoming electromagnetic flux $F_E = A_0^2 \omega / 8\pi\hbar c$; and the oscillator strength f_{fi} from an integration over the angular spatial $\int d\omega \sigma_{abs}(\omega)$ as follow

$$\sigma_{abs} = \frac{W_{fi}}{F_E} = 4\pi^2 \alpha \hbar\omega |\boldsymbol{\varepsilon} \cdot \langle \Psi_f \mid \mathbf{r} \mid \Psi_i \rangle|^2 \delta(E_f - E_i - \hbar\omega) \qquad (2.55)$$

$$\int d\omega \sigma_{abs}(\omega) = 4\pi^2 \alpha \omega_{fi} |\boldsymbol{\varepsilon} \cdot \langle \Psi_f \mid \mathbf{r} \mid \Psi_i \rangle|^2 = \frac{2\pi^2 e^2}{mc} f_{fi} \qquad (2.56)$$

where α is the fine structure constant and f_{fi} is[j]

$$f_{fi} \equiv \frac{2m}{\hbar} \omega_{fi} |\boldsymbol{\varepsilon} \cdot \langle \Psi_f \mid \mathbf{r} \mid \Psi_i \rangle|^2 \qquad (2.57)$$

This many-particle matrix element can be reduced to a single-particle form as long as the transition process is "sudden" with respect to the relaxation time of the other non-excited electrons, i.e., $\langle \Psi_f \mid \mathbf{r} \mid \Psi_i \rangle \approx S \langle \psi_f \mid \mathbf{r_1} \mid \psi_i \rangle$. Indeed, single approach is accurate and approximately constant for all transitions up to a factos S.[83] Therefore, we can rewrite f_{fi} as

---

[j]Sum of all final states equalize the number of electrons: $\sum_f f_{fi} = N$. Also, known as the Thomas-Reiche-Kuhn sum rule.

$$f_{fi} \equiv \frac{2m}{\hbar}\omega_{fi}|\boldsymbol{\varepsilon} \cdot \langle \psi_f \mid \boldsymbol{r_1} \mid \psi_i \rangle|^2 \tag{2.58}$$

where $|\psi_{f,i}\rangle$ denotes the the single-electron states involved in the transition. Also note that ω_{fi} corresponds to the electronic energy states difference $\omega_{fi} = (e_f - e_i)/\hbar$.

2.2.3 Polarization

The oscillator strength depends on the orientation of the material under study with respect to the polarization vector ε. For systems with fully spatial anisotropy the simplest expression of the averaged f_{fi} can be estimated by averaging over the x, y and z directions, as expressed below

$$f_{fi} \equiv \frac{1}{3}\frac{2m\omega_{fi}}{\hbar}(|\langle \psi_f \mid \mathbf{x} \mid \psi_i \rangle|^2 + |\langle \psi_f \mid \mathbf{y} \mid \psi_i \rangle|^2 + |\langle \psi_f \mid \mathbf{z} \mid \psi_i \rangle|^2) \tag{2.59}$$

The f_{fi} in systems that exhibit some degree of symmetry, in particular, for two-dimensional crystals at an arbitrary angle θ as shown in Figure 2.3, can be estimated by[84]

$$f_{fi} \equiv \frac{2m\omega_{fi}}{\hbar}(|\langle \psi_f \mid \mathbf{x} \mid \psi_i \rangle|^2 + |\langle \psi_f \mid \mathbf{y} \mid \psi_i \rangle|^2)\sin^2\theta + \frac{2m\omega_{fi}}{\hbar}(|\langle \psi_f \mid \mathbf{z} \mid \psi_i \rangle|^2)\cos^2\theta \tag{2.60}$$

For instance, in graphene the oscillator strength of fully excitation $1s \rightarrow \pi^*$ and $1s \rightarrow \sigma^*$ can be computed at $\theta = 0$ and $\theta = 90$ degrees respectively, by the following equations.

$$\begin{aligned}f_{fi}(1s \rightarrow \sigma^*) &\equiv \frac{m\omega_{fi}}{\hbar}(|\langle \psi_f \mid \mathbf{x} \mid \psi_i \rangle|^2 + |\langle \psi_f \mid \mathbf{y} \mid \psi_i \rangle|^2) \\ f_{fi}(1s \rightarrow \pi^*) &\equiv \frac{2m\omega_{fi}}{\hbar}(|\langle \psi_f \mid \mathbf{z} \mid \psi_i \rangle|^2)\end{aligned} \tag{2.61}$$
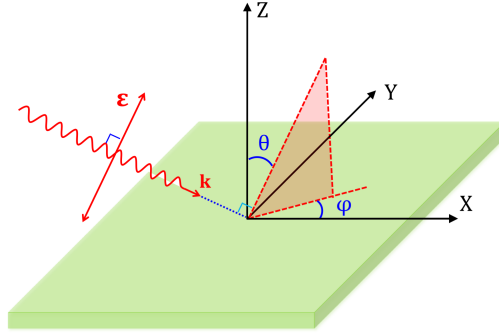
Figure 2.3: Schematic representation of angle dependence of incoming radiation and a 2D system in Cartesian coordinates. ε is the polarization vector.

2.2.4 Orbital Vector Approach: The α parameter

In order to derive a practical formula to study the angular dependence of π^* orbital variations when rippling/corrugations distortions are present. It is useful to represent the π^* orbital as a vector with certain polar angle (α). In fact, this α angle is shown to be an important parameter to describe such surface deformations, as shown in Chapter 3. This spatial approximation of π^* as a vector is based on the fact that dipole transition from $1s$ to p component of the π^* is highly directional.[85]

A consequence of the angular dependence of the π^* resonance approach is that only peak height changes are considered. Such changes in intensity are proportional to changes in the oscillator strength f_{fi}, given by

$$I \propto |\langle \psi_f \mid \boldsymbol{e} \cdot \boldsymbol{p} \mid \psi_i \rangle|^2 \propto \frac{1}{\boldsymbol{E}^2} |\langle \psi_f \mid \boldsymbol{E} \cdot \boldsymbol{p} \mid \psi_i \rangle|^2 \qquad (2.62)$$

where $\boldsymbol{E}$ is the electric field vector, $\boldsymbol{p}$ is the momentum operator and $\boldsymbol{e}$ is the unit vector in the direction of $\boldsymbol{E}$. If the coordinate system is oriented such that incident beam propagates in the Z-axis and unit vectors $\boldsymbol{e}^{\parallel}$ and $\boldsymbol{e}^{\perp}$ are in the direction of X and Y axis respectively, then

$$\boldsymbol{E} = \boldsymbol{E}^{\parallel} \cos(kz - \omega t) + \boldsymbol{E}^{\perp} \sin(kz - \omega t) \qquad (2.63)$$

where k is the momentum of the incident beam and ω is the frequency of the electromagnetic wave. Since matrix elements are under the dipole approximation, an

integration in time over one wave period give the matrix element in the form

$$I \propto \frac{\int_0^{2\pi} |\langle \psi_f \mid \boldsymbol{E}^{\parallel} \cdot \boldsymbol{p} \cos(\omega t) - \boldsymbol{E}^{\perp} \cdot \boldsymbol{p} \sin(\omega t) \mid \psi_i \rangle|^2 d(\omega t)}{\int_0^{2\pi} |\boldsymbol{E}^{\parallel} \cos(\omega t) - \boldsymbol{E}^{\perp} \sin(\omega t)|^2 d(\omega t)} \tag{2.64}$$

Then considering the polarization factor P as

$$P = \frac{|\boldsymbol{E}^{\parallel}|^2}{|\boldsymbol{E}^{\parallel}|^2 + |\boldsymbol{E}^{\perp}|^2} \tag{2.65}$$

The total resonance intensity can be expressed as

$$I \propto P|\langle \psi_f \mid \boldsymbol{e}^{\parallel} \cdot \boldsymbol{p} \mid \psi_i \rangle|^2 + (1 - P)|\langle \psi_f \mid \boldsymbol{e}^{\perp} \cdot \boldsymbol{p} \mid \psi_i \rangle|^2 \tag{2.66}$$

for a $1s$ initial state and a vector final state orbital the matrix element points in the direction of the final state orbital, then Equation 2.62 is reduced to

$$|\boldsymbol{e} \cdot \langle \psi_f \mid \boldsymbol{p} \mid \psi_i \rangle|_v^2 \propto I_v = \cos^2 \delta \tag{2.67}$$

where the index v represent the π^* vector final state and δ is the angle between $\boldsymbol{E}$ and the π^* vector final state.

Intensities related with the angle-dependent matrix elements (from Equation 2.67) for the $\boldsymbol{E}^{\parallel}$ component is given by $I_v^{\parallel}$. Analogously, the angle-dependent intensities for the $\boldsymbol{E}^{\perp}$ component is given by $I_v^{\perp}$. Considering those definitions Equation 2.66 becomes

$$I_v = A[PI_v^{\parallel} + (1 - P)I_v^{\perp}] \tag{2.68}$$

where $I_v^{\parallel}$ and $I_v^{\perp}$ are

$$I_v^{\parallel} = \cos^2 \theta \cos^2 \alpha + \sin^2 \theta \sin^2 \alpha \cos^2 \varphi + 2 \sin \alpha \cos \alpha \sin \theta \cos \theta \cos \varphi \tag{2.69}$$

$$I_v^{\perp} = \sin^2 \alpha \sin^2 \varphi \tag{2.70}$$

37

By neglecting terms associated with the azimuth angle due to symmetry reasons, i.e., $\varphi = 0$, and assuming a perfect linearly polarized beam, i.e., $P = 1$, we have

$$I(\theta) = A(\cos^2\theta\cos^2\alpha + \sin^2\theta\sin^2\alpha + 2\sin\alpha\cos\alpha\sin\theta\cos\theta) + c \qquad (2.71)$$

A particular application on a single sheet of graphene will result in a specific average single orientation of π^* vector final state with respect to the substrate upon transfer. These local perturbations from rippling will be modeled through α. Additionally, to account for π^* intensity variations in highly delocalized systems the parameter c was also included.

2.2.5 The Shirley Code

The XCH approach

Shirley is a non-distributed scientific software used to simulate the NEXAFS spectra. It is built on the excited electron and core-hole (XCH)[86] approach that efficiently describe the photoabsorption of an electron on the absorbing atom. XCH was first applied to study the local structure of liquid water and ice at the near K-edge of O which resulted in good qualitative agreement with X-ray absorption experiments available at that time.

In the XCH method, the initial state ($1s$) of the core-hole matrix element ($\langle\psi_f \mid \boldsymbol{r_1} \mid \psi_i\rangle$) is usually the ground state and is available from electronic structure calculations, whereas the final state is not directly available because the use of pseudopotentials to represent the core states. This problem is circumvented by applying a reconstruction of the core states in the pseudopotential of the target absorbing atom, i.e., an exclusive *all electron* description for that particular absorption atom in the framework of the projector augmented wave (PAW) method. Then, the final state is obtained by explicitly removing an electron from the $1s$ core state, and placing an electron at the lowest unoccupied state. Therefore, core-hole interaction is completely taken into account by self-consistent iterations of the Kohn-Sham equations for the final state (excited state).[87,88]

An essential feature is that Shirley code was implemented using the recursive method. This method permits to only calculate the occupied states as a consequence of express the cross section as function of a continued fraction.[89] Indeed,

pioneering implementation of the recursive method to calculate the dielectric function including accurate description of the core-hole interaction within the Bethe-Salpeter formalism has been reported by Benedict and Shirley.[90] The use of the recursive method represent a significant advantage that simplifies the treatment of large supercells. This software is also greatly benefited with the technique that use Bloch functions at only few points in the Brillouin zone to construct an optimal basis set for the electron states throughout the zone, therefore, reducing the computational cost that means to converge numerically the Brillouin zone integral.[91]

The Shirley flowchart

Figure 2.4 summarize the typical steps involved in NEXAFS calculation. The input to feed the code is a fully relaxed structure, where calculations of the input structure at ground state (GS) and excited state (under the XCH approach) are performed. In both scenarios, ground and excited, calculations of individual atoms are also performed to serve as a reference for posterior energy alignment. Those GS and XCH calculations will provide a non-aligned NEXAFS spectra. Finally, the alignment named chemical shift Δ referenced to the Fermi level E_F are performed to give the NEXAFS spectra ready for analysis as shown in Figure 2.4, where E_{sys}^{XCH} and E_{ref}^{XCH} are the total energies of the system supercell with an absorbing atom and the total energy of an isolated absorbing atom, respectively. Similar description is applied for E_{sys}^{GS} and E_{ref}^{GS} at ground state.

2.2.6 High Performance Computing Facilities

Two High Performance Computing (HPC) Facilities have been used to complete the work described here, based in Wales (UK) and Berkeley (CA).

2.2.6.1 High Performance Computing Wales

HPC Wales hubs usually accessed to compute data for this thesis are based on Cardiff and Swansea's University campuses. What follow are technical features gathered from its official website.[93]
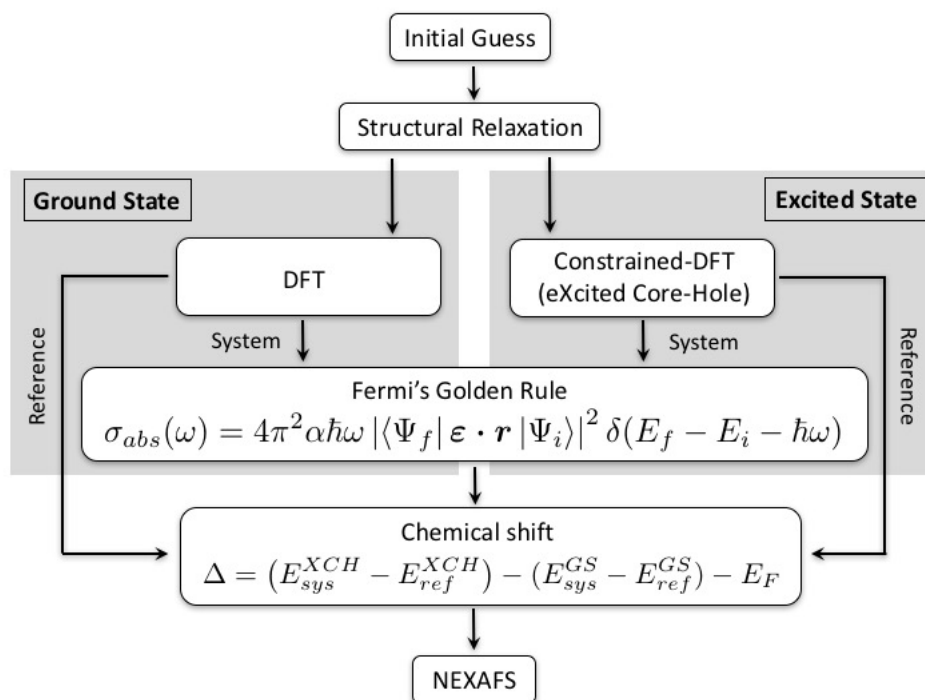
Figure 2.4: Flaw-chart of first-principles computation of NEXAFS as implemented in Shirley code. Reproduced from ref.[92]

The Cardiff Clusters

Cardiff HTC

- 162 x BX922 dual-processor nodes, each having two, six-core Intel Westmere Xeon X5650 2.67 GHz CPUs and 36GB of memory, providing a total of 1994 Intel Xeon cores (with 3 GB of memory/core).

- 4 RX600 X7550 dual processor Intel Nehalem nodes, 2.00 GHz, each with 128 GB RAM.

- 1 RX900 X7550 node with 8 Nehalem processors, 2.00 GHz and 512 GB RAM.

- Total memory capacity for the system of 6.85 TBytes.

- 100 TBytes of permanent storage.

Cardiff CPC

- 384 x CX250 dual processor nodes, each having two eight-core Intel Sandy Bridge Xeon E5-2670 2.6GHz CPUs and 64GB of memory, providing 6144 Intel Xeon cores (with 4GB of memory / core).

- Total memory capacity of 24.5 TBytes.

Cardiff GPU

- 16 x CX270 dual-processor nodes, each having two eight-core Intel Sandy Bridge Xeon E5-2670 2.6GHz CPUs and 64GB of memory providing 256 cores (with 4GB.

The Swansea Clusters

Swansea CPB

- 16 x CX250 dual-processor nodes, each having two eight-core Intel Sandy Bridge Xeon E5-2690 2.9GHz CPUs and 128GB memory providing 256 cores (with 8GB memory / core).

- 240 x CX250 dual-processor nodes, each having two eight-core Intel Sandy Bridge Xeon E5-2690 2.9 GHz CPUs and 64GB memory providing 3840 cores (with 4GB memory / core).

- Total memory capacity of 17 TBytes.

Swansea CPC

- 128 x CX250 dual-processor nodes, each having two eight-core Intel Sandy Bridge Xeon E5-2670 2.6 GHz CPUs and 64GB memory providing 2048 cores (with 4GB memory / core).

- Total memory capacity of 8 TBytes.

Swansea GPU

- 16 x CX270 dual-processor nodes, each having two eight-core Intel Sandy Bridge Xeon E5-2670 2.6GHz CPUs and 64GB of memory providing 256 cores (with 4GB memory / core). Each node also has an Nvidia Tesla M2090 GP-GPU module with 512 CUDA cores and 6GB internal memory.

- Total memory capacity of 1 TByte.

2.2.6.2 Molecular Foundry

Vulcan[94] and Etna[95] clusters are part of the Lawrence Berkeley National Laboratory Supercluster facilities under the same Supercluster infrastructure. Clusters use the scheduler Simple Linux Utility for Resource Management (SLURM) to manage jobs. Here we listed main hardware configuration of those two clusters. Further general information and details of other clusters from the facility can be found in the High Performance Computing at Berkeley Lab portal.[96,97]

Vulcan

It has built in a mixture of CPUs with different architectures and memory features. Majority of nodes intercommunication used multiple high performance QLogic 40 Gbps QDR Infiniband switches, as detailed Figure 2.5.

Partition	Nodes	Node List	CPU	Cores	Memory	GPU	Infiniband
vulcan	246	n0[000-241].vulcan0	INTEL XEON E5530	8	24GB		QDR
		n0[242-245].vulcan0	INTEL XEON E5-2609	8	32GB		QDR
vulcan_gpu	2	n0[246-247].vulcan0	INTEL XEON E5-2650	16	64 GB	4x Tesla K20Xm	
vulcan_c20	28	n0[248-275].vulcan0	INTEL XEON E5-2670 v2	20	64 GB		QDR
vulcan_gpu	2	n0[324-325].vulcan0	INTEL XEON E5-2623 v3	8	64 GB	4x K80	QDR

Figure 2.5: Vulcan cluster: principal technical features such as CPU type, number of core per node and RAM memory per node. Adapted from ref.[94]

Etna

Every node of this cluster is a dual-socket 12-core INTEL Xeon E5-2670 v3 @ 2.30 GHz processors (24 cores in total), 64 GB of physical memory. Nodes communicate to each other through a high performance Mellanox 56 Gbps FDR Infiniband fabric. Figure 2.6 below show node features.

Partition	Nodes	Node List	CPU	Cores	Memory	GPU
etna	172	n0[000-171].etna0	INTEL XEON E5-2670 v3	24	64GB	-
etna	3	n0[172-174].etna0	INTEL XEON E5-2670 v3	24	64GB	Xeon Phi
etna	9	n0[175-183].etna0	INTEL XEON E5-2623 v3	8	64GB	Tesla K80

Figure 2.6: Etna cluster: principal technical features such as CPU type, number of core per node and RAM memory per node. Adapted from ref.[95]

2.3 Experimental Framework

2.3.1 Fabrication

Samples of single layers of graphene were grown on Copper foil by chemical vapour deposition (CVD) technique inside a tube furnace (OTF-1200x-STM, MTI Corp, CA) which is fitted with a scroll vacuum pump.[27,28] The Cu foil was acquired from Lester Metals LLc, Avalon Lake, Ohio, with a purity of 99.99% to produce oxygen-free Cu foil with 0.0005% O content, composed by multi-domains of ~10 μm diameter sized grain boundaries.

Graphene was grown and transferred by following the next process. While Cu foil was heated up to 1000 °C, hydrogen gas was injected at 125 mTorr for 30 min, and subsequently an injection of methane gas at 1.25 Torr for a further 30 min was applied; then the furnace was cooled down to room temperature while the flow of hydrogen and methane remained. Prior to graphene transfer, SiC substrates were solvent-cleaned over 15 min submersion steps through Acetone, Methanol and Isopropyl alcohol sequence. The cleaning and transfer procedures occurred in a class 10000 clean room, with the cleaned substrates being used immediately. Details of growth-transfer process is represented as a flowchart in Figure 2.7.

Thermal release tape (Nitto Americas Inc., CA) has been used to transfer graphene monolayer onto SiC substrates. The tape was placed over the graphene-coated Cu foil. Then, a round metal bar was gently rolled over the thermal release tape to secure the adhesion. Oxygen plasma (35mW/cm^2) was applied on the exposed graphene-side of the Cu foil for 5 min to remove extra graphene and expedite the following chemical Cu etching process. Etching process has followed over the ensemble in a solution of 100 mg/mL $(NH_4)_2S_2O_8$ for 2 hours, then rinsed with
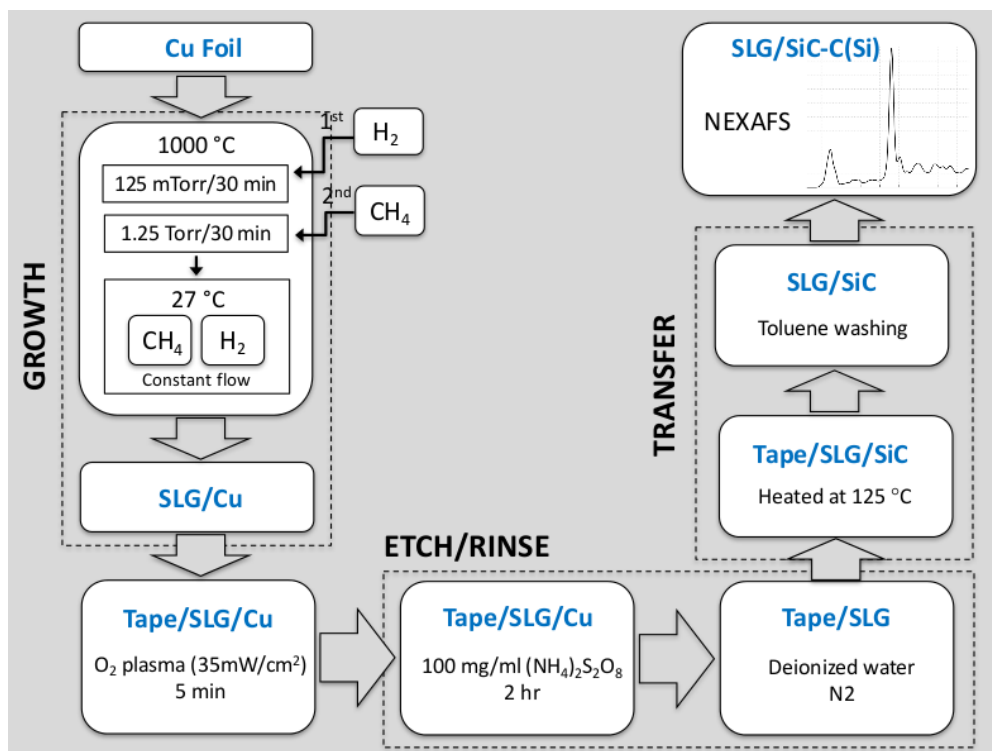
Figure 2.7: Experimental details of the fabrication of graphene on Cu foil surface then transferred to SiC substrate.

deionized water, and dried with dry N_2. The tape/graphene/SiC ensemble was then heated at 125 °C to release the monolayer graphene onto the substrate. As a final step, Toluene washing was applied to the transferred graphene to remove residues from the tape. This process of transferring graphene monolayer was sequentially applied four times to prepare four monolayers graphene onto both Si- and C-terminated SiC substrates. Figure 2.8 provides schematically a picture of the fabrication process described above.

It should be mentioned that quantitative measurements work on quartz crystal microbalance (QCM) for 1 layer to 4-layer thermal released tape transferred CVD-grown graphene confirms that the repetitive graphene transfer used in this work is a reliable process for single layer to multilayer graphene on a hard metal/quartz substrate. Linear fit of 89.1 ng/cm^2 transferred-graphene was in close proximity to a theoretical single layer graphene aerial weight of 76.1 ng/cm^2.[98] Similarly, graphene was also transferred to a SiN transmission electron microscopy grid for further characterization by Helium Ion Microscopy.
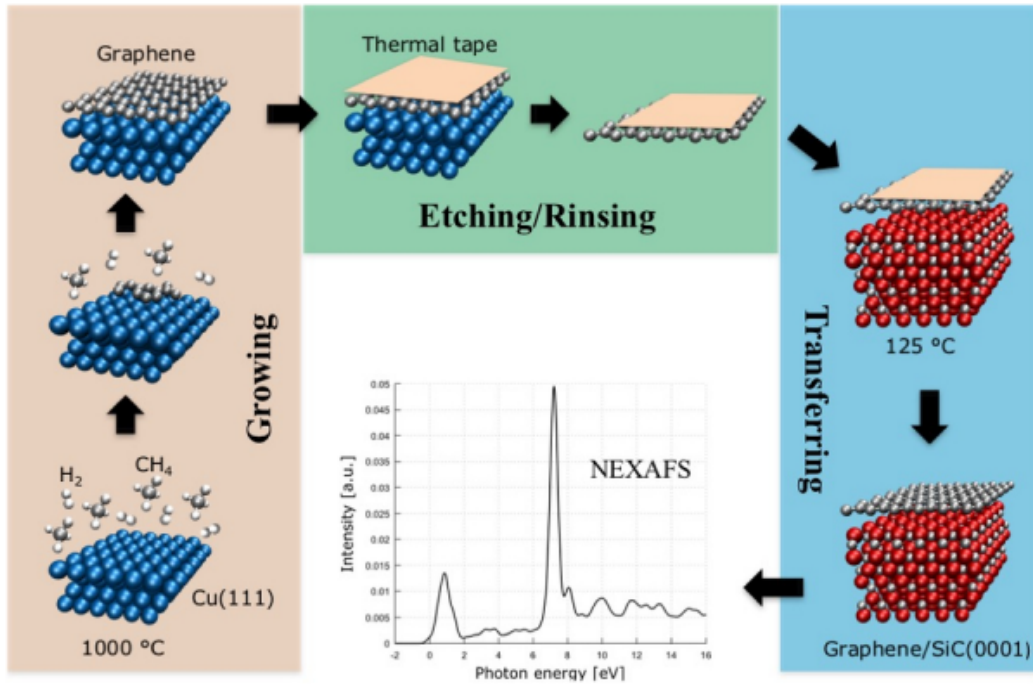
Figure 2.8: Graphic schematic of fabrication-transfer process of graphene on SiC for NEXAFS analysis.

For comparison purposes, epitaxial graphene on SiC was grown on commercial nominally on-axis oriented 6H-SiC (0001) (SiCrystal AG, Germany)-Si surface side. Prior to epitaxy, surface polishing damage was removed through etching in hydrogen for 15 min. at 1 bar and 1550 °C. Epitaxial growth was performed in a vertical cold-wall reactor with a double-walled, water-cooled quartz tube and a graphite susceptor in a slow flow of argon (purity 5.0). Heating and cooling rates were 2–3 °C per second. Typical annealing time was 15 min. Importantly, the choice of this collection of substrates would offer a quantitative framework into the examination of post-processing effects (i.e., transfer process) by comparing epitaxially-grown graphene on SiC with CVD-grown graphene that is later transferred onto SiC substrates. Equivalently, a way to get rid of growth effects where vast intrinsic defects (such as dislocations and vacancies) readily nucleate from growth, as it is the case in epitaxial graphene on SiC. In addition, multiple layer graphene transferred to SiC represents an additional important variable since it is known to enhance conductivity. Findings are extensively discussed in Chapter 3 and Chapter 4.

2.3.2 Characterization

The acquisition of hyperspectral NEXAFS spectra at Carbon K-edge were carried out at NIST Beamline U7A which is equipped with a Large Area Rapid Imaging Analytical Tool detector (LARIAT, Synchrotron Research Inc.) located at the National Synchrotron Light Source, Brookhaven National Laboratory. Data collection for all samples were made at 30°, 45°, 54°, 60°, 75°, 85° and 90° incidence of the X-rays relative to the plane of the sample in partial electron yield (PEY) mode, with energy resolutions of 0.1 or 0.2 eV and polarization of 85% in the horizontal direction. Depth sensitivity of NEXAFS in PEY mode depend on kinetic energies of collected electrons, but can be adjusted in part by the application of a grid bias prior to the detector.[99,100] The grid acts as a high-pass filter, rejecting elastically-scattered electrons with lower energies which are likely to have been emitted from deeper within the sample. C K-edge measurements were performed with a grid bias of -225 V. A lower limit for the depth sensitivity can be taken as the inelastic mean free path of the C KLL signal (E_K=263 eV), which will embrace a significant portion of the detected signal with this grid bias; it is estimated to be 0.7 nm assuming a graphene density of 2.3 g/cm^3.[99] Spectra normalization was performed with the Lariat Data Figure (LDF) software (Synchrotron Research Inc.) and the scanned areas were 5 mm × 3 mm in size.

Micrograph of untreated CVD-grown graphene transferred to SiN grid was imaged with an Helium Ion Microscope (ORION Plus He-IM Zeiss) at 30kV and the assistance of a flood gun was not necessary to prevent surface charging.

2.3.3 Hyperspectral NEXAFS Spectroscopy

The LARIAT detector has a nominal resolution (i.e., pixel size) of ∼40 μm for hyperspectral NEXAFS acquisition, which is advantageous compared to typical 2 mm in standard NEXAFS spectroscopy.[101–103] A description of the chamber is found in Figure 2.10a. Samples on a tilting stage are immersed in a 1 T magnetic field which provides a full-field image ensuring a high collection efficiency by defining electron trajectories. It is the extreme stability of electron trajectories throughout wavelength acquisition frames that enable energy stacking towards full spectrum reconstruction for each pixel (Figure 2.10a). Complete illumination is achieved by photon beam wobbling to irradiate the entire sample area and depth-sensitivity is

controlled by adjusting bias voltage across a grid, acting as a high-pass filter. Additionally, the grid provides a built-in neutralization mechanism, as rejected electrons return to the sample, enabling imaging of insulating systems. After passing through the grid, electrons are incident on a channel plate, whose electron pulses are then impinged on a phosphor-coated optic feedthrough, generating final monochromatic images as the one in Figure 2.10b.
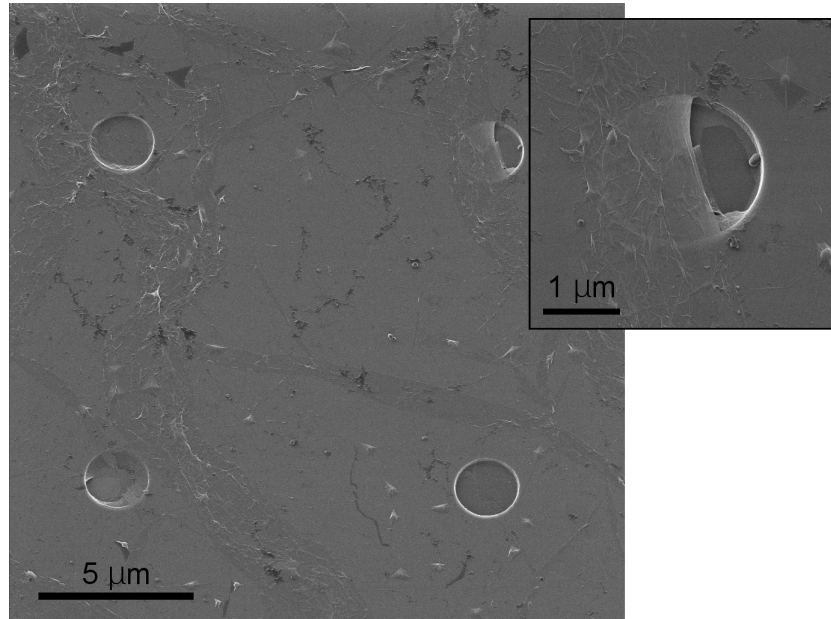
Figure 2.9: Image of graphene placed onto SiN grid taken by an He-Ion Microscope. Ripples of ∼50 nm width are visible throughout the sample.

This detector provides fully resolved spectra per individual image pixels. For instance, in Figure 2.10c it has been plotted spectra extracted from nine selected pixels labeled from pixel 1 to pixel 9 in Figure2.10b. That image corresponds to epitaxial graphene, acquired at glancing incidence (30°). Despite of lower spectral signal respect to noise ratios, the detector captures meaningful spectral variations particularly reflected in π^* lineshapes (around 284.5 eV) thus evidencing the high sensitivity of the detector. Angular stacking procedures can be applied to larger regions of 1 mm × 1 mm, suitable for informing at wafer level. A more detailed explanation of hyperspectral imaging concepts and the needed data analytics will be detailed in Chapter 3.
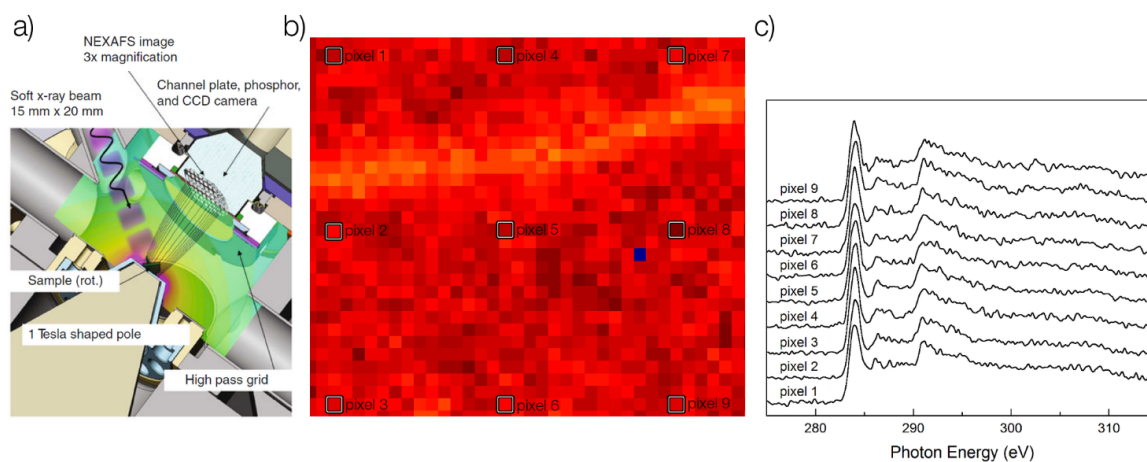
Figure 2.10: (a) Graphic scheme of the LARIAT Mark I detector in the synchrotron chamber.[l] (b) Hyperspectral image at one acquisition angle with a resolution of of $\sim$40 μm (one pixel). (c) Spectra from individual pixels. They have a lower signal to noise ratio, but physically significant spectral variations are observed (in particular for π^* resonances around 285 eV).

3

Monitoring Deformation in Graphene Through Hyperspectral Synchrotron Spectroscopy to Inform Fabrication

3.1 Introduction

As described in Chapter 1, graphene was isolated for the first time in 2004.[4] Since then, it has been subject of broad interest in contemporary research, specially, in silicon industries where fabrication of improved electronic devices are potentially limited by quantum physics laws as they relate to length scales. The outstanding electronic properties of graphene make it an excellent candidate for novel applications in optoelectronics, sensors, and flexible electronic devices.[31,105–107] In fact, 2D materials beyond graphene have made considerable progress in recent years, opening possibilities in photonics with the improvement of advanced terahertz communication.[108–110] Presently, manufacturing of commercial graphene technologies is in its early stages. Even though, high quality graphene can be epitaxially grown on silicon carbide substrates it is still expensive to be massively produced.[30] Further, technology integration imposes conditions on substrate types, resulting in devices whose behavior is governed not only by graphene properties themselves, but also by the characteristics of the desired substrate. The added technological demands require the development of efficient procedures to transfer graphene from the initial growth substrates, typically SiC or copper. The efficiency of these procedures hinders on their ability to preserve intrinsic graphene properties.[111] Thus, characterization of graphene synthesized by affordable methods such as low-cost chemical vapour deposition and later transferred, is of paramount importance. At this

time, predicted prominent electronic properties of exfoliated graphene are far from being reached by current substrate-supported methods, due to the incorporation of defects and perturbations in the pristine sp^2 structure upon processing.[112–114] High-temperature growth and subsequent cooling involved in the fabrication process lead to out-of-plane distortion and in-plane strain.[115,116] Initial deformation occurs when the system is heated up and later upon cooling further deformation is created when the system is compressed due to the lattice parameters mismatch between graphene and substrate. This mismatch is stabilized through the nucleation of intrinsic ripples.[115,117,118] Also, post growth processing introduce additional in-plane strain upon transfer and increase deformation.[118–121] Evidently, the amount of substrates-derived deformation play a key role in transferred graphene.[116] Therefore, these effects are of crucial importance, in particular for electronic applications, as strain fluctuations limit carrier mobility in detriment to operational devices,[116] promoting the need for reliable characterization techniques.

In this chapter, under the Materials by Design approach[61] introduced in Chapter 2, we have used density functional theory simulations to develop a methodology that enables data analytics and information extraction of out-of-plane deformation from a complex material system (deformed graphene on SiC substrates) using sophisticated spectroscopies. The necessity of such combined theoretical and experimental methodology is highlighted here since our findings would not be feasible without such close collaborative.

Overall, the value of theory in this discussion is the feasibility to build two theoretical samples. The first sample, serves as a theoretical graphene standard; i.e., freestanding, unstrained, flat and without impurities. The theoretical standard will be compared to an epitaxially grown graphene on SiC and to 4 samples obtained from CVD method and subsequently transferred to SiC. This sequence will quantitatively address the out-of-plane deformation induced by fabrication first and processing later, through the analysis of hyperspectral NEXAFS spectroscopy focused on the $\pi^*_{C=C}$ resonance.

The second sample features a generic out-of-plane deformation through an asymmetric ripple modeled on a single graphene sheet. These features have been repeatedly observed experimentally, as will be discussed later. Spectroscopy of the theoretical rippled sample, showing variations throughout the rippled area, enables the development of the analysis that follows here.

3.2 Computational Details

A free-standing theoretical graphene primitive unit cell of 2 carbon atoms with lattice parameter of 2.465 Å was relaxed by using plane-wave DFT under the general gradient approximation (GGA) of Perdue-Burke-Ernzerhof (PBE) exchange-correlation functional implemented in the suite Quantum ESPRESSO within the pseudopotential approximation.[122–124] We employed ultrasoft pseudopotentials, energy cutoff of 30 Ry for plane wave basis set and 300 Ry for charge density, a K-sampling grid in the Monkhorst-Pack scheme of $30 \times 30 \times 1$, total energy tolerance of 10^{-6} and vacuum of 20 Å along Z-axis to avoid interactions between periodic images. Atomic forces at equilibrium position were converged below the 0.01 eV/Å threshold.

The input to perform NEXAFS spectra simulations is a periodic 10×10 supercell size containing 200 carbon atoms. *Ab initio* NEXAFS spectroscopy calculations at C K-edge were modeled in the framework of the excited electron and core-hole (XCH) approximation implemented in the code Shirley,[86] and spectra were projected for angles of incidence of 0°, 10°, 20°, 30°, 35°, 40°, 45°, 54°, 60°, 65°, 75°, 85°, and 90° (Figure 3.1). In order to simulate the excitation of the carbon atom due to the X-ray, one electron from the 1s level of the carbon pseudopotential has been removed. One carbon atom from the supercell has been used to calculate the unoccupied states under the pseudopotential approximation that includes the core-hole interaction. XCH-NEXAFS use the PBE form for the exchange-correlation potential within GGA approximation. Supercell's dimensions were large enough to guaranteed non-interaction between adjacent absorbing atoms due to periodic boundary conditions.

3.3 Angle-Resolved Hyperspectral NEXAFS Spectroscopy

The ability of NEXAFS to measure molecular orientation makes it ideal to study deformations in graphene lattice.[112] The out-of-plane perturbation impact over orientation and distribution of orbitals can be monitored by the π^* intensity.[119,125] Remarkably, with the advent of hyperspectral large area detectors such as the large-area rapid imaging analysis tool (LARIAT), large areas at the mm scale can be ex-
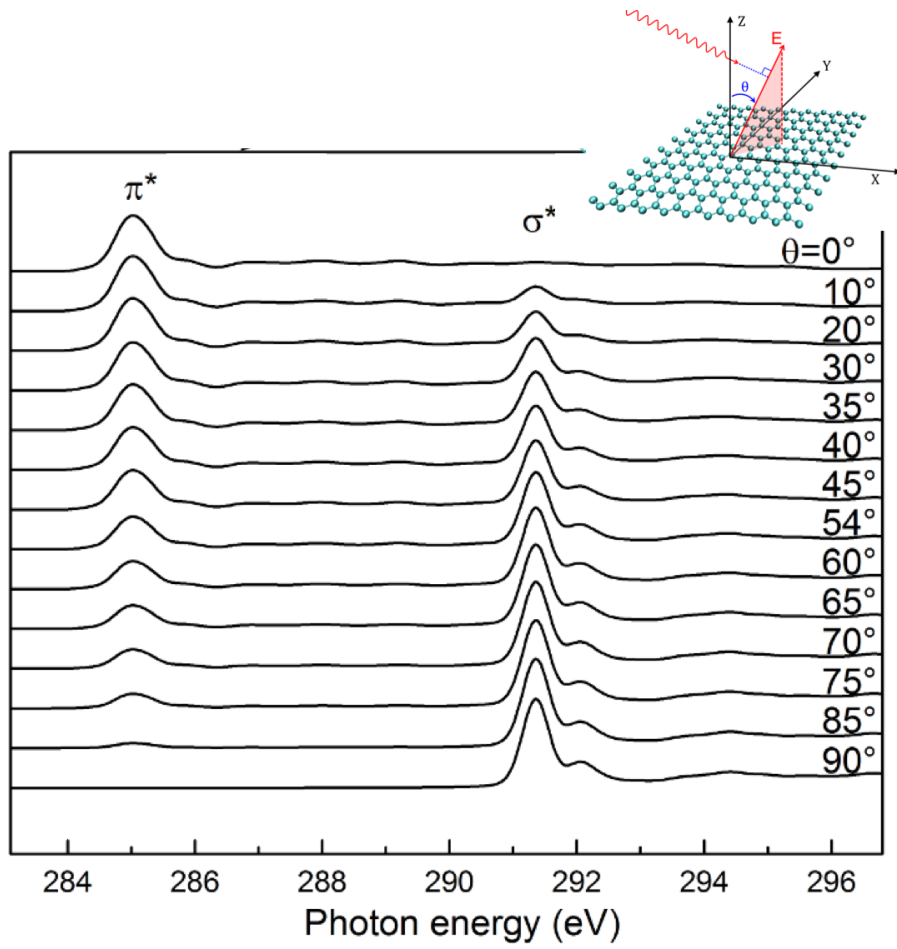
Figure 3.1: Spectra of theoretical graphene projected for various incident angles (θ).

plored by the high sensitivity NEXAFS spectroscopy with resolutions at the micron-scale[104,126] resulting essential toward informing industrial graphene manufacturing.[61,113]

The sample is placed within a uniform 1T magnetic field which confines electron trajectories. The photon beam is wobbled up and down to provide full-field illumination for each incident photon energy then emitted Auger electrons travel along the magnetic field lines, through a high-pass filter and a channel plate, consequently, generated electron pulses are impinged on a phosphor-coated fiber-optic feedthrough, which is imaged with a CCD camera (Figure 3.2a). Fast acquisition of hyperspectral files results in large datasets systems imaged at every energy interval (Figure 3.2b), producing a spectrum corresponding to each pixel which specific
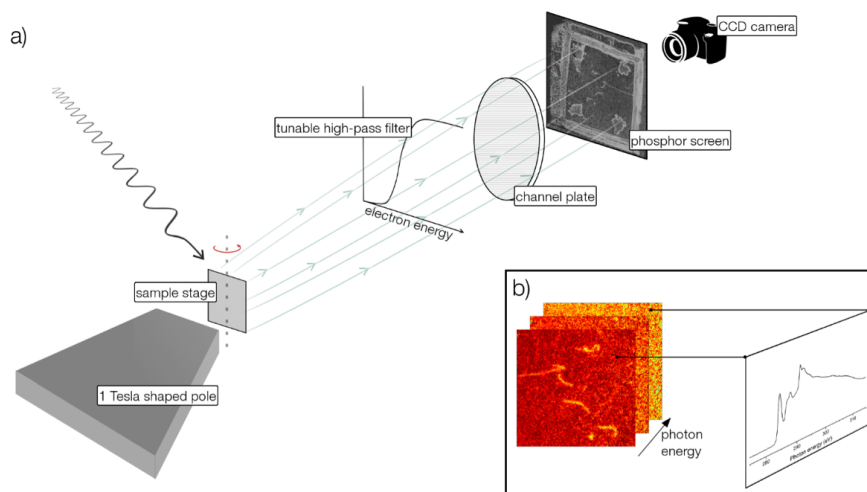
Figure 3.2: (a) Schematic drawing of experimental setup for Hyperspectral NEXAFS acquisition (LARIAT I). (b) The sample is imaged at each photon energy interval where each pixel in the stack represents an individual spectrum.

data treatment toward adequate exploitation is needed. In this work, data reduction toward information extraction yielding an out-of-plane deformation parameter is performed.

To this end, the ability to collect data at various incidence angles by tilting the sample stage offers a unique opportunity to study the spatial distribution of out-of-plane deformation in angle-resolved images, as shown in Figure 3.3a.[119] Nevertheless, for hyperspectral detection, perspective distortions in images resulting from stage tilting need to be corrected in order to perform accurate angular characterization of particular region of interests (ROIs). This is achieved by fiducial mark alignment in images throughout all angular acquisitions (Figure 3.3b), which is performed by the LDF software.
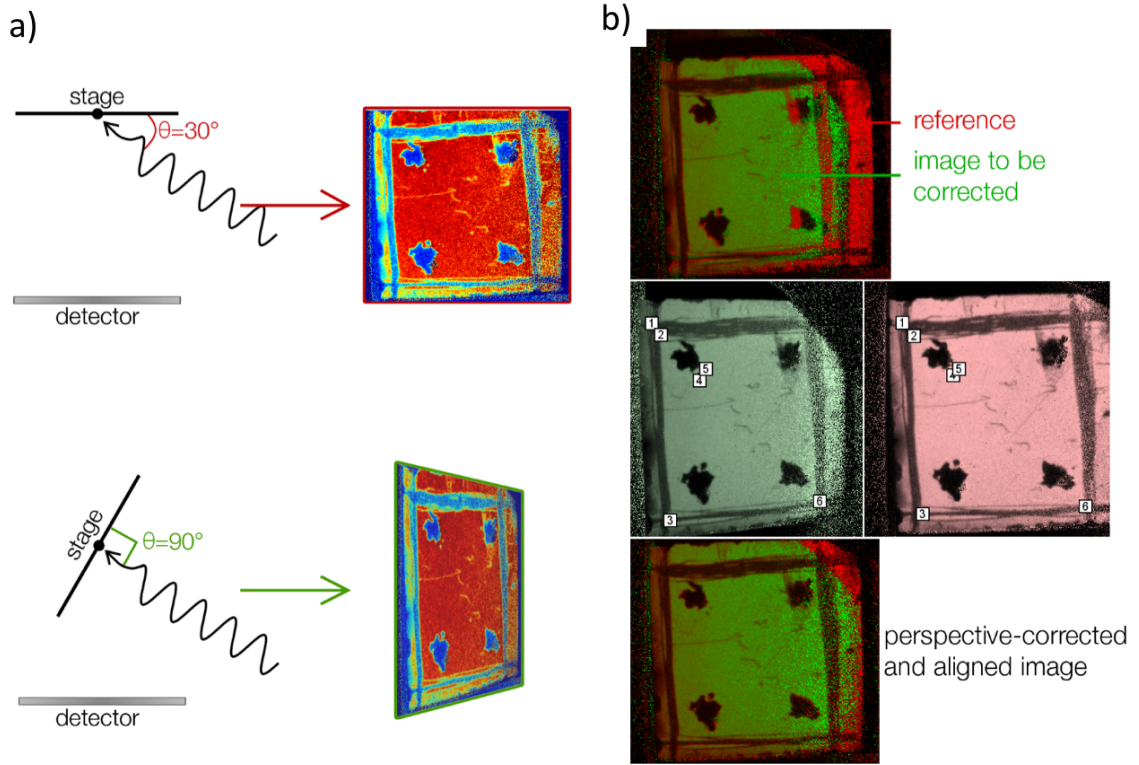
Figure 3.3: (a) Tilting the stage to acquire NEXAFS at various angles results in spatially uncorrelated stacks. (b) Stacks from different angular acquisitions are manually corrected by correlating pixels to a reference using the LDF software.

The procedure of perspective correction on images, which enables precise ROI correlation between angular acquisitions and NEXAFS scans of graphene systems under study, results in a hyperspectral energy-angle superstack: a spatially linked series of hyperspectral energy stacks ("stacks" henceforth for the sake of simplicity) for every system (Figure 3.4a). In each superstack, we ensure that spectra are extracted from identical areas throughout angular acquisitions (Figure 3.4b). Superstacks are thus functions of spatial X and Y coordinates, photon energy, intensity, and acquisition angle.

For the analysis of out-of-plane deformation it is necessary to establish a baseline which excludes all angular-independent contributions.[127] Hyperspectral NEXAFS maps of SLG/SiC-Si, SLG/SiC-C, 4LG/SiC-Si, 4LG/SiC-C (Figure 3.5a-d), and epitaxial graphene (Figure 3.5e) were acquired at various incidence angles, following the procedure in Figure 3.4a. Images in Figure 3.5a-d correspond to the 1s
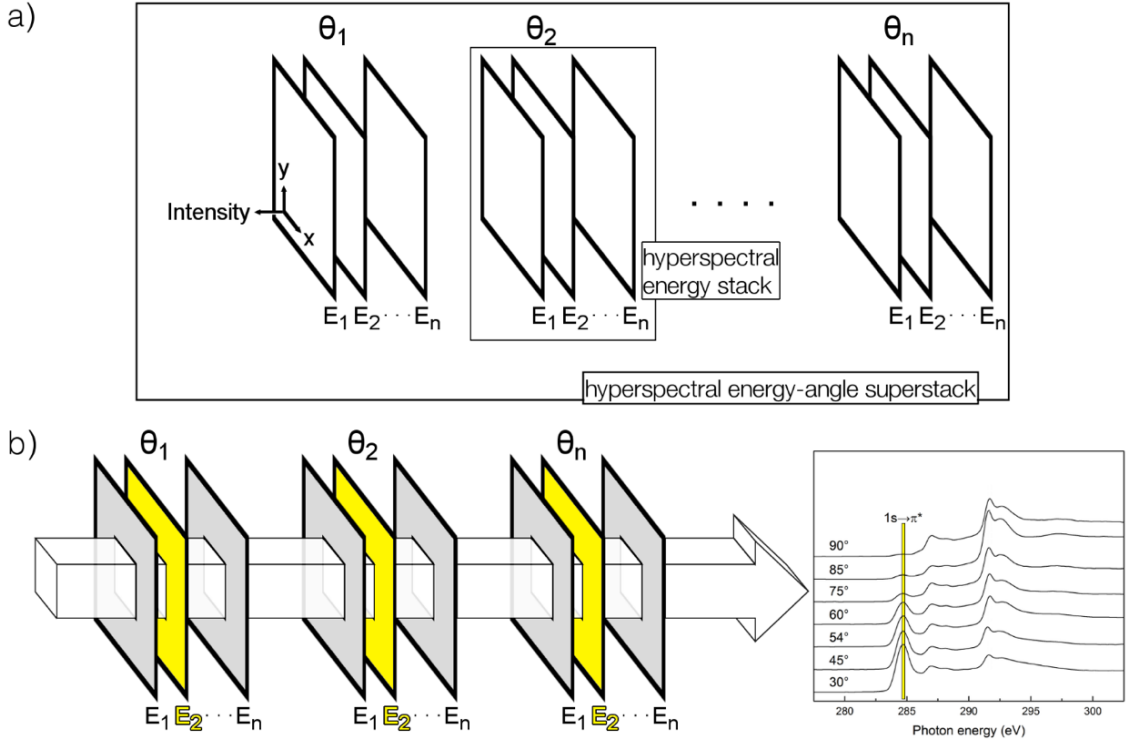
Figure 3.4: (a) Post-correction, a hyperspectral energy-angle superstack is assembled for each experimental system, consisting of a hyperspectral energy stack for every acquisition angle. (b) Schematic representation of data extraction: angular spectra acquired from a precise area in a graphene system, with energy E_2 representing the π^* resonance.

$\to \pi^*$ excitation around 284.7 eV, taken from the 30° stacks, where these features show highest π^* intensities for flat graphene.[128] Fully extracted experimental spectra from Figure 3.5a-d (transferred graphene) and Figure 3.5e (epitaxial graphene) as well as the theoretical standard spectra, are shown in Figure 3.6. Angular intensity trends are shown in Figure 3.6, which will be investigated toward out-of-plane deformation analysis. Importantly, $\pi^*_{C=C}$ resonance intensities (at 284.7 eV) are minimal when the incoming beam is at 90° to the substrate, and increase with incidence angle, whereas, σ^*_{C-C} resonance intensities (at ~291 eV) exhibit the opposite trend, validating predominantly flat graphene.[128] SLG/SiC-C is not considered in our data analysis due to its low variability on $\pi^*_{C=C}$ resonances.
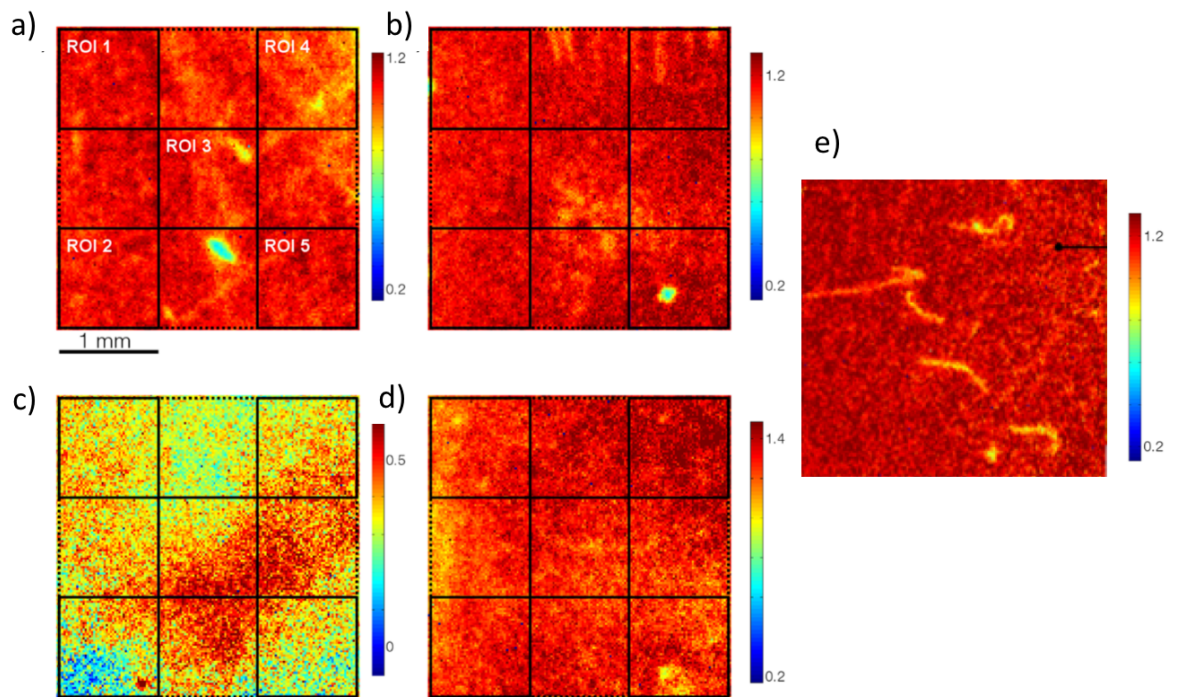
Figure 3.5: Images were tuned around 284.7 eV, and acquired at 30°, rendering intense π^* resonances. ROIs are 1 mm × 1 mm, and each pixel is ∼40 μm. (a) SLG/SiC-Si. (b) 4LG/SiC-Si. (c) SLG/SiC-C. (d) 4LG/SiC-C. (e) Epitaxially grown graphene.
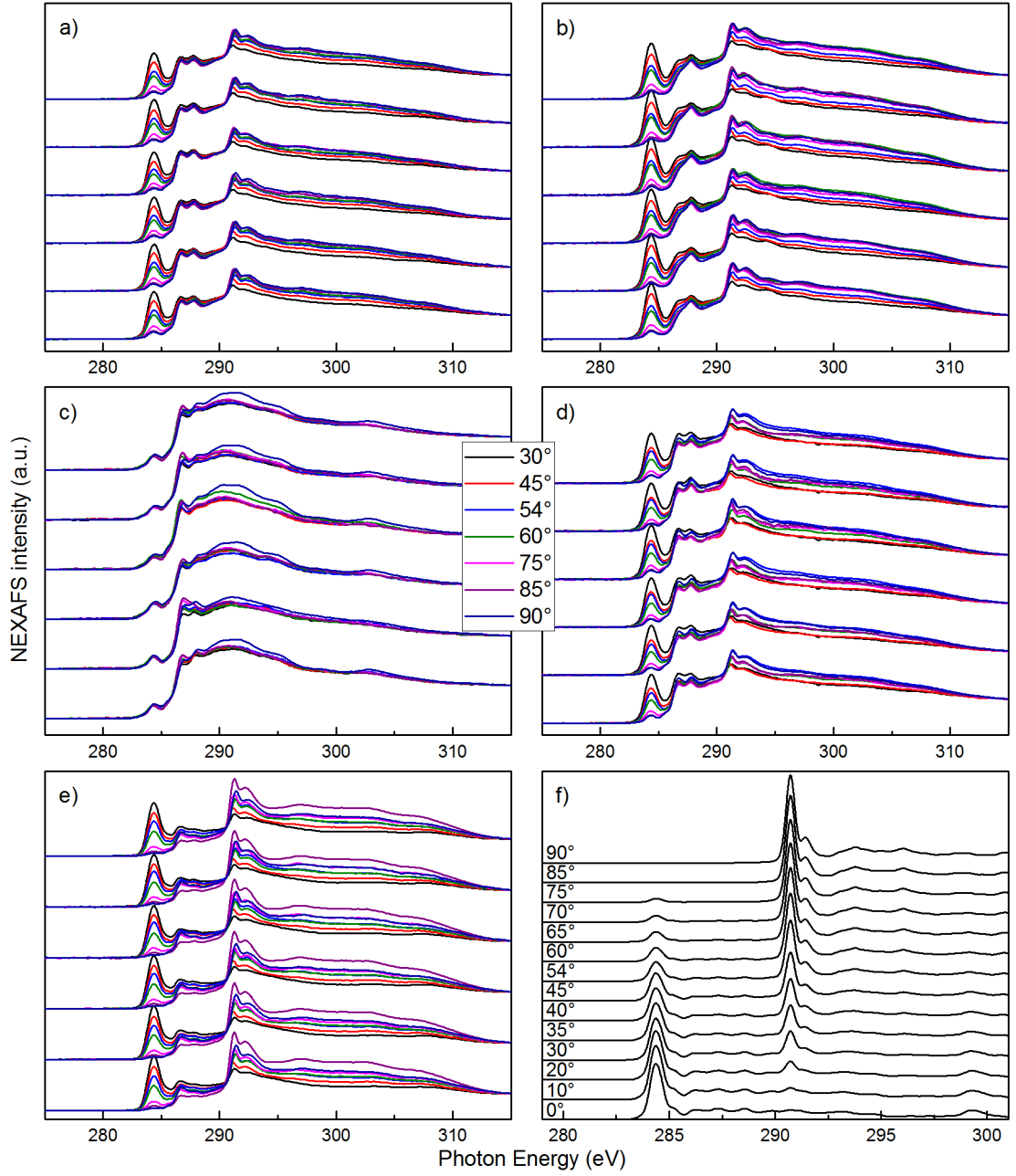
Figure 3.6: Extracted angle-resolved carbon K-edge NEXAFS spectra. (a) SLG/SiC-Si. (b) 4LG/SiC-Si. (c) SLG/SiC-C. (d) 4LG/SiC-C. (e) Epitaxial graphene. (f) Theoretical freestanding graphene.

3.4 Dichroic Ratio

A typical method for semi-quantitatively determining of out-of-plane deformation in graphene is the dichroic ratio (DR). It compares intensities at orthogonal acquisition angles, and is calculated by the equation 3.1.[119,129]

$$DR = \frac{(I_{90°} - I_{0°})}{(I_{90°} + I_{0°})} \tag{3.1}$$

In principle, DR can be applied to π^* and σ^* resonances given that they follow linear and orthogonal trends with $\cos^2 \theta$ and $\sin^2 \theta$, respectively.[130] However, the presence of carbonaceous impurities adsorbed on experimental samples add complexity to the analysis of σ^* resonances, therefore, only π^* intensities are used here. According to equation 3.1, DR = -1 result from a system with π^* orbitals perfectly oriented normal to the plane (as in pristine graphene) and DR = 0 for isotropically arranged orbitals.

Figure3.7a shows fitted π^* resonances of theoretical graphene and experimental spectra extracted from 3 mm $\times$ 3 mm ROIs. As expected, the theoretical standard confirms a DR of -1 for pristine graphene. Results displayed in Table 3.1 indicate that epitaxial graphene has the largest deformation, yielding the lowest numerical value of DR, while 4LG/SiC-C has the least deformation, with the highest DR followed by both SLG/SiC-Si and 4LG/SiC-Si, rendering identical DRs. The difference in ratios between all systems (and ROIs within systems) is low, however, suggesting lack of molecular sensitivity for this method at these high extents of substrate alignment. In fact, every ROI in SLG/SiC-Si resulted in DR = -0.94, while significant differences are observed in the π^* image for that system in Figure3.5a. Being insensitive to fine out-of-plane deformation at the length-scale under study, DR can only provide a descriptive indication of relative π^* orbital alignment. Thus, the method is unsuitable for comprehensive analytics at wafer level and another sensitive approach: "Orbital Method Approximation" will be discussed in the next section.
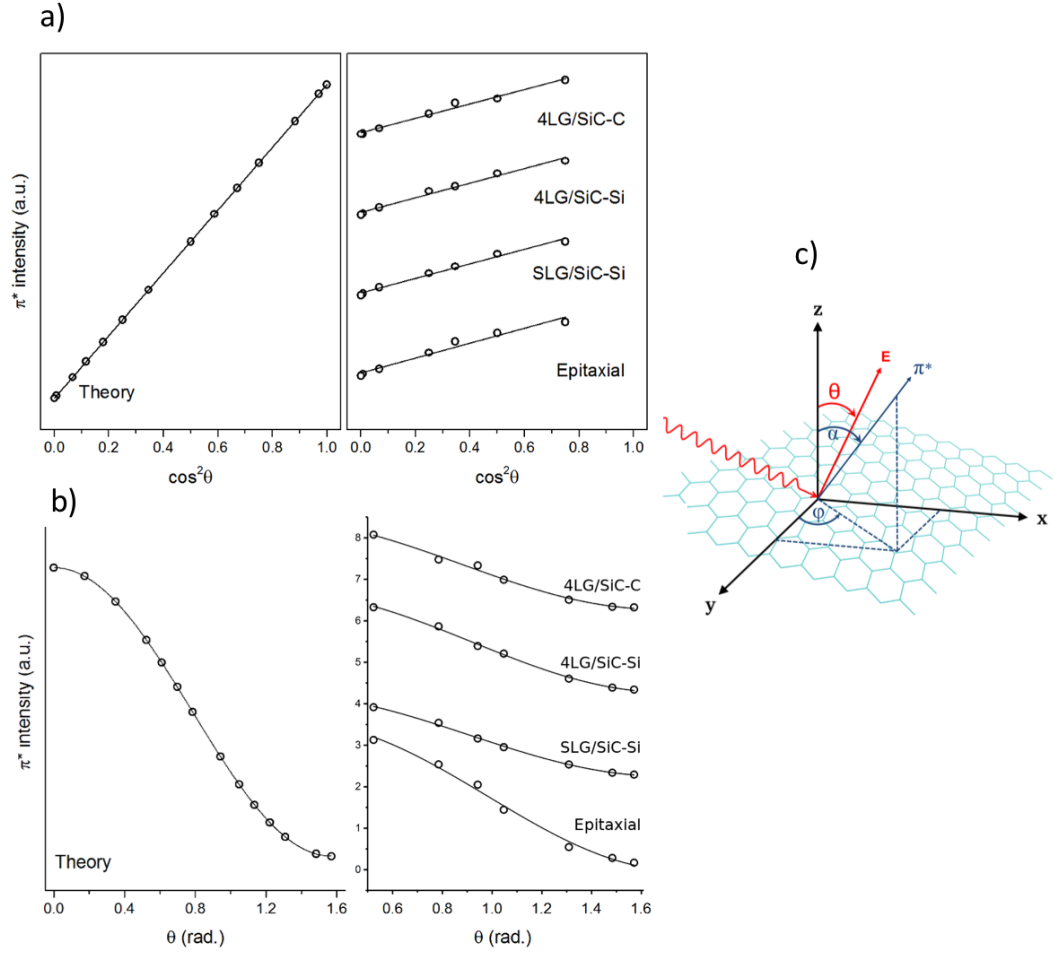
Figure 3.7: For theoretical graphene, epitaxial graphene, SLG/SiC-Si, 4LG/SiC-Si, and 4LG/SiC-C computed from 3 mm × 3 mm ROIs. (a) Dichroic ratios (Table 3.1). (b) π^* intensities fitted with equation 3.2 (Table 3.2). (c) Geometric definitions show π^* vector described by angles α and φ to be used in the orbital vector approximation.

System	ROI	DR
Theoretical graphene	-	-1.00
Epitaxial graphene	1	-0.93
	2	-0.94
	3	-0.93
	4	-0.92
	5	-0.92
	3 mm	-0.93
SLG/SiC-Si	1	-0.94
	2	-0.94
	3	-0.94
	4	-0.94
	5	-0.94
	3 mm	-0.94
4LG/SiC-Si	1	-0.94
	2	-0.95
	3	-0.96
	4	-0.93
	5	-0.93
	3 mm	-0.94
4LG/SiC-C	1	-0.97
	2	-0.97
	3	-0.96
	4	-0.95
	5	-0.95
	3 mm	-0.97

Table 3.1: Dichroic Ratios.

System	ROI	$\alpha(°)$	R^2	mean	s.d.	c	R^2	mean	s.d.
Theoretical graphene	-	0	1	0	0	0	1	0	0
Epitaxial graphene	1	10.8	0.9943			-0.035	0.9942		
	2	10	0.9936			0.006	0.9936		
	3	11.8	0.9909	11.66	1.27	-0.037	0.9908	-0.0366	0.0120
	4	12.8	0.9896			-0.063	0.9896		
	5	12.9	0.9904			-0.054	0.9904		
	3 mm	11.3	0.9927			-0.028	0.9927		
SLG/SiC-Si	1	8.1	0.9990			0.239	0.9990		
	2	8	0.9983			0.248	0.9983		
	3	6.9	0.9986	7.19	0.87	0.260	0.9987	0.2520	0.0086
	4	6	0.9992			0.254	0.9992		
	5	6.9	0.9998			0.259	0.9999		
	3 mm	7.1	0.9983			0.255	0.9983		
4LG/SiC-Si	1	8.1	0.9970			0.253	0.9970		
	2	7.6	0.9967			0.269	0.9967		
	3	6.7	0.9981	7.61	0.59	0.325	0.9981	0.2883	0.0282
	4	8.1	0.9975			0.303	0.9975		
	5	7.6	0.9974			0.291	0.9974		
	3 mm	7.8	0.9979			0.275	0.9978		
4LGSiC-C	1	4.4	0.9954			0.293	0.9954		
	2	4.4	0.9942			0.274	0.9942		
	3	6.4	0.9884	5.63	1.09	0.278	0.9884	0.2852	0.0222
	4	6.3	0.9916			0.320	0.9916		
	5	6.6	0.9881			0.261	0.9881		
	3 mm	5.4	0.9917			0.281	0.9917		

Table 3.2: Results of Orbital Vector Approximation Method according to equation 3.2.[b]

---

[b]Here, π^* resonances from representative 3 mm ROI from each system and the vector approximation fits are shown in Figure 3.7b.

3.5 Orbital Vector Approximation for Detecting Ripples in Graphene

Orientation and alignment of small molecules can be quantitatively determined by categorizing π^* and σ^* orbitals as either vectors or planes, according to their geometry.[85,127,131,132] In this model, π^* orbitals in graphene are vectors normal to the plane. In systems with 3-fold or higher symmetry, equation 3.2 dictates the correlation between NEXAFS intensities of orbitals and acquisition angle θ, with α as the polar angle of the vector-like orbital displayed in Figure 3.7c. Due to symmetry reasons the azimuth φ is absent in the equation 3.2.

Indeed, a single layer of graphene will result in one single orientation with respect to the substrate upon transfer. Under the assumption, the Orbital Vector Approximation has been applied to the graphene systems under study. As a first approximation, ignoring local perturbations from rippling that will be modelled through α, the azimuth angle was set to zero. Also, parameter c was included to account for π^* intensity variations in highly delocalized systems which combine with additional signals provided by adjacent unperturbed areas.[c]

$$I(\theta) = A(\cos^2\theta\cos^2\alpha + \sin^2\theta\sin^2\alpha + 2\sin\alpha\cos\alpha\sin\theta\cos\theta) + c \qquad (3.2)$$

In Figure 3.8a a Helium-ion microscopy image of a single graphene layer shows out-of-plane deformations of a predominantly flat graphene. Figure 3.8b are line profiles of selected features from insets in Figure 3.8a that reveal asymmetric geometries. To examine ripple deformation, an asymmetric ripple was modelled (Figure 3.6c) and applied the orbital vector approximation method (Figure 3.6d) on several atoms highlighted as blue (labeled from 1 to 10) in Figure 3.6c. According to Table 3.3, individual atoms produced values of α ranging from -3.6° to 6.3° and an average NEXAFS spectrum gave α of -0.96°, which is the average of individual α values. Notably, these results strongly suggest that the orbital vector approximation is promising in the characterization of rippling effects in graphene, where α

---

[c]Fully derivation of Equation 3.2 is found in chapter 9 "The Angular Dependence of Resonance Intensities" from Stöhr's book.[85] To obtain this particular expression, we should note that: (i) Terms associated with the azimuth angle are neglected due to symmetry, i.e., $\varphi = 0$, and (ii) It was assumed a perfectly polarized beam, i.e., P=1, for better comparison with simulated data.

and c are providing physical interpretation on frequency and intensity of rippling feature.
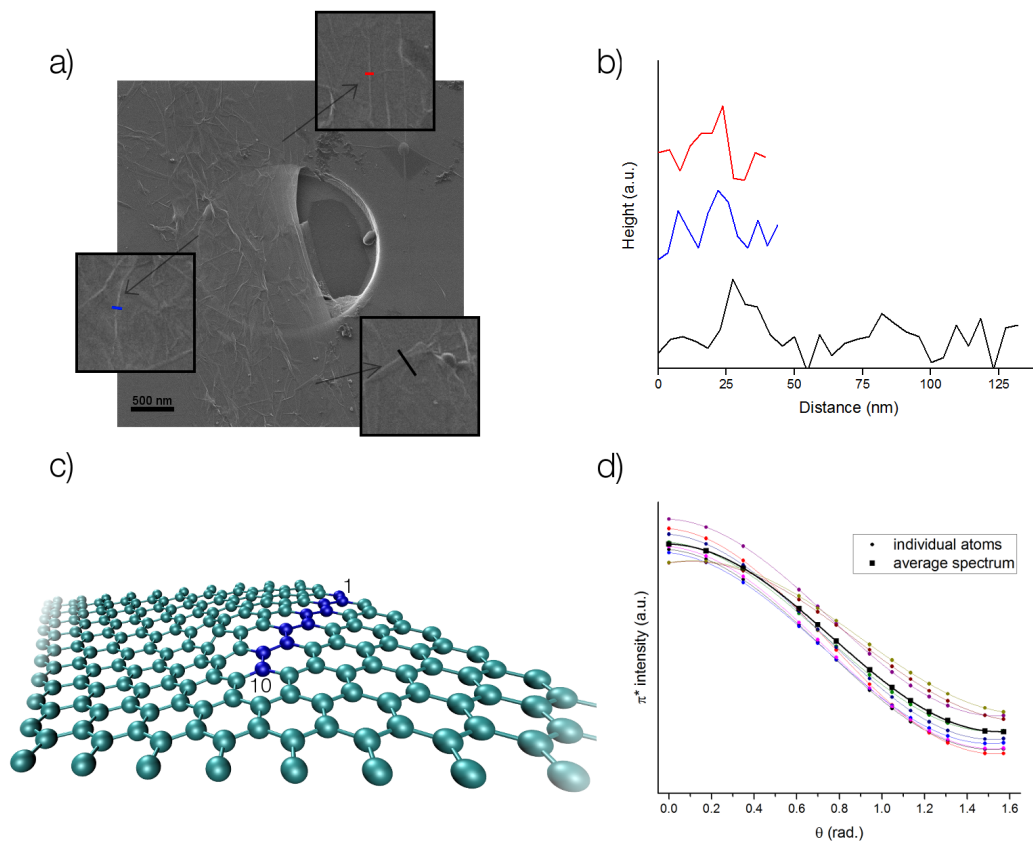
Figure 3.8: (a) Helium Ion microscopy micrograph of a single graphene layer. (b) Line profiles of 3 asymmetric ripples from inset in (a). (c) Asymmetric ripple modeled on a single graphene sheet. (d) Angle-resolved π^* intensities of individual blue carbon atoms and average intensities fitted with Eq. 3.2. Average of individual atoms yielded α = -0.96°, therefore, asymmetric ripples will be detected by the orbital vector approximation.

As expected, α = c = 0 is obtained for π^* intensities of modelled flat graphene (see Figure 3.7b). Similarly, Figure 3.7b shows experimental samples fitted with equation 3.2[d]. It has been shown that extraction of π^* intensities from NEXAFS spectra is sensitive to the incorporation of small errors resulting in significant changes on α value.[133] However, α and c values measured from different ROIs form distinct clusters for each experimental graphene system (Table 3.2). α parameters from each analyzed ROI are represented in Figure 3.9.

[d]Equation 3.2 was fitted in OriginPro 9, using the Levenberg-Marquardt algorithm.

Carbon atom	$\alpha(°)$
1	-3.11
2	-2.27
3	-3.58
4	-2.85
5	-2.97
6	-3.08
7	-1.89
8	-1.89
9	5.81
10	6.33
Average	-0.96

Table 3.3: α for individual carbon atoms along ripple modelled in Figure 3.8c, and α for corresponding average spectrum.

Design and implementation of reductive analytic methods is very important for optimization in data acquisition and data processing. From that perspective, data treatment routine suitable for incorporation in large area substrates and high throughput industrial environments is designed in this work (Figure 3.9), where an analytic comparison of selected 1 mm $\times$ 1 mm ROIs against overall 3 mm $\times$ 3 mm ROIs (Figure 3.9a) is performed. In this design, a zero-level data reduction (integration) represents the capabilities of traditional NEXAFS spectroscopy, where the complete bulk data is analyzed, hence taxing manufacturing decision making turnaround. Corrugation map displayed in Figure 3.9b has been built from α values as a result of analysis of the whole scanned area (3 mm $\times$ 3 mm ROIs). At this length scale and in agreement with the dichroic ratio, the interpretation of this zero-level data reduction implies that system with the most out-of-plane distortion is epitaxial graphene, followed by 4LG/SiC-Si, SLG/SiC-Si, and 4LG/SiC-C with decreasing α, as systems with less out-of-plane deformation.

This method proves to be significantly more sensitive to corrugation variations contrary to DR method. Actually, this sensitivity seems to be enhanced by α versus c variations. In fact, only meaningful variation arises from comparing the c values between epitaxial and transferred, as shown in Table 3.2. Analogously to the α parameter treatment, individual c values are provided for the 5 ROIs in each sample, as well as, corresponding mean and standard deviation. For transferred systems, mean c values overlap within the brackets of their standard variation, as seen in Table 3.2, also net variation is observed between the lower c values of epitaxial and the higher c values from transferred systems, as a collective. Given the increased sensitivity of α values, further data analytics have been deployed with the purpose of increasing information output from this data set.

For the upcoming analysis we have only considered α values resulting from analysis of 1 mm × 1 mm ROIs (non-shaded areas in Figure 3.9a). In other words, we have discretized the entire scanned area, ROIs 1–5 in each sample from which values of α has been obtained and mapped in Figure 3.9c, namely first-level data reduction (segmentation), consistent with the data discussed in ROIs 1–5 in Table 3.3. This segmentation reveals sensitivity enhancement to corrugation variations compared to DR, most pronounced in SLG/SiC-Si, where every ROI produced the same DR, but different α. In Figure 3.9d a second-level data reduction has been proposed here (extrapolation). In this case, the segmented analysis from Figure 3.9c is extrapolated from discretized 1 mm × 1 mm ROIs to the entire 3 mm × 3 mm ROI. A direct comparison between integration (Figure 3.9b) and extrapolation (Figure 3.9d) analysis lead to the conclusion that data segmentation has successfully reduced data load but still informing on the overall 3 mm × 3 mm ROI (validation). Mean αs and standard deviations were computed from α values at ROIs 1–5 and shown in Figure 3.9d as well.
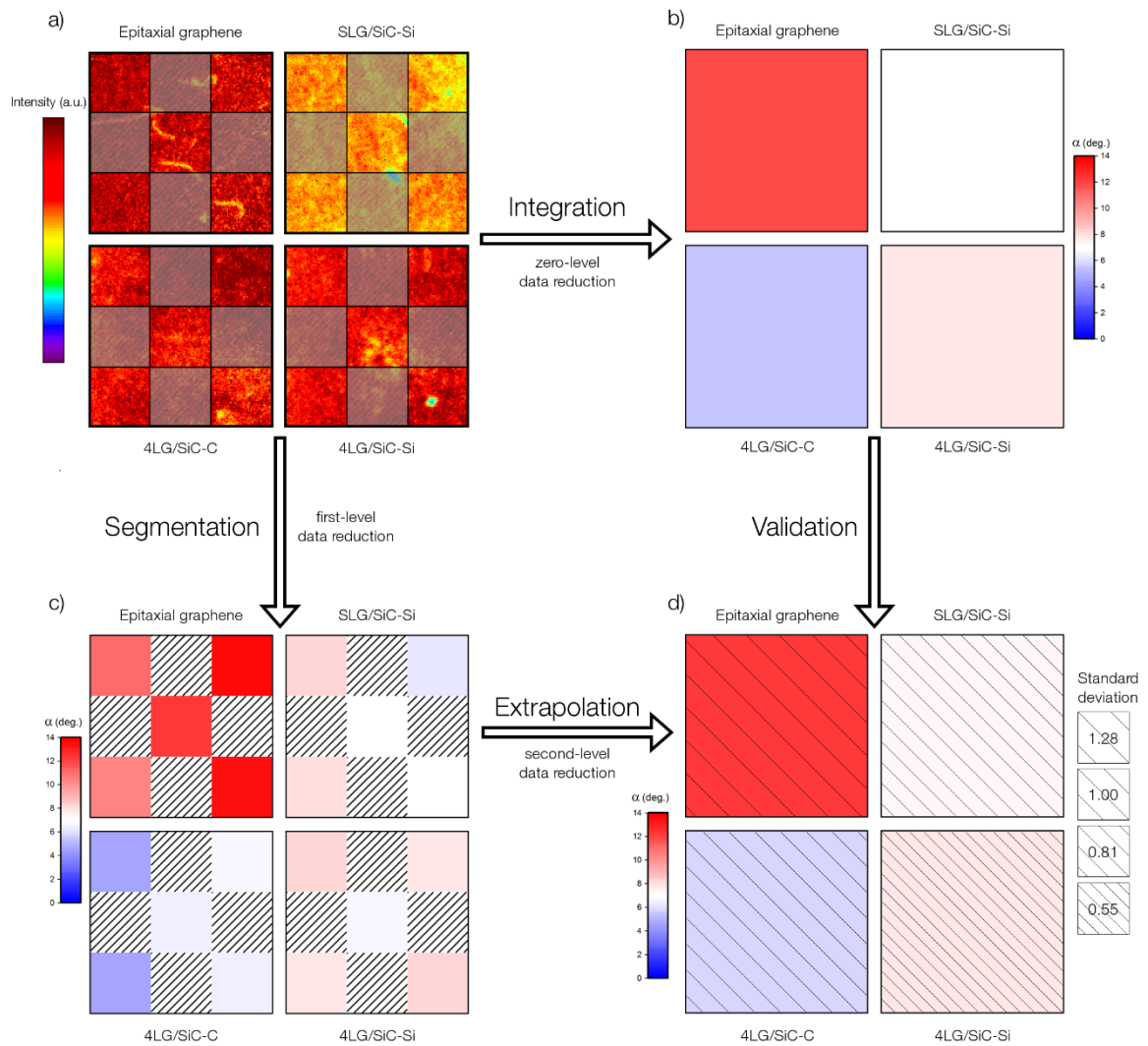
Figure 3.9: α maps built from orbital vector approximation results. (a) NEXAFS π^* intensities. (b) αs from 3 mm × 3 mm ROIs (zero-level data reduction). (c) αs from 1 to 5 ROIs (first-level data reduction). (d) mean αs and standard deviations from 1 to 5 ROIs (second-level data reduction). Intensity scale is 0–1.9 in (a) for epitaxial graphene, and 0–1.4 for the other three systems.

From analytic data treatment in Figure 3.9 we observed an evident compensation in terms of choice of target substrate. In absolute terms, 4LG/SiC-C exhibits the least corrugation and homogeneity across the wafer; conversely, SLG/SiC-Si and 4LG/SiC-Si show more corrugation and the most homogeneous deformation distribution. Nevertheless, graphene growth on both SiC terminations is well documented,[111] importance of substrate termination upon graphene transfer, with a homogeneous but higher corrugation level for Si-termination on a four-layer transfer, is highlighted here. As seen, α reveals some level of information on frequency and intensity of local flat areas intertwined with ripples. Although, definitely lower values of α is desired, as proven by modelled graphene, we believe that increment of α in graphene can be due to higher frequency of occurrences on corrugations rather than intensity of them. In fact, scratches observed in ROI 3 and 5 in epitaxial graphene do not have a large impact in the overall α compared to ROI 2, with less frequent scratches, as seen in Figure 3.9c.

3.6   Unsupervised Machine Learning Analysis

In this section, we applied the Density-Based Spatial Clustering of Applications with Noise (DBSCAN) algorithm[69] to carry out unsupervised machine learning investigation on areas larger than 3 mm × 3 mm. Robustness to noise and minimal pre-knowledge of the system under study are important features of DBSCAN. Although, previous studies employed effectively this unsupervised data mining technique to hard X-ray XANES of $Nd_2Fe_{14}B$,[134] here we apply it to soft X-ray hyperspectral NEXAFS images to cluster based on pixel π^* intensities acquired at 30°. As preparation for data mining analysis, images stacks were cropped and normalized with TXM Wizard.[135] In Figure 3.10 are presented DBSCAN maps and spectra of resulting clusters, where spectrum in blue (highest π^* intensity) indicates the most pristine graphene.

We observed in epitaxial graphene (top-left image in Figure 3.10) some well defined scratches-like features attributed likely to processing derived in localized reorientations, hence favouring lower π^* intensities (red spectrum). Also, dense mixture of blue and red clusters is observed for the most part of epitaxial graphene, implying that out-of-plane perturbations (ripples) have lenghtscales under the detector resolution (40 μm) and that occurrences are very frequent.[115,121] In addition, since each pixel is assigned a fraction weight of each cluster, each pixel is rated

higher or lower quality depending on the frequency of inner-pixel defects. It is also observed that there are no areas of a single cluster, which is consistent with results from DR and orbital vector approximation methods. Therefore, this demonstrates that epitaxial graphene is the least pristine in terms of rippling which were originated during the cooling-down stage. In fact, it has shown that SiC substrates contains many terraces of a 0.5 nm typical step-height inducing deformation of π electronic states during epitaxially grow of graphene.[30]
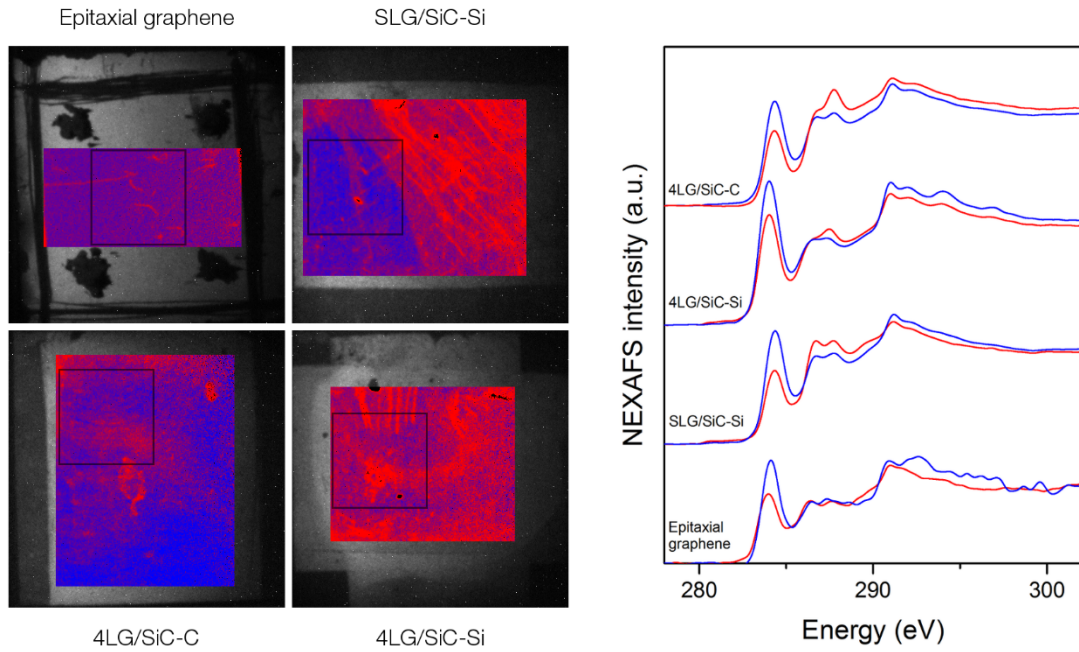
Figure 3.10: DBSCAN clustering based on π^* intensity. Cluster maps indicate 4LG/SiC-C has the most pristine graphene. Maps also suggest two distinct length scales of out-of-plane deformations. Black squares indicate the location of 3 mm × 3 mm ROIs.

Analysis of cluster maps on Si-terminated transferred samples exhibit well defined phases. Although, maps are predominantly red which indicates least pristine graphene, the clusters are well segregated, suggesting local homogeneity contrary to epitaxial graphene. Moreover, inner red clusters, lines uniformly arranged are observed, revealing ripples of 100 μm, possible formed by either imperfect graphene-substrate contact during transfer or by water drain channels during etching and rinsing.[121,136] In fact, contrast of ripple size between epitaxial and transferred graphene suggest that it is frequency of ripples, rather than ripple magnitude, that contributed to α in the orbital vector approximation method. Similarly,

given the reverse behaviour of the c parameter, where c values increase with the level of processing, and since both c and α parameters provide some measure information on ripple magnitude and frequency; data suggest that the c parameter could be preferentially informing on ripple magnitude. Cluster map of 4LG/SiC-C is dominated by the blue cluster (highest π^* intensity) suggesting that it is the most pristine graphene sample in terms of ripples. Notice as well that ripples seen in SLG/SiC-Si and 4LG/SiC-Si do not appear in 4LG/SiC-C. These observations are in agreement with findings from the prior methods, where 4LG/SiC-C resulted in both the lowest dichroic ratio, and lowest α.

Analysis reported here complete the structure-property description of α, which follows the same dependence as mobility on defect frequency rather than size and therefore becomes a good candidate to correlate deformation and performance at wafer scale with molecular sensitivity.

3.7 Summary

We have employed a combination of experimental hyperspectral NEXAFS data and first-principles calculations to investigate data treatment methods for characterization of out-of-plane deformation in graphene. We found that the orbital vector approximation method is significantly more sensitive to fine-scale corrugation. All techniques studied here agree that the specific epitaxial graphene sample studied here, is the most defective and 4LG/SiC-C the most pristine. Indeed, DBSCAN not only confirmed the results, but also revealed different deformation length-scales, leading to the conclusion that α in the orbital vector approximation are more affected by frequency of defects rather than by their magnitude, in good agreement with the reported phenomena behind carrier mobility in graphene. These findings pave the way toward the correlation of out-of-plane strain and carrier mobility through the assessment of the parameter α in a high throughput mode at wafer scales. In addition, effective development of methodology proposed in this chapter requires further characterization of theoretical and experimental standards to build a database for adequate discrimination of out-of-plane deformations through a multiplicity of layers in graphene and other 2D materials.

The next chapter will focus on the capability of combined theoretical and experimental spectroscopic approaches to address in-plane deformation within the same experimental samples analyzed here.

4

Strain and Bond Length Dynamics upon Growth and Transfer of Graphene by NEXAFS Spectroscopy

4.1 Introduction

As discussed in Chapter 1, graphite exfoliated graphene yields unprecedented high electric mobilities, still not having met the theoretical predictions.[106] It was also discussed earlier how industrial-scale fabrication of novel electronic devices would benefit from such transport properties, although challenges remain, rendering this technology far from full commercialization.[137] Indeed, challenges revolve around synthesizing large area, defect-free graphene and subsequently transferred onto desired substrates.[138,139] And in fact, strain (in-plane) and ripples (out-of-plane) derived from processing have been identified as dominant disorder agents which induce random strain fluctuations in graphene devices.[116] Both strain and ripples are first generated during growth, mainly due to thermal mismatch between metal substrates and graphene,[115] and later during transfer.[115] In the last few years, the promise of low cost production of large area graphene by CVD techniques on Cu foils,[27,140] has boosted investigations on more effective growth and transfer approaches aiming at reducing mechanically growth-derived strain and ripples, impurities (adsorbed atoms and/or molecules), as well as other structural defects.[141,142] Nevertheless, CVD-grown graphene is still lacking the high quality achieved by epitaxially-grown graphene on SiC.[30,143] Indeed, investigations that correlate electronic conductivity of graphene with degree of corrugation varied from wide (135 nm) to narrow (16 nm) wrinkles with reported heights of up to 6 nm.[136]

At present, instrumentation and analytic capabilities for morphological analysis include Transmission Electron Microscopy (TEM) and Scanning Tunnel Microscopy (STM). Spectral analysis commonly feature Low Energy Electron Diffraction (LEED), Raman, and Synchrotron techniques, that are suitable to characterize mechanical deformation in graphene.[111] As discussed in the previous chapter, NEXAFS spectroscopy recently has been highlighted to study graphene.[119] Information on molecular orientation and chemistry can be obtained by NEXAFS through the examination of core electron excitation to an unoccupied antibonding state.[85,144–146] Indeed, our collaborators had successfully used experimental NEXAFS to widely explore rippling and interactions at interfaces of single and bilayer graphene growth on Cu by chemical vapor deposition (CVD) and transferred to SiO_2 substrates.[119] However, characterization prone to understanding molecular details at wafer length scales is missing. We have provided evidence of the value of hyperspectral spectroscopy to understand out-of-plane deformations at wafer levels on transferred graphene, as shown in Chapter 3.[147] Furthermore, successfully theoretical and experimental NEXAFS has been used to investigate out-of-plane deformations and doping in CVD-grown graphene on Cu, as well as interface chemical bonding of single layer graphene (SLG) deposited on Cu, Ni and Co substrates has been reported.[112,128,148]

This chapter studies in-plane strain effects on lattice parameter resulting from growth and subsequent transfer to foreign substrates. The studies are conducted through a mixed theoretical/experimental approach to further exploit the wealth of information in experimental hyperspectral imaging when combined with theory and data analytics. In this scheme and with aid of first-principles calculations to yield theoretical standards, average strains and lattice constants of transferred graphene can be predicted. This is done by exploiting the relationship between bond lengths and σ^* shifts in NEXAFS spectroscopy,[a] where a strained bond (i.e., increased lattice parameter) yields a shift to lower σ^* energy positions. To this end, spectra from a total of 6 theoretical samples (each under different levels of strain therefore with different lattice parameters) were calculated and compared with experimental data from samples previously introduced in Chapter 3.

The approach described here presents an alternative—and more comprehensive method—to Raman techniques recently published.[150] Like Raman,[151,152] the present

---

[a]Molecular Orbital calculations had showed that the σ^* positions of atoms where dependent on bond lengths.[149]

approach is suitable to deployment in Cu derived graphene, given the low charge transfer between substrate and epilayer. In advantage to Raman technologies, and owing to the advent of large area hyperspectral detectors,[104,126] this technique is applicable to large substrates at wafer scale, with micro-meter resolution. The combined experimental/theoretical approach featured in this study follows a Materials by Design paradigm and aims at addressing a pending issue in the context of post-CMOS technologies. Lastly, the advantageous of this technique is that it can be deployed at wafer scale and hence, is prone to industrial-level assessment.

4.2 Computational Details

Crystal relaxations of unit cells of 2.47 Å as lattice parameter of single layer graphene (SLG) and graphene on copper substrate along the [111] direction (SLG/Cu) were carried out using plane-wave density functional theory (DFT) implemented in Quantum ESPRESSO within the pseudopotential approximation.[28,153] We employed ultrasoft pseudopotentials, energy cutoffs of 30 Ry for plane wave basis set and 320 Ry for charge density, k-sampling grid in the Monkhorst-Pack scheme of $30 \times 30 \times 1$ and vacuum of ∼15 Å along the Z-axis. Total energy and electronic self-consistency criteria were set to 10^{-6} Ry and 10^{-8} Ry. Atomic forces at equilibrium position were converged below 0.01 eV/Å. All relaxations were modelled under the general-gradient approximation (GGA) with the Perdue-Burke-Ernzerhof (PBE) exchange-correlation functional.[98,99]

Subsequently, self-consistent calculations of SLG and SLG/Cu with 2.42 Å, 2.47 Å and 2.51 Å lattice parameters were performed. SLG was simulated considering a unit cell of 2 C atoms whereas for SLG/Cu the unit cell contains 4 Cu atoms, one per each layer, and 2 C atoms for the SLG part. We have considered the most stable configuration top-fcc.[154,155] Previous work reported 4 atomic layers as the minimum number of layers before physical properties begin to change.[155] Lattice constants of Cu substrates has been adapted to graphene accordingly, as depicted in Figure 4.1.[100,122]

In this work, van der Waals interaction was not considered in the calculations; instead the interface distance (d_z) of 3.25 Å was assumed for all SLG/Cu systems. Such interface distance was accurately calculated by Olsen et. al. under the random phase approximation (RPA) where the interfacial chemical bonding and van der Waals interactions were considered.[124,148] Ground state band structures were

performed by sampling the Brillouin Zone with 200×200×1, where convergence of Fermi energy is achieved within the self-consistent field calculations of 0.01 eV. High symmetry k-points (M and K) were explicitly included.
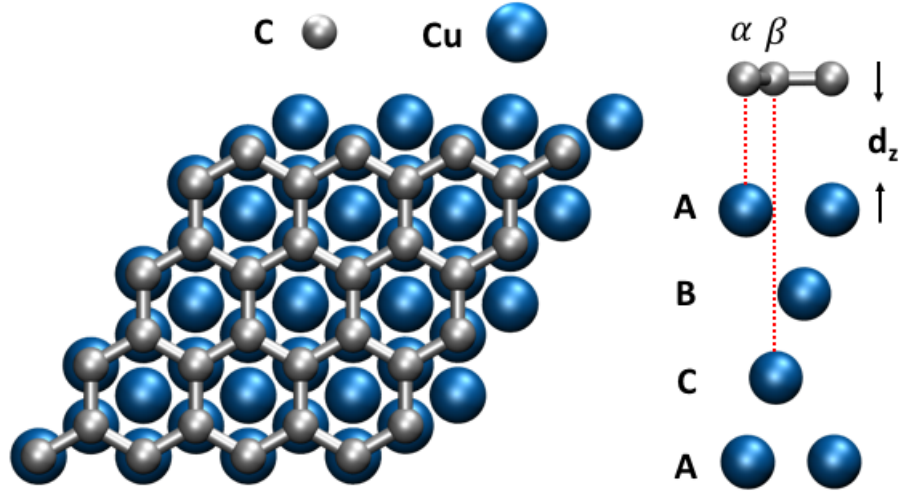
Figure 4.1: Most stable top-fcc atomic configuration of SLG/Cu represented by four atomic layers of Cu where α and β C atoms from SLG unit cell are over Cu atoms in layers A and C. Interface distance d_z of 3.25 Å

A graphene ripple was also relaxed under same criteria of SLG except that k-sampling grid in the Monkhorst-Pack scheme of 10×10×1 and equilibrium atomic force of 0.02 eV/Å were applied. In this scenario, the supercell contained 200 C atoms.

To simulate NEXAFS, supercells assembled by 7 replications of unit cell along X and Y axis has been employed. This supercell's size provides a suitable distance between absorbing atoms to avoid interaction between them due to the periodic boundary conditions. Supercells contain 98 C atoms for each SLG and 294 atoms (98 C and 196 Cu atoms) for SLG/Cu. *Ab initio* calculations of NEXAFS spectra at C K-edge were conducted in the framework of the excited electron and core-hole (XCH) approximation implemented in the Shirley code at 55° of incidence of X-ray beam to enhance $\pi^*_{C=C}$ and σ^*_{C-C} resonances.[86] In order to simulate the excitation of the carbon atom due to the X-ray, one electron from the $1s$ state of the carbon pseudopotential has been removed. One carbon atom from the supercell has been used to calculate the unoccupied states under the pseudopotential approximation

that includes the core-hole interactions. XCH-NEXAFS uses the PBE form for the exchange-correlation potential within GGA approximation.

4.3 Transferred Graphene Layers and Theoretical Graphene Standards

Single and multiple layer stacks on SiC along with epitaxial SLG/SiC (i.e., experimental standard), containing both Si and C- terminated SiC were chosen. Staking of four graphene layers (4LG/SiC) on both surface termination were assembled and examined by NEXAFS spectroscopy. Multiple layer graphene is known to improve overall device performance through conductivity,[156] and it is an additional variable here. The question stacked graphene samples could answer is whether initially nucleated deformations either propagate through the graphene stack or further relax as a function of underlying substrate interactions.

Figure 4.2 shows spectra from all experimental samples. All spectra reveal degree of contamination evidenced by the presence of $\pi^*_{C=C}$ intensities at 285 eV on SiC substrates. Contaminations builds up as a consequence of exposure of SiC substrates to environments out of the cleanroom. Spectra also show expected well-defined resonances in transferred SLG at 285 eV ($\pi^*_{C=C}$), 287 eV (σ^*_{C-H}), 288 eV ($\pi^*_{C=O}$) and 292 eV (σ^*_{C-C}).[b,119] These results suggest that SiC termination also has an effect on NEXAFS spectra of transferred CVD-grown graphene. For instance, the spectrum of SLG/SiC(Si) in Figure 4.2a shows distinctive sharp σ^* resonance of graphene whilst a broad σ^* resonance is observed in SLG/SiC(C) in Figure 4.2b due to the convolution of σ^*_{C-C} and σ^*_{Si-C} signals from the substrate (Figure 4.2b) which suggest that spectra of SLG/SiC(C) is dominated by the substrate. Indeed, experimental and theoretical spectra of SiC (both 3C and 6H polytypes) have been studied previously and show comparable intensities as those shown here, with higher texture in the 287, 288 eV and 292 eV regions for 6H-SiC than for 3C-SiC, as shown in Figure 4.2.[157]

The pronounced graphene distinctive features from SLG/SiC(Si) originated at the Si layer between carbon in the substrate and graphene,[111] which suppresses Auger signal from the substrate. Subsequent transfer of four monolayers have

---

[b]The different properties of graphene grown on Si and C terminations of SiC have been well documented by Norimatsu and Kusunoki.[30]
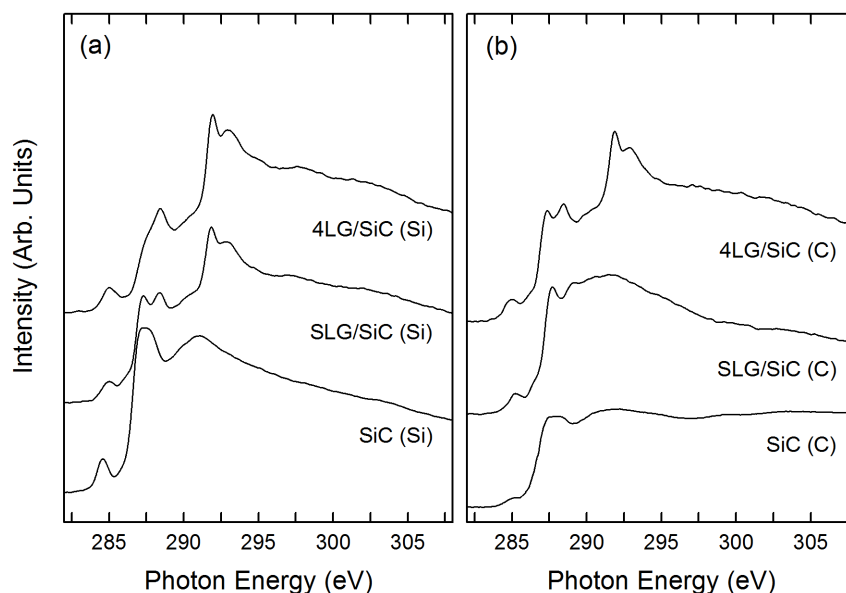
Figure 4.2: Experimental C K-edge NEXAFS spectra of substrate SiC, single-layer graphene and four graphene layers transferred onto SiC. (a) Si-terminated substrate. (b) C-terminated substrate. Transfer onto C-terminated substrates gives different spectra with single-layer graphene and differences are observed upon transfer of four graphene layers in the region associated with oxygenated contributions.

little impact in the NEXAFS spectra as a function of substrate termination, other than increased intensities of oxygenated states. Also, decreased intensities at 287 eV in 4LG/SiC(Si) suggests that C-H impurities could be mostly in the substrate. Conversely, $\pi^*_{C=O}$ signal ~288 eV has a reduced intensity in the substrate and increases with graphene in both terminations, suggesting carboxylic impurities are being generated on the graphitic structure throughout chemical processing.[158]

Rippling can be observed across the wafer at a microscopic scale through a variety of techniques. He Ion Microscopy is an innovative microscopy modality that has been used to describe the extent of large superficial mechanical deformations.[159] It is well known that He-IM imaging of soft matter systems reproduce topographic features with high fidelity, which indicates the observed corrugation was not originated by electron beam heating.[160] Figure 4.3 reveals extensive regions of high corrugation with features up to 50 nm wide combined with flat zones (even on the freestanding domains) of CVD-grown graphene on Cu transferred to
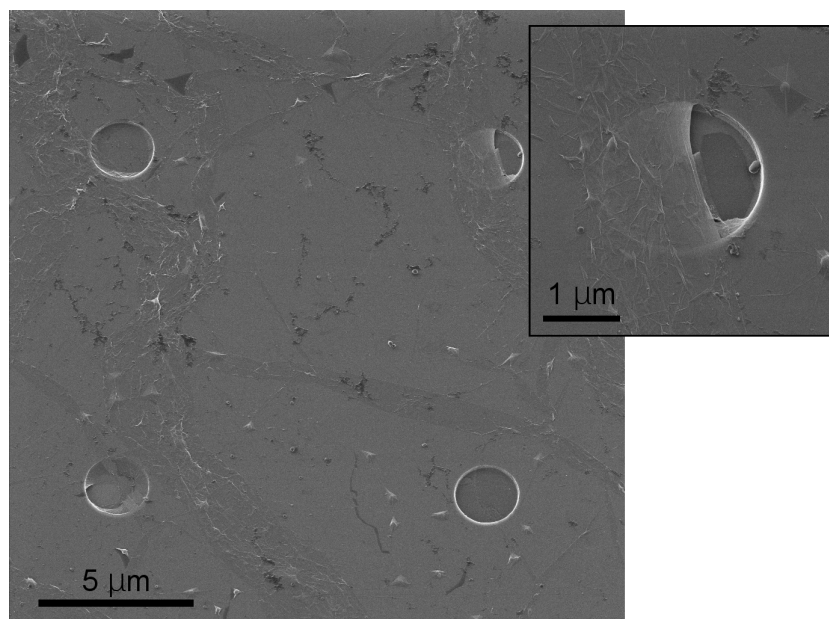
Figure 4.3: He Ion Microscopy (He-IM) of CVD-grown graphene grown on Cu and later transferred to a SiN TEM grid. This technique conveniently emphasizes characteristic ripples of ~50 nm width that are visible throughout the sample.

a SiN TEM grid. In this micrograph the scan width is 15×15 mm^2, while scanned zones at NEXAFS experiment ranged between 22 and 53 mm^2. Furthermore, absence of coating layers to prevent charging effects further guarantee high fidelity of graphene rippling effects caused by growth and transfer to any substrate, although with widths and heights variations. Indeed, widths from tens to hundreds of nanometers, as well as, heights of up to 6 nm have been recorded by AFM upon transfer.[136] Conversely to out-of-plane features, morphological description of in-plane deformations (also as results from growth and processing) requires of high resolution TEM or STM approaches that will nevertheless only provide a very local description.[111]

To address such sensitivity versus length scale cunundrum, this work propose an innovative methodology. Here, experimental NEXAFS (as described above) is combined with simulated spectra to examine structural deformation. Changes in lattice constant result from structural deformations from growth and processing. Therefore, three computed standards of free-standing graphene of lattice parameters (2.42 Å,[112] 2.47 Å[148] and 2.51 Å) have been computed following the procedure described in Section 4.2 (Computational Details). In addition, calculation of

76
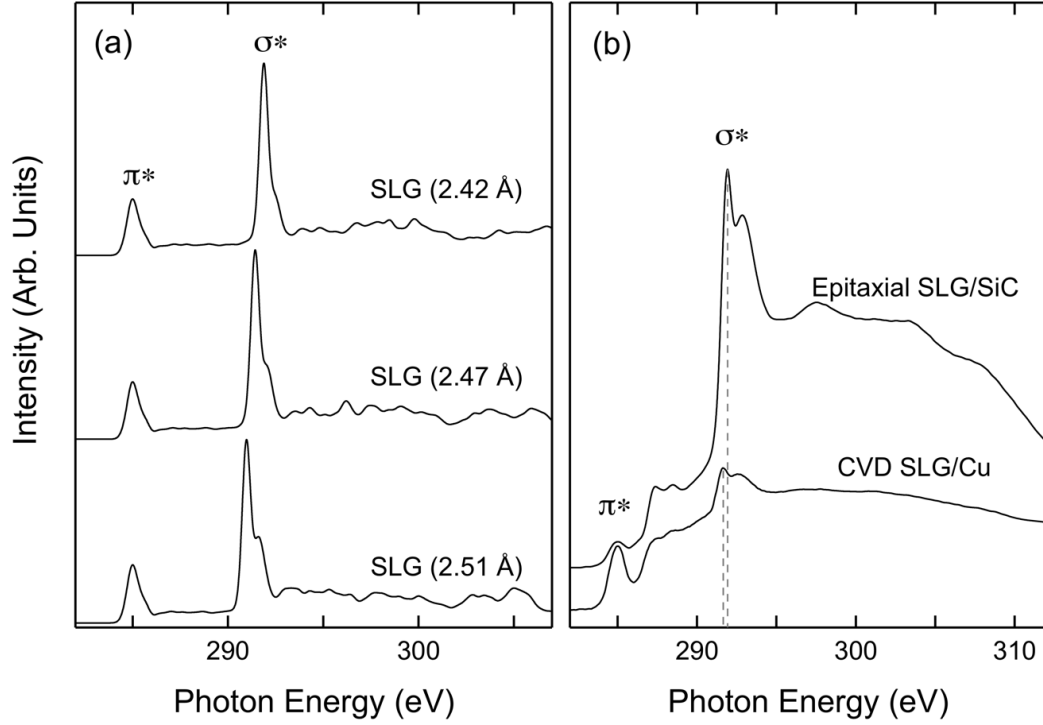
Figure 4.4: (a) Calculated C K-edge NEXAFS spectra of SLG. Position of σ^* resonance is a function of graphene lattice parameter, or bond length. (b) Experimental C K-edge NEXAFS of epitaxially grown graphene on SiC and CVD-grown graphene on copper result in different C-C bond lengths, evidenced by different σ^* resonance energy positions.

graphene grown on Cu (SLG/Cu) was needed to study charge transfer mechanisms through substrate effects. Resulting NEXAFS spectra of theoretical and experimental standards (i.e., epitaxially grown SLG on SiC and CVD-grown SLG on Cu) are shown in Figures 4.4(a and b). Spectra feature distinctive 1s $\rightarrow \pi^*_{C=C}$ and 1s $\rightarrow \sigma^*_{C-C}$ electronic transitions at around 285 and 291 eV respectively (Figures 4.4a and b).[112,119] Also, it is observed resonances at energies between 287 and 288 eV on the experimental spectra that correspond to σ^*_{C-H} and $\pi^*_{C=O}$ impurity states as previously identified in Figure 4.2. It is worth mentioning that both experimental and theoretical NEXAFS spectra have shown surface termination-sensitivity on SiC.[157] Also, polarization and detector bias variations have been used to describe

77

graphene-susbtrate interactions.[111]

The core excitonic nature at $\sim$292 eV of the associated sp^2 graphite has been demonstrated as both theoretically and experimentally.[161,162] Indeed, recent studies have confirmed graphene σ^*_{C-C} state to be core exciton.[163] Density functional theory calculations performed in this work (under the assumption of fully uniform strain with retention of conjugation), suggest empirical correlations exist between energy position of σ^* resonances and graphene bond lengths. Although the limits of this correlation have not been studied yet, the computed empirical correlations described here provide a methodology for evaluating strain effects that might be induced by underlying substrates. Computational details proving this correlation are discussed in more details in the upcoming sections.

4.4 Substrate Effects

It is known that both charge transfer and screening effects as well as screening effects have impact on spectral features in Raman[151,152] and NEXAFS spectroscopy.[148] To clarify the origin of the observed shifts, substrate effects from screening as well as charge transfer to graphene NEXAFS spectra have been simulated. In cu substrates, small σ^* shift from the graphene epilayer are noticeable from the experimental samples in Figure 4.4. And in fact, shift in σ^* resonances can be a direct consequence of in-plane strained graphene as shown in theoretical standards (see Figure 4.4a), since hybridization with the $\pi^*_{C=C}$ resonances in the graphitic lattice is not possible.

Similarly, adjacent atoms in the out-of-plane deformation (like those along the ripple) will present shifted σ^* resonances as indicative of lattice constant variation. The density functional theory calculations thus provide a practical measure of strain within the samples, which are likely a result of the highly excitonic nature of σ^* resonances. In this section, aspects of strain, charge transfer and substrate screening phenomena that influence the NEXAFS features[85,148] are discussed. The purpose of this discussion is to seek a functional correlation between σ^* and strains for graphene grown on Cu and on SiC, as well as transferred SLG onto SiC.

4.4.1 Charge Transfer Effects in Growth Substrates

For the purpose of quantifying the amount of charge transferred between Cu and SLG in a SLG/Cu sytems, calculations were carried out through the Bader[164] and Löwdin[165] approaches.[c] It is worth mentioning that contradictory behavior has been observed on the computed charge transfer with those methods for the SLG/Cu structures. Indeed, the Löwdin (atom-centered) approach predicted transfer from graphene to Cu, while Bader's approach predicted the inverse transfer. Even though, Bader's method captured the correct flow of charge from Cu to graphene; it failed to predict increased charge transfer with increasing lattice parameter. Hence, direct quantification of transferred charge has not been possible to achieve so far. Here, an accurate indirect analysis based on DFT band structure calculations has been employed to successfully confirm charge transfer processes by monitoring shifts of the Fermi energy level on the corresponding electronic band structure. In this scenario, the Dirac cone of freestanding graphene, which nominally coincides with the Fermi energy, is shifted to lower energies in the presence Cu substrate. This shift reflects electrons from the Cu substrate rearranging to populate previously unoccupied states in graphene, as pictured in Figure 4.5a.[166,167]

Band structures of freestanding graphene and SLG/Cu constrained under three levels of strain are shown in Figure 4.5b. These theoretical standards will be key to elucidate strain effects on charge transfer. Shifts of Fermi energy to higher energies in the calculated SLG/Cu band structures indicate charge transfer from Cu substrates to graphene.

Notably, up-shifts also show an increment of Fermi energy shifts as strain (lattice parameter) increases. Indeed, computed Dirac point energies (E_D) shift with respect to Fermi energy (E_F) yielded values of 0.05 eV, 0.21 eV, and 0.33 eV for lattice parameters of 2.42, 2.47, and 2.51 Å, respectively. The choice of lattice parameters was based in the experimental range found in the literature. Typically, experimental E_Ds with respect to E_Fs are measured through angle resolved photoemission spectroscopy measurement (ARPES). The experimental measurements revealed values of 0.38 eV,[167] 0.3 eV,[168] and 0.37eV,[169] the latter for graphene with lattice parameter of 2.46 Å, as measured by LEED.[169]

---

[c]In Bader analysis the system ground state electron density is used to compute each individual atomic electron charge, making its efficiency dependent on the splitting of the system electron density in the real space.[164] On the other hand, Löwdin population analysis projects atomic wave functions into orthonormal basis set functions, prior to the population analysis.[165]
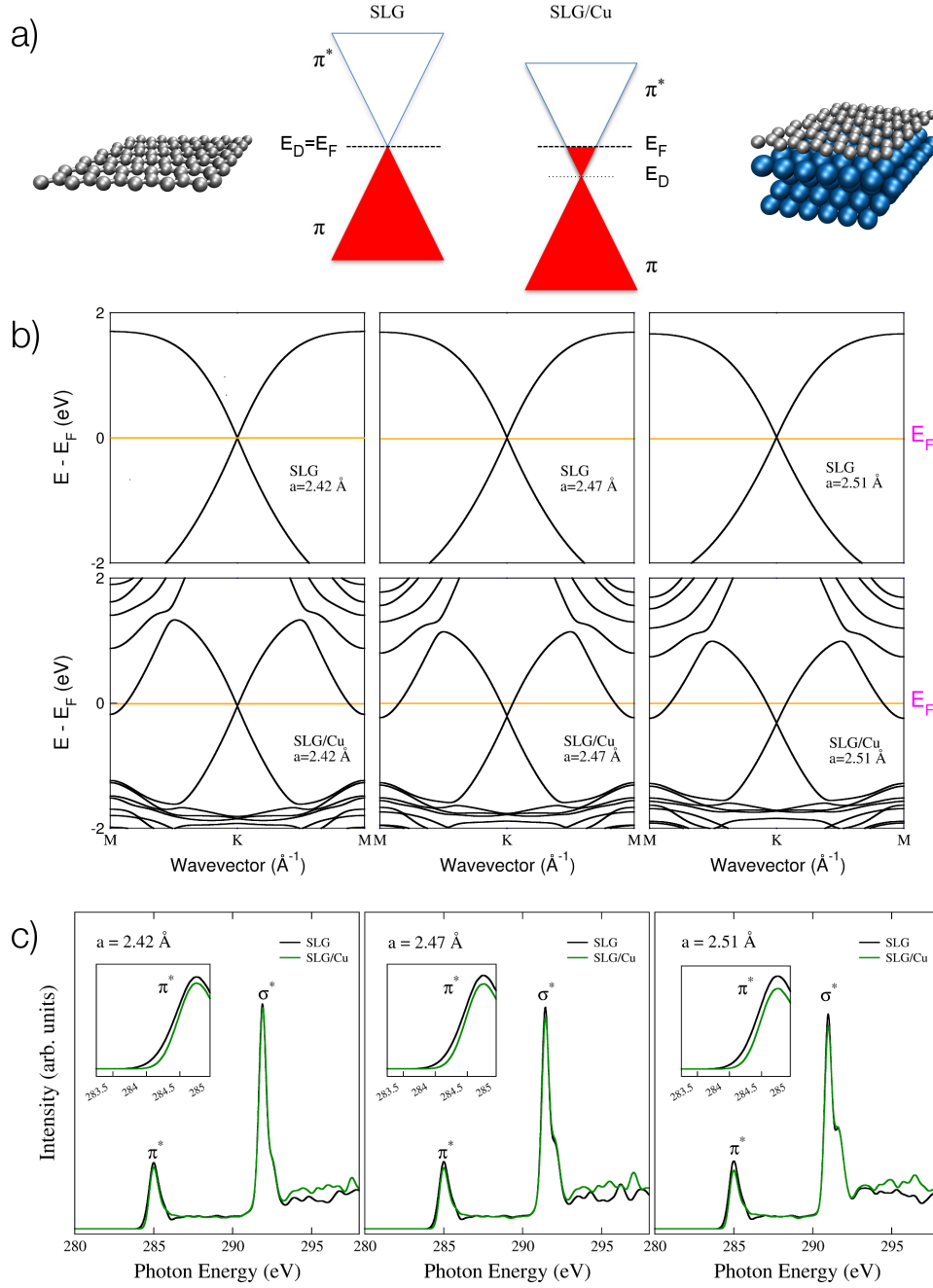
Figure 4.5: Charge transfer process between graphene and Cu substrate. (a) n-doping graphene caused by metal substrate. (b) Band structures of SLG and SLG/Cu as function of the lattice parameter. (c) Charge transfer evidenced in NEXAFS spectra of SLG and SLG/Cu at π^* resonance.

In Figure 4.5c, shifts in Fermi energies are seen in NEXAFS spectra of SLG and SLG/Cu systems for the three lattice parameters. This shift is a consequence of charge transfer from Cu surface to graphene. Such charge transfer induces a shift to higher energies in the rising edge of π^* resonances, as observed in Figure 4.5c. Indeed, an increased curvature on the rising slope of π^* can be seen in more detail in the corresponding insets in Figure 4.5c; which is also consistent with decreased Dirac points with respect to the Fermi energy (Figure 4.5b). This finding suggests that larger lattice strains will be required to yield increased for π^* resonances. Simulated NEXAFS spectra also showed additional shifts in the σ^* energy positions which decrease when lattice constants increase. Therefore, charge transfer clearly stands up as a likely feature that affects the σ^* energy position. For these particular systems however, those shifts are significantly small (in the order of 0.01 eV) which are not easily observed on simulations (Figure 4.5c), and also below the current energy resolution in the spectrometer. Consequently, σ^* energy position shifts owing to charge transfer are not crucial in the predicted bond lengths of SLG/Cu at this time.

It is worth highlighting that theoretical analysis of band structures, and specially of NEXAFS spectra of SLG/SiC systems, have not been performed in this work because of the high computational cost. Nevertheless, values of the order of 0.42 eV of Dirac point energy on epitaxial graphene grown on 6H-SiC(0001) measured by ARPES have been reported.[170] Such values fall within the range of experimental and theoretical shifts from SLG/Cu. The theoretical shifts are correlated with minimum shifts in σ^* energy positions in simulated NEXAFS spectra. These findings suggest no significant impact of charge transfer in the σ^* energy position of SLG/SiC systems. As a result, σ^* energy position shifts in SLG/SiC could be ascribed to lattice parameter variations, and perhaps to substrate shielding effects, but not to charge transfer.

4.4.2   Substrate Shielding and Lattice Constant Effects

Electrostatic screening has been reported to yield NEXAFS spectral shifts. In fact, some authors had observed overall spectral hard shifts to lower energies by about 1 eV from SLG/Cu when compared to theoretical SLG.[148] Screening shows as hard shift in the band structure relative to the Fermi level, that compensates for charge asymmetry in SLG/Cu. Indeed, the large interface distance between graphene and Cu of 3.25 Å provides too high Coulombic barrier for efficient charge transfer.[148] As a result, the system engages in charge redistribution, or dipolar rearrangement, as described by Zhan.[138]

In this work, rigid shifts of the NEXAFS spectra from the simulated SLG/Cu systems on 2.42, 2.47, and 2.51 Å are also observed, as shown in Figure 4.6. Here, smaller lattice parameters produce spectral shifts to lower energies in larger intervals, although without charge transfer entailed due to variation of the lattice parameter; instead it is a second order response of the system in a new electrostatic field, leading to charge rearrangement.

Consequently, It is necessary to address three effects on the spectral features, i.e., effects induced by electrostatic screening (Figure 4.6a), effects due to transferring of charge and lattice parameter variation (Figure 4.6b). With respect to the first effect, where a hard shift on the entire spectra is produced by the Cu substrate shielding, it is considered by monitoring $E(\sigma^*)$ - $E(\pi^*)$ when bond lengths are predicted. As previously discussed, regardless the small charge transfer involved in epitaxial SLG/SiC, it is however uncertain how screening from SiC impacts NEXAFS spectra (It would be addressed further below).

In the case of charge transfer and lattice parameter effects, we have shown in the last section that charge transfer can also affect σ^* energy positions, therefore, potentially distort the prediction of lattice parameters. Although, relative shifts of σ^* resonances due to charge transfer are negligible in this study. Shifts in Figure 4.6b are attributed to solely lattice constant effects. Finally, bond lengths (or lattice constant in crystals) effects give a specific σ^* energy position in agreement with quantum mechanical calculations.[149] Hence, smaller lattice parameter returns higher σ^* energy position, consistent with our results (Figure 4.6b).
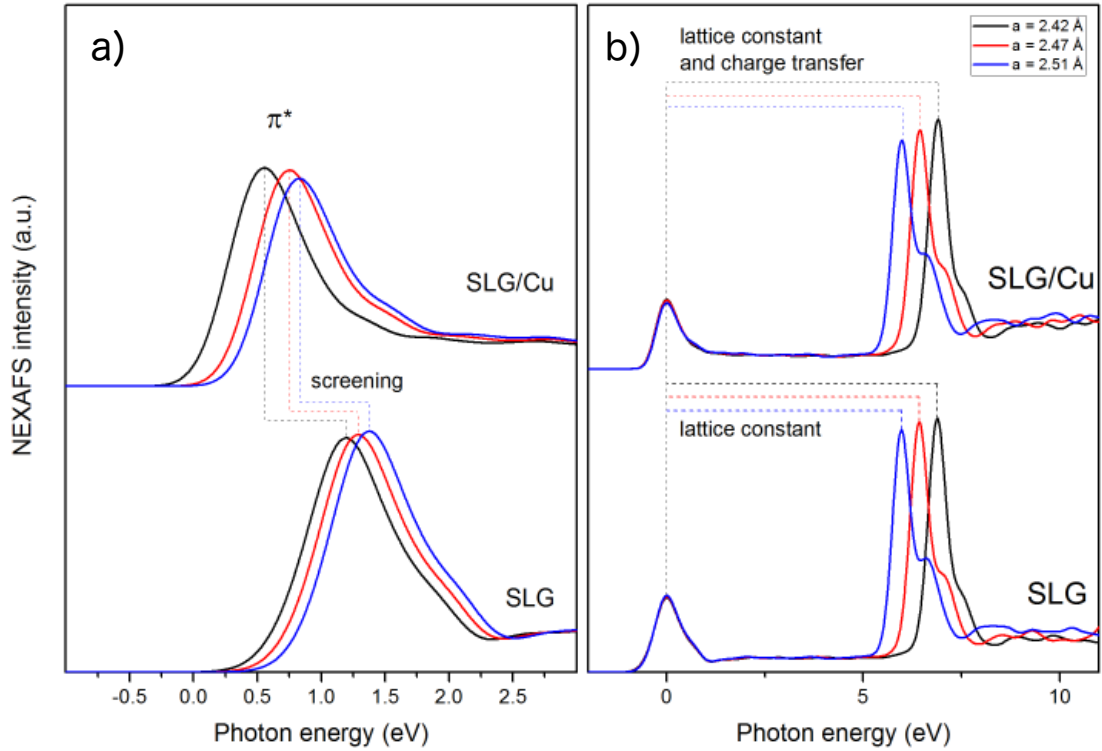
Figure 4.6: Three factors affecting energy position of σ^* resonances. (a) Substrate screening, charge transfer, and lattice constant. (b) To isolate the effect of bond length on the σ^* energy, we will use the π^* energy as reference.

4.5   Lattice Constant Analysis

Experimental NEXAFS spectra of epitaxial SLG/SiC and CVD SLG/Cu certainly exhibit a shift of σ^* resonances from one sample with respect to the other. As seen in Figure 4.4b, these σ^* resonances are placed at energies of 291.8 and 291.3 eV respectively, which suggests to CVD SLG/Cu as the sample with the smallest lattice constant contrasted with SLG/SiC. Additionally, scans on transferred SLG onto SiC substrates produced σ^* features at energies of 291.8 eV for SLG/SiC(Si), and 291.9 eV for both 4LG/SiC(Si) and 4LG/SiC(C) systems. Contrary to differences in growth method, nature of substrate and processing of experimental samples studied in this work, the only variable on the simulated spectra is the bond length, yet spectra still generated σ^* shifts with varying bond lengths. As discussed in the previous section, differences in C-C bond lengths (as reflected in experimental NEXAFS) can be attributed to effects induced by growth, substrate, and processing.

83

By considering E(σ^*) - E(π^*) instead of absolute σ^* energies during the prediction of bond lengths for Cu-derived samples, substrate-related screening effects discussed in the prior section can be omitted. For this reason, and given that charge transfer is below the experimental resolution all σ^* energy positions from Cu-derived graphene, the energy shift positions discussed here reflect lattice parameter variations exclusively. For completion, a discussion on epitaxial SLG/SiC is also tentatively included in this study.

Graphene with different lattice constants were used as theoretical standards derived from density functional theory calculations to fit a linear correlation between resonance energies E(σ^*) - E(π^*) and bond length R as the equation:

$$E(\sigma^*) - E(\pi^*) = aR + b \qquad (4.1)$$

Theoretical standards (SLG and SLG/Cu) were calculated with lattice constants 2.42, 2.47, and 2.51 Å, with the underlying assumption of uniform strain. This assumption is consistent with reported first-principles analysis of characteristic band structure in strained graphene. DFT calculations show the lost of distinctive graphene band structures for lattice constants greater than 3.209 Å.[171] These findings justify the choice of lattice parameters of our theoretical standards; whose band structures (both SLG and SLG/Cu) preserve the expected graphitic components. Indeed, we have taken as experimental reference the reported lattice constant of 2.46 Å of CVD SLG/Cu, which is close to the typically graphite lattice constant of 2.461 Å.[169,171]

In order to exclusively measure σ^* shifts, regardless substrate effects, E(σ^*) - E(π^*) was used to predict bond lengths of experimental samples, following Equation 4.1. Results are shown in Figure 4.7. Interestingly, plots of E(σ^*) - E(π^*) against bond lengths from theoretical standards associated to SLG (black fit line) and to SLG/Cu (red fit line) as shown in Figure 4.7, reveal a slight difference in fitting parameters for both linear fits. Furthermore, charge transfer effects had a subtle effect on σ^* energy positions, as shown in Figure 4.5c. The associated shifts were on the order of 0.01 eV; much below the energy resolution limit of the energy scan in the present setup. For consistency, we have used the regression of SLG/Cu to
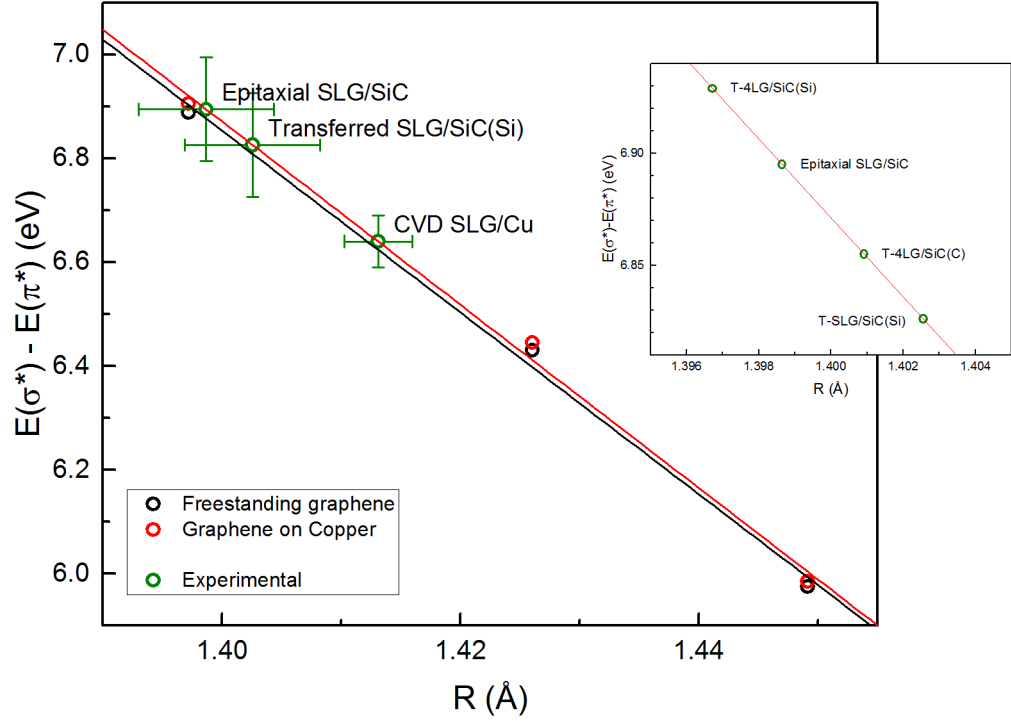
Figure 4.7: C-C bond lengths (R) for the various graphene systems display the predicted linear correlation with the σ^* resonance energy position. The deduced values of R are represented by green circles The inset shows the same regression magnified in the 6.80–6.95 eV and 1.3905–1.404 Å where data from transferred and epitaxial graphene lie.

predict bond lengths of all experimental, grown and transferred samples; for which the only known information through experimental NEXAFS is $E(\sigma^*)$ - $E(\pi^*)$.

Fitting parameters generated after fits the linear equation 4.1 are a = -17.5 and b = 31.6 for freestanding graphene, and a= -17.6 and b= 31.6 for SLG/Cu. In both samples (SLG and SLG/Cu) the correlation coefficients are close to unity, which is an acceptable empirical descriptor of the correlation between R and σ^* energy position. In addition, data points represented by black (for SLG) and red (SLG/Cu) circles are theory-derived to produce a linear fit where experimental σ^* energy were used to estimate values of R. Those deduced values of R are represented by green circles. Inset illustrates the same regression augmented in the energy interval 6.80–

6.95 eV and R interval 1.3905–1.404 Å in which data from transferred and epitaxial graphene lie.

Table 4.1: Predicted C-C bond lengths for all studied graphene systems[a].

System	$E(\sigma^*) - E(\pi^*)(eV)$	$R(\text{Å})$	Predicted $R(\text{Å})$	Strain(%)
SLG (2.46 Å)[b]	—	1.42	—	—
SLG (2.42 Å)[c]	6.888	1.397	—	-1.62
SLG (2.47 Å)[c]	6.430	1.426	—	0.42
SLG (2.51 Å)[c]	5.975	1.449	—	2.04
SLG/Cu (2.42 Å)[d]	6.906	1.397	—	-1.62
SLG/Cu (2.47 Å)[d]	6.446	1.426	—	0.42
SLG/Cu (2.51 Å)[d]	5.985	1.449	—	2.04
CVD SLG/Cu	6.64 ± 0.05	—	1.413 ± 0.003	-0.49
T-SLG/SiC(Si)	6.8 ±0.1	—	1.403 ± 0.006	-1.17
T-4SLG/SiC(Si)	6.9 ± 0.1	—	1.398 ± 0.006	-1.57
T-4SLG/SiC(C)	6.8 ± 0.1	—	1.403 ± 0.006	-1.17
epitaxial SLG/SiC	6.9 ± 0.1	—	1.398 ± 0.006	-1.57

[a]**R** correspond to values of bond length of the standards, which are free standing graphene and graphene on Cu. These are theoretical samples, and **R** is the bond length value by design on free standing graphene and the value of bond length for Graphene on Cu at the interface distance reported by Olsen *et al.*[172] **Predicted R** are values of bond lengths that have been estimated over experimental samples with the assistance of theoretical standards, where a correlation between bond length and σ^* resonance energy was established.
[b]Avila *et al.*[169]
[c]Calculated NEXAFS spectra where the graphene lattice constant is given in parentheses.
[d]Spectra used to fit equation 4.1.

Predictions shown in Figure 4.7 were derived from linear regression analysis applied over the simulated SLG/Cu. In fact, Figure 4.7 shows the bond length predictions of CVD SLG/Cu and of epitaxially-grown SLG/SiC (Figure 4.4). The experimental error for predicted bond lengths was calculated as the energy resolution (0.05 and 0.1 eV for U12 and U7 respectively) divided by fitting parameter a in Equation 4.1.

In the past section we have established a very small impact of charge transfer on the σ^* energy positions of graphene grown on SiC. However, we should clarify that those SLG transferred to SiC substrates will likely experiment van der Waals interaction with the underlying SiC substrates. In fact, it is expected weak van der

Waals forces since transferring is executed at much lower temperatures than those temperatures usually involved in growth, resulting in no charge exchange or any other substrate artifact. Therefore, generating no spectral signature and justifying bond length predictions in graphene transferred to SiC.

Altogether, bond lengths of CVD SLG/Cu, Epitaxial SLG/SiC and transferred SLG to SiC on both terminations have been predicted by means of regressions (Figure 4.7 and Table 4.1). In addition, strains have been calculated with respect to CVD-grown graphene, which is taken from the literature as an experimental standard with lattice constant 2.46 Å (or its associated bond length 1.42 Å). This value has been derived from low energy electron diffraction measurements on CVD-grown graphene on Cu substrate, as reported by Avila *et al.*.[169]

Clearly, growth substrates have impact on the C-C bond length as shown in Figure 4.4b. Hence, we have used epitaxial SLG/SiC and SLG/Cu as experimental references to which SLG transferred to SiC substrates are compared. Bond lengths predictions of all experimental samples, reported in Table 4.1, were found to be lower than the cited 1.42 Å by less than 2%.[144] As a matter of fact, Gui *et al.* showed that under strains less than 2% graphene is isotropic, namely, the Poisson ratios in the two directions are equal (deformation along X and Y axis take same values).[171] Also, under even smaller strain (less than 1.5%), the Poisson ratios were constant (0.1732).

According to the discussion, predicted values in Table 4.1 (less than 2%) suggest that transferred SLG are under isotropic and compressive strain, consistent with experimental results found in the literature. Indeed, it shows a strain of -1.57% for the Epitaxial SLG/SiC which is overestimated since the typical maximum strain would be on the order of 1%.[111,173] Even when only three modeled graphene structures were employed to calibrate the line used to predict bond lengths of the experimental samples.

4.6 Interpretation of Strain and Lattice Constant Correlation with σ^* Shifts

Until now, the contribution to strain variation of individual morphologies across the scanned regions are unknown, along with, the dynamics of how their spectroscopic signatures are combined to produce a certain σ^* position which produces a

certain amount of strain have not yet been discussed. Moreover, it is worth mentioning that in free-standing graphene (or equivalently graphene in transferred systems where substrate effects are absent), computed SLG with lattice constant of 2.42 Å is compressed by little less than 3% with respect the theoretical standard lattice constant of 2.47 Å, and even under such large strain, intrinsic electronic and structural properties of graphene remain as seen in the band structures of Figure 4.5b.

One should bear in mind, however, that in the simulated systems discussed here, every bond is isotropically strained (molecularly homogeneous) whereas in experimental samples, spectra are averaged over local anisotropic inhomogeneities, including for instance, localized strain and/or rippling, as seen in Figure 4.3.

With the aim of investigating a rippled morphology at the atomic scale, we have modeled a rippled region, showing strain bonds throughout, such the one depicted in Figure 4.8a, and calculated NEXAFS spectra of associated atoms along the ripple (blue atoms in Figure 4.8a). Spectra plotted in Figure 4.8b reveals energy shifts in the σ^* resonances associated with individual strained bond lengths of the blue atoms in the ripple. The single strain value predicted for an experimental system is due to strain homogeneities overall the scanned region. The changes in energy of σ^* resonances from atoms 1 to 10 demonstrate how sensitive this method is to capture variations at the atomic scale that will be then averaged. Indeed, we have verified that the average spectra along the rippled region gives a σ^* energy position that is the resulting average of the individual shifts from each atom along the ripple. Such results suggest that every morphology is going to contribute to the measured integrated σ^* feature, which allows the identification of an asymmetrically distorted real system with a certain value of strain to an equivalent evenly strained system. Both would actually provide equal integrated spectra.

Also, we should point out that σ^* shifts capture both in-plane and out-of-plane strain, although, high curvature in large corrugations might not be accounted due to transition prohibition or due to the orthogonality between beam polarization and vector associated with the σ^* orbitals.[85] Nevertheless, majority of morphologies will be registered by this method.

We emphasize the ability of the proposed technique to gives a clear description of the value of averaged spectra over extensive areas including wafer size regions, where molecular details of single atoms are conserved and averaged out together with the collective. Even more, specific capabilities of these NEXAFS spectra are
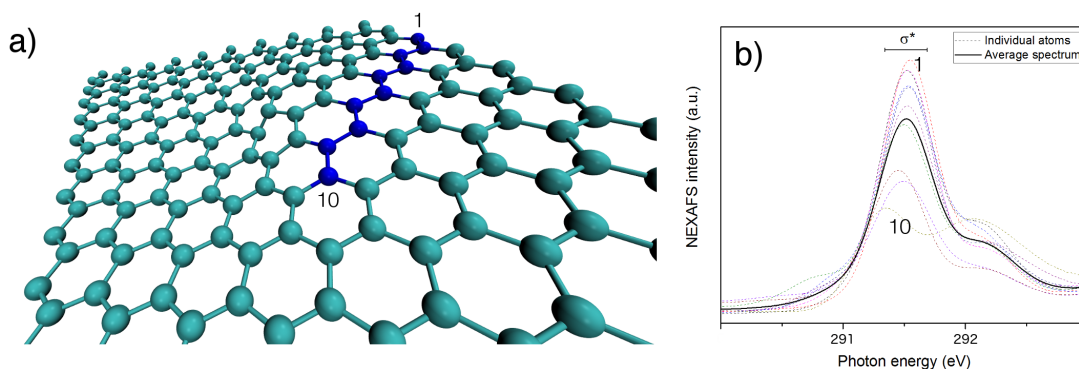
Figure 4.8: Theoretical NEXAFS calculations for atoms along a graphene ripple. Individual atoms produce σ^* resonances at various energies, indicating different bond lengths.

further accentuated with the advent of large area hyperspectral NEXAFS technique. In fact, the analysis made here can be expanded to specific areas of interest (not only the entire wafer) thank to the dynamic range resolution between 40 μm to the tens of mms, thereby opening the possibility of in-depth strain metrics.

It is worth to highlight that given the interest on the increased transport properties as a result of stacked configurations onto multiple transfers[156] (mentioned in section 4.3). This technique enables the characterization of both at micron and wafer scales of transferred graphene to substrates of technological relevance, beyond commonly growth substrates. On transfer of single layer graphene to SiC(Si), the bond length of decreases to 1.403 Å with respect to bond length of CVD SLG/Cu (1.413 Å). Subsequent transfers of layers show similar decrease of the bond length. However, before providing an interpretation of particularities behind transferred systems, a comparative analysis on the experimental standards CVD SLG/Cu and epitaxial SLG/SiC is required.

Bertran *et al.* verified how fine control over experimental variables such as H_2 flow could have significant impact over strain on CVD SLG/Cu.[174] In fact, compressive strain could be reduced from 0.2% to 0.026% by measuring Raman shifts of the 2D phonon mode compared to that of unstrained pristine graphene. In addition, combination of Raman spectroscopy with molecular dynamics simulations give an average compressive strain of 0.5% for CVD SLG/Cu, which is the resulting average of local C-C bond lengths being deformed in the range 0.009–0.005 Å, yielding strains between 0.3–0.6%.[175] This suggests that predicted strain in CVD

SLG/Cu (-0.49%) reported in Table 4.1 falls within the expected range.

Unfortunately, analysis of the standard epitaxial SLG/SiC is less straightforward. Even though, in recent review of epitaxially grown graphene, biaxial strain first arises from epitaxial stress during growth of graphene on a substrate, but is energetically expensive.[111] Indeed, strain above 1% has been identified as prohibitive, since it cannot even be done in graphene-metal systems. In this study, prediction of strain in epitaxial SLG/SiC is compressive by 1.57%, unconsistent with Tetlow's parameters. Besides computation of band structure and specially NEXAFS spectrum of epitaxial SLG/SiC is highly costly in terms of computational resources. However, Coletti *et al.* have measured the Dirac point energy of epitaxial SLG/SiC sample to be around 0.42 eV, comparable to that observed in SLG/Cu, which produced little impact on the σ^* shift,[176] leading to the conclusion that charge transfer in epitaxial SLG/SiC would not result in shifting of σ^* resonance. Therefore, before to conclude that this technique of σ^* resonance shifts is applicable to epitaxial SLG/SiC, the substrate effects on epitaxial SLG/SiC need to be elucidated. On the other hand, substrate effects had promoted a hard shift in CVD SLG/Cu systems, and the effects in SiC systems had not been derived. An unexpectedly large predicted strain (more than 1%) was found for epitaxial SLG/SiC was found unexpected, indicating that complexity of SiC substrate effects might be higher than a spectral hard shift.

In addition, evidence of structural strain in epitaxial graphene on 6H-SiC(0001) derived from long annealing times has been reported by Ferralis *et al.*, who indeed estimated a compressive residual strain of $\sim 0.8\%$ at room temperature. Such residual strain results from the large difference in the thermal expansion coefficients of graphene and SiC substrate, and adjustable by growth times, between the theoretical maximum of $\sim 0.8\%$ and the empirical minimum value of 0.1%.[173] Another estimation of residual compressive strain of 0.2% in epitaxial graphene on SiC(0001) was reported by Schuman *et al.*[176]

When these strain values are compared to our predicted strain of -1.57% for epitaxial SLG/SiC, clearly our method yields an overestimated strain. This result suggest that details of screening effects due to SiC growth substrate need to be considered. To support further applicability of the calibrated trend in Figure 4.6, we predicted strains from NEXAFS Carbon K-edge spectra of epitaxial SLG/SiC(Si)

found in literature (0.46%,[177] 0.67%,[178] and 1.07%.[179]) with equation 4.1. Such predictions imply tensile strain in graphene, which contradicts the widely accepted lattice parameter dynamics of epitaxial SLG/SiC to be indeed a compressed epilayer. Hence, this methodology cannot be applied to epitaxial SLG/SiC unless substrate effects (screening effects) are rationalized.

It is important to remember that transferred graphene and subjacent SiC interact weakly through van der Waals dispersion forces, consequently, neither charge transfer nor substrate shielding need to be accounted for. Notwithstanding that predicted strains for the transferred cases are in excess of the 1% limit given by Tetlow,[127] these systems will be highly rippled but with absence of substrate related effects. It partially justifies the larger values predicted (still under 2% compression, but conserving native graphene structure as shown in Figure 4.5b). Moreover, Table 4.1 shows that transferred systems show larger compressive strain than CVD SLG/Cu, as well as this increment could increase with subsequent transferred layers. In fact, the strain in CVD SLG/Cu expands from the initial -0.49% to -1.17% for T-SLG/SiC(Si) and -1.57% for T- 4SLG/SiC(Si). Additionally, the strain for T-4SLG/SiC(C) and T-SLG/SiC(Si) are equal to -1.17%. According to these results, it seems that transferred systems experienced an increase in frequency and magnitude of rippling events, which is expected and needs to be supervised by the σ^* shift method proposed here. Another point that emerges from these results is that transferring multiple epilayers could influence the level of generated compressive stress. Also, he dependence on substrate termination is not clear this time.

Finally, it is possible to apply this σ^* shift methodology to each segmented region since microscopy-hyperspectral acquisition mode has the ability to scan small regions in every sample. This will provide information of strain variations at wafer level in addition to strain values for those smaller regions. Here, we have only analyzed integrated regions of 5×3 mm^2. But nevertheless, this technology is able to scan regions as large as 20×20 mm^2 with a resolution under 10 μm. As a consequence, the advent of hyperspectral synchrotron spectroscopy paves the way to spatially resolved mechanical deformation at the micron level and wafer scale capable to maintain molecular sensitivity, thus, overcoming detectability limits. Furthermore, optimal results could be achieved by setting the detector at the highest energy resolution during the spectral acquisition along with application of machine learning models at different length scales to completely exploit the collected data

to inform structural deformation upon growth and processing at industrial level. We should mention that here, data was collected at 0.2 eV resolution, instead of the maximum 0.06 eV that would give higher sensitivity in the predicted lattice parameters. For this implementation to come to full term, newly developed hyperspectral NEXAFS detectors need to become forefront technology, accessible in various beamlines. This availability will promote extensive use and exploitation of the technological advancements that this detector represents.

Fundamentally, this work demonstrates that interactions at substrate interfaces can induce measurable changes in the σ^* peak positions of NEXAFS spectra. When calibrated with density functional theory calculations, this work provides a tool for mapping strain across transferred graphene. Another important point to highlight - and that has been demonstrated here- is the ability of the σ^* shift technique to reflect out-of-plane strain effects. This finding is crucial to account for the ripple-derived strain effects that are known to develop throughout the entire wafer.

4.7 Summary

In this chapter a technique is proposed to measure graphene strains at wafer level. This techniques relies on a robust correlation underwritten by first-principles simulations which highlight the excitonic character of σ^* and π^* features. This method is directly applicable to CVD-grown graphene on Cu as well as to graphene layers previously transferred to substrates with established weak van der Waals dispersion forces. It is possible to apply this technique to SiC-derived graphene, as long as, the specifics of substrate interactions are elucidated and accounted for. Additionally, this method is applicable to other transition metal substrates, however, measurements of both charge transfer between graphene and substrate (known to be more prominent than in Cu), as well as substrate screening, are needed to isolate the σ^* energy dependence on bond length and strain. The validity of the σ^* energy shift correlation with strain lies in the excitonic nature of this resonance. In this scheme, a localized absorbing electron which leads to a core electron decay, which is likely the reason for the observed calculations. Finally, the proposed method here, holds promise in other 2D materials; probing the bond length directly by measuring an ubiquitous σ^* signal and taking into account specific substrate/epilayer relations. To fully implement this approach, further work is required to analyze the correlation between functionalization and dimensional reduction.

Building a Fingerprints Database of Topological Defects on Single Layer Graphene by NEXAFS Spectroscopy

5.1 Introduction

High quality graphene was first obtained by Novoselov *et al.*.[106] Replication of such unique electronic transport properties at wafer scale is clearly of great commercial interest. However, large scale industrial fabrication along with the ability to transferring graphene onto desired substrates is still challenging. Current standalone growth, as well as growth and transfer technologies results in detrimental structural and electronic quality, as described earlier in Chapters 3 and 4.[92,147] CVD on metallic substrates is the subject of much exploration in large scale graphene production.[111] This is due to the versatility of subsequent transfer to substrates of technological interest, beyond SiC.

Beyond structural defects such as strain and rippling, current densities are also affected by point intrinsic and processing-derived defects.[120,136] These defects also compromise device efficiency, and a fundamental understanding of these defects at the electronic level is long due. Indeed, current characterization techniques feature either atomic resolution in short topographic range (i.e., EELS[180]) or limited resolution in a longer topographic span (i.e., Raman[150]). Either approach brings limited information to point defects derived from growth and processing to inform fabrication.

Ideally, a fully-informing approach would feature both a topographic span, comparable to that of wafer levels, combined with specific molecular sensitivity. Such

level of specificity would be both chemical and morphological, to comprehensively identify defects through spectroscopic fingerprints. Nevertheless, data created by intertwining high resolution with topographic span will surely yield a high level of information complexity. Fortunately, advent of statistical and/or artificial intelligence in the realm of materials research could be deployed in this scenario for comprehensive information extraction.

In this chapter, spectroscopic fingerprints of graphene point defects are provided to construct a theoretical database. This database, will enable data-mining through data-centric routines to produce qualitative and quantitative analysis of highly complex experimental hyperspectroscopic shown in Chapter 3. Moreover, the 2D community has expressed strong interest in defect modeling towards experimental verification.[112,119,181,182]

Along this lines, this chapter is dedicated to perform structural and electronic density functional theory analysis of pristine and defective graphene. The defects addressed in this work are single vacancy, single vacancy passivated with 3 hydrogen atoms, Cu adsorbed and Cu substitutional.

The first three defects are likely to happen during the CVD growth and post-processing. Although, single vacancy would require extra energy to be formed. Cu substitutional defect is adopted for completeness since it is very unlikely to occur in CVD. The high spatial localization of those defects make them suitable to monitor their impact in the NEXAFS spectrum along the point defect. Finally, it is proposed a procedure to generate angle-resolved NEXAFS fingerprints from first-principles calculations of NEXAFS spectra over a set of absorbing atoms placed nearby the defect.

5.2 Computational Details

Four topological defects on graphene were fully relaxed beyond pristine graphene (G), i.e single vacancy (SV), single vacancy passivated with 3 hydrogen atoms (SVP), Cu atom substitutional (Cu-sub) and Cu atom adsorbed on graphene (Cu/g) using plane-wave density functional theory implemented in Quantum Espresso within the pseudopotential approximation.[122,124] We employed ultrasoft pseudopotentials, energy cutoff of 25 Ry for plane wave basis set and 300 Ry for charge density, k-sampling grid in the Monkhorst-Pack scheme of $10{\times}10{\times}1$ and vacuum of 20 Å

along the Z-axis. Total energy criteria were set to 10^{-6} Ry while electronic self-consistent energy criteria of 10^{-8} was adopted. Atomic forces at equilibrium position were converged below 0.02 eV/Å. All atoms were allowed to move during the structural relaxation and were modelled under the general-gradient approximation (GGA) with the Perdue-Burke-Ernzerhof (PBE) exchange-correlation functional.[123] Electronic density of states at ground state were performed by sampling the Brillouin Zone with $10 \times 10 \times 1$, where convergence of Fermi energy is achieved within the self-consistent field calculations of 0.01 eV. Given the symmetry breaking induced by defects and the strong correlation of the spectral fingerprint with the absorption site as well as the adjacent environment,[85] the identification of absorption sites is crucial for the definition of the defect spectral fingerprinting. Likely adsorption sites of individual Cu atom on pristine G are: the Hollow site above the center of the hexagon (H), the Top site just above the carbon atom (T) and the Bridge site within a C-C bond (B) as represented in Figure 5.1.

To simulate NEXAFS spectra the size of supercells provide a suitable distance between absorbing atoms to avoid interaction between them due to the periodic boundary conditions, typically greater than 10 Å. NEXAFS spectroscopy calculations at C K-edge were modelled in the framework of the excited electron and core-hole (XCH)[86] approximation at 30°, 45°, 54°, 60°, 75°, 85°, and 90° angles of incidence of the X-ray beam to monitor $\pi^*_{C=C}$ and σ^*_{C-C} resonances on defective graphene. In order to simulate the excitation of the carbon atom due to the X-ray, one electron from the $1s$ level of the carbon pseudopotential has been removed. Several carbon atoms from the supercell has been used to calculate the unoccupied states under the pseudopotential approximation that includes the core-hole interactions. XCH-NEXAFS uses the PBE form for the exchange-correlation potential within GGA approximation.[123]
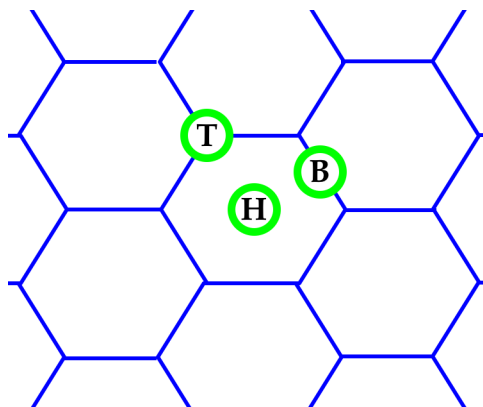
Figure 5.1: Possible localization of adsorbed atoms: Hollow (H), Bridge (B) and Top (T) positions, a top view.

5.3 Structural, Energetic and Electronic Characterization of Topological Defects

Structure Analysis

Fully relaxed systems are presented in Figure 5.2. Figure 5.2a shows a Cu/g configuration with Cu adsorbed atom at the top site. Top site is the most stable configuration with respect to H and B sites as found in the literature[a].[183,184] In Figure 5.2a2, out-of-plane lattice distortion in the vicinity of Cu atom is observed as a result of strong nuclear repulsion caused by Cu atom, as well as, the relative distance of Cu adatom respect to C atom placed below is found to be 2.065 Å under a GGA approach. In addition, despite of local perturbation due to Cu adatom the whole lattice preserves a certain degree of symmetry as seen in Figure 5.2a1. SVP has reached its structural equilibrium through the in-plane arrangement of H atoms as shown in Figure 5.2b. Although, the extent of the lattice deformation around the defect (Figure 5.8b1) has been found much bigger than SV (Figure 5.2d1), the presence of H atoms contribute to stabilize the dangling bonds induced by the vacancy, thus maintaining the sp^2 character. Indeed, SVP is found to be the most stable structure, as we will discuss later. SV relaxed to a structure with no out-of-plane perturbation. Lastly, Cu-sub configuration shows the highest in-plane deformation of the lattice (Figure 5.2c and Figure 5.2c1), as well as, no signs of out-of-plane perturbation.

---

[a]We should mention in this work, we only explored the T site conformation since it has been proven as the most stable configuration with respect to Bridge and Hollow positions.
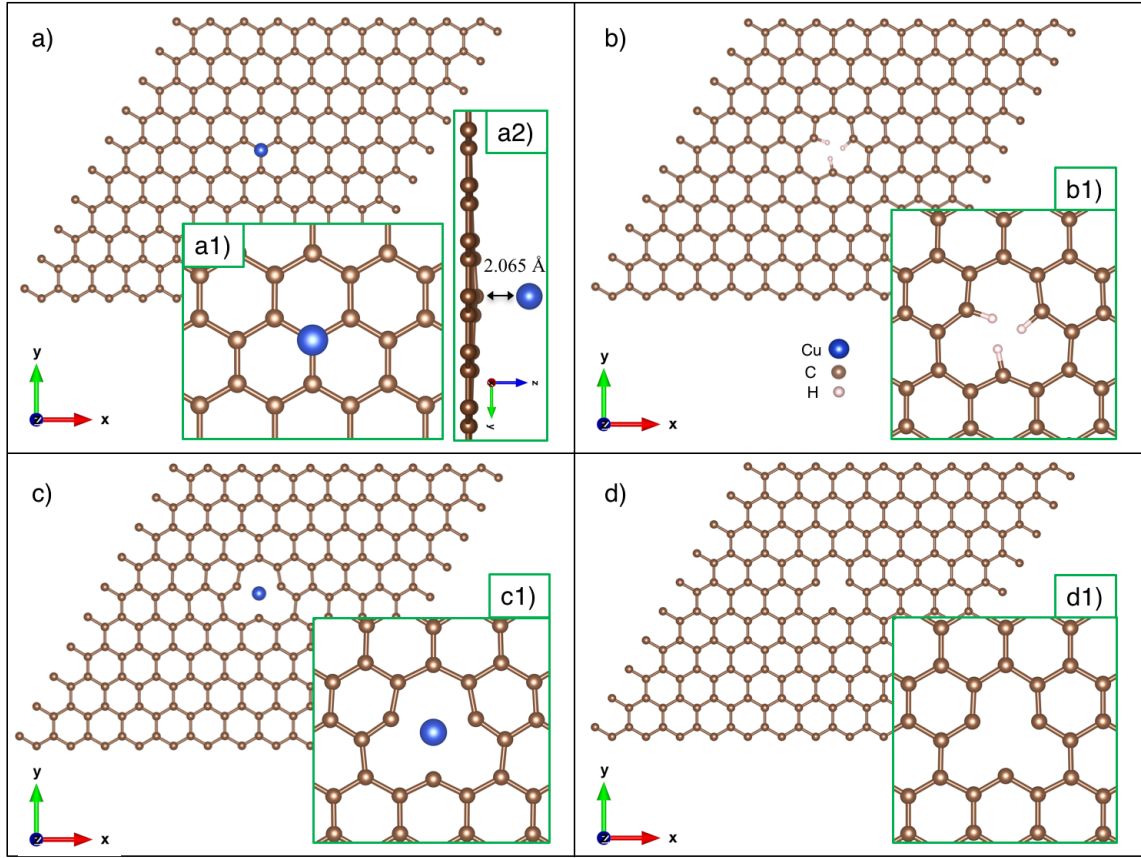
Figure 5.2: Relaxed structures of topological defects on graphene. (a) Cu atom adsorbed on graphene (Cu/g). (b) Single vacancy passivated with 3 hydrogen atoms (SVP). (c) Cu atom substitutional (Cu-sub). (d) Single vacancy graphene (SV).

Energetic Analysis

Formation energies of E_{SV}, E_{SVP}, $E_{Cu/G}$ and E_{sub}^{Cu} defects where estimated according to Equation 5.1, written below:

System	Formation energy (eV)
E_{SVP}	-5.03
$E_{Cu/g}$	-0.46
E_{sub}^{Cu}	5.52
E_{SV}	7.95

Table 5.1: Computed formation energies of atomic defects on graphene. SVP is found as the most stable and Cu-sub as the least energetically favourable system.

$$E_{SV} = E_{G+SV} - \frac{N-1}{N}E_G$$

$$E_{SVP} = E_{G+SVP} - \frac{N-1}{N}E_G - 3E_H$$

(5.1)

$$E_{Cu/g} = E_{G+Cu/g} - E_G - E_{Cu}$$

$$E_{sub}^{Cu} = E_{G+Cu_{sub}} - \frac{N-1}{N}E_G - E_{Cu}$$

where N in the number of carbon atoms in the model of pristine graphene sample. E_{G+SV}, E_{G+SVP}, $E_{G+Cu/g}$ and $E_{G+Cu_{sub}}$ are the computed total energies of defective graphene, namely, SV, SVP, Cu/g and Cu-sub, respectively. Analogously, E_{Cu} and E_H are calculated energies of isolated Cu and H atoms, and E_G is the total energy for pristine graphene. Energies estimated in Table 5.1 point SVP as the most stable configuration with -5.03 eV followed by Cu/g with -0.46 eV, which is an order of magnitude smaller than SVP. On the contrary, Cu-sub and SV exhibit positive values of 5.52 eV and 7.95 eV, respectively. Therefore, these two structures are energetically unfavourable but still being considered in this work for the sake of com-

pletion, specially SV given the abundant theoretical and experimental literature[b]. [185]

Electronic Structure Analysis

NEXAFS spectra is sensitive to perturbations on the unoccupied electronic states in graphene. We performed calculations of DOS to analyze the electronic structure of pristine and defective graphene. As a first observation, these topological defects under study have induced the appearance of electronic states at the Fermi level as shown in Figures 5.3b-e. The redistribution of electronic states are comparable in intensity but exhibits particular characteristics. For instance, the presence of a single peak at Fermi level in SVP and Cu/g systems (Figures 5.3b and c) clearly differ from the two peaks observed around Fermi level in Cu-sub and SV (Figures 5.3d and e). Moreover, in these two last defects the highest peak near the Fermi level is located below the Fermi level in the case in Cu-sub and above Fermi level in SV. In all cases, non-significant changes are observed in the conductance states apart from the peaks earlier mentioned. Such case is slightly different in the valence states where perturbations are observed, especially around 2.5 eV where peak became less sharp in all cases and split in case of SVP and Cu/g respect to pristine graphene (Figures 5.3b and c). Therefore, effects of topological defects on the electronic density are significant in the range of 5 eV centered at Fermi level.

In Figure 5.4 are presented the density of states of topological defects with their Fermi level of pristine graphene taken as a reference, for measurement and visualization purposes, as indicated by δ_i in the insets. Notice that peak at $\sim$2 eV below and closed to the Fermi level of Cu/g (Figure 5.4b) correspond indeed to an additional electronic states not observed in pristine graphene. In fact, we can see that Cu adsorbed on graphene as higher impact on the electronic structure beyond and below Fermi level respect to the other systems.

Charge transfer is a process that can be conveniently monitored through NEXAFS spectra, in particular the $\pi^*_{C=C}$ exciton feature, due to the relocation of the Fermi level, as discussed in Chapter 4.[92] Charge transfer was qualitatively analyzed from the differential DOS. $\delta_{i;i=1..4}$ presented as insets in Figures 5.4a-d measure both direction and magnitude of Fermi level displacements. In Table 5.2 the corresponding δ and converged Fermi energy's values are shown. Notice that only

---

[b]Calculations and analysis of more energetically accessible samples are in progress and expected to be ready after the submission of this thesis.
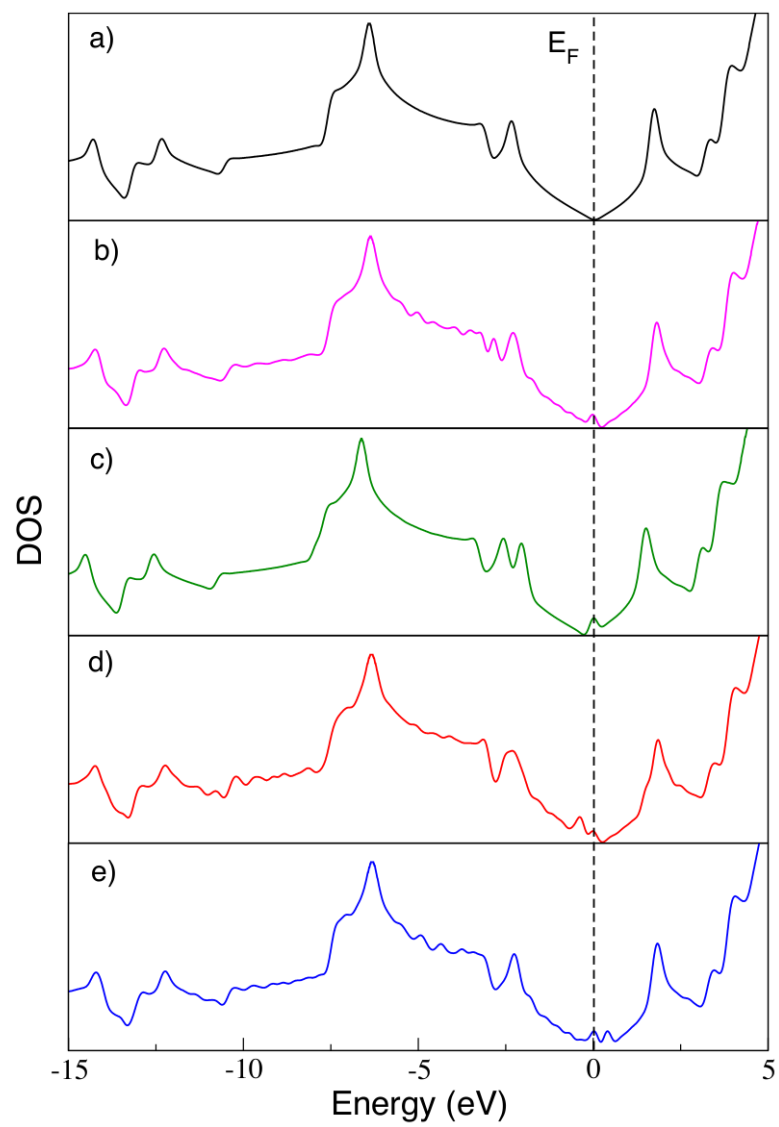
Figure 5.3: Density of states. (a) Pristine graphene. (b) Single vacancy passivated. (c) Cu atom adsorbed. (d) Cu atom substitutional. (e) Single vacancy.

System	Fermi energy (eV)	δ (eV)
G	-2.741	-
SVP	-2.810	-0.069
Cu/g	-2.499	0.242
Cu-sub	-2.845	-0.104
SV	-2.849	-0.108

Table 5.2: Relative Fermi energy shifts of topological defects respect to pristine graphene.

Cu/g system has given a positive quantity. Positive δs mean that systems have increased their number of occupied electronic states, whereas, systems with negative δs experienced the opposite effect, i.e., additional unoccupied electronic states are available upon charge density redistribution. Therefore, in SVP, Cu-sub and SV structures removed/substituted C atom has induced additional unoccupied states. Even when additional electrons (available from Cu atom in the case of Cu-sub structure) do not restore the initial electronic distribution of states, possible due to the non-covalent nature of substitutional Cu in graphene. Indeed, the ability of H to form covalent bonds reduced the amount of unoccupied states, as reflected by δ magnitude of -0.069 eV, which is nearly half for Cu-sub and SV (Table 5.2). Following the previous analysis, it can be observed the opposite behavior for the Cu/g structure, i.e., Cu electronic states promoted significant contribution of occupied states, reflected in higher δ value and longer positive displacement (Figure 5.4b).
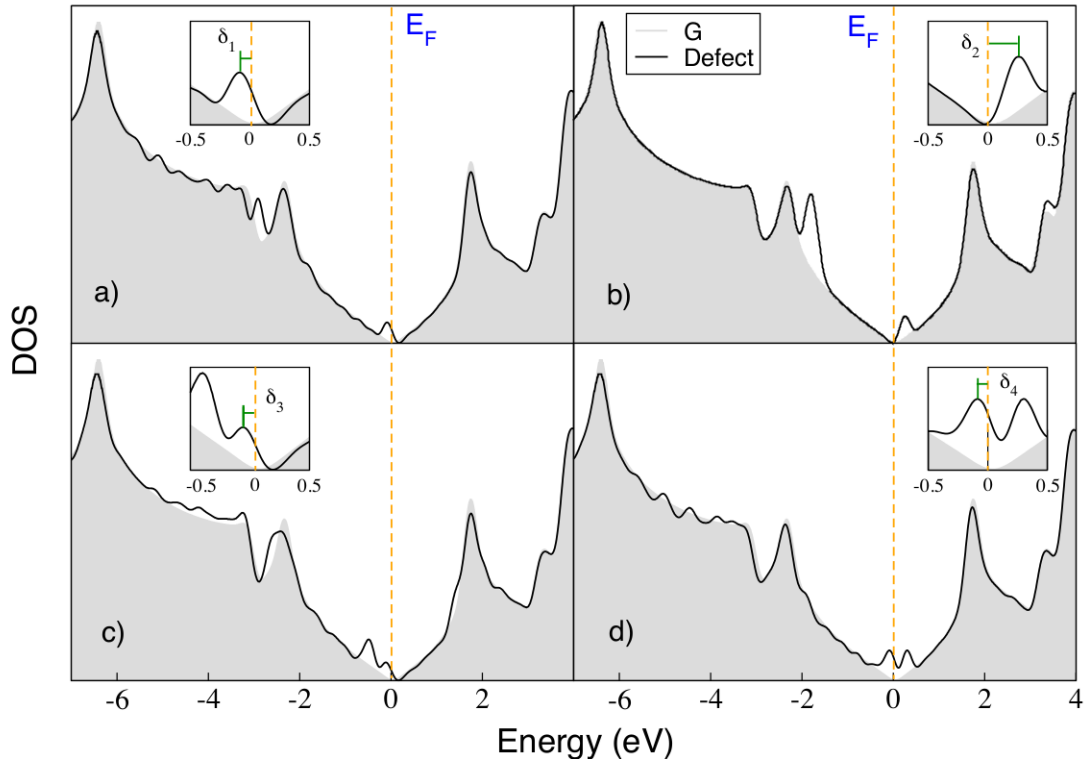
Figure 5.4: Differential density of states. (a) Single vacancy passivated. (b) Cu atom adsorbed. (c) Cu atom substitutional. (d) Single vacancy. Grey area is graphene and black lineshape is the defect. Insets show Fermi energy shifts of defects respect to pristine graphene.

5.4 Angle-Resolved NEXAFS Spectral Variation as per Action Range of Topological Defects

Region of Interest (ROI) and definition of Physical Parameters

To develop a methodology that account for the chemical physics properties induced by the formation of defects on graphene, it was established a set of absorbing atoms grouped according to their relative distance from the point defect position, as shown in Figure 5.5. In the present analysis, it is identified six groups of absorbing atoms differentiated by the color code proposed in Figure 5.5.
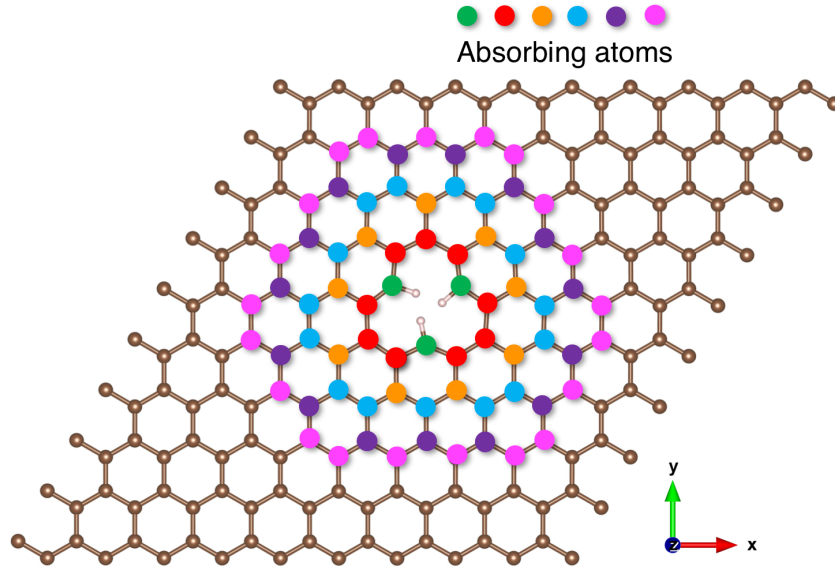
Figure 5.5: Identification of absorbing atoms taken into account to computed NEX-AFS spectra.

Additionally, in Figure 5.6 we have defined approximated circular areas as our region of interest (ROI) where each ROI contains the prior in size ROI thus we can account accumulative effects. These areas could provide experimentally measurable values . Corresponding radii are detailed in the inset of Figure 5.6. Every topological defect has dimensions of 2.47 nm $\times$ 2.47 nm, such dimensions are enough to prevent interaction between same defects due to the periodic boundary conditions of DFT calculation.

Another measurable quantity reported here is the atomic excitation density (ρ) defined as the number of absorbing atoms per ROI. Estimated ρ for every ROI and corresponding values of every ROI are shown in Figure 5.7.

Angle-Resolved NEXAFS spectra

Characteristic Carbon K-edge NEXAFS spectrum of specific ROI was built by averaging individual NEXAFS spectra of every absorbing atoms that composed the ROI of interest. Subsequently, angular projection at 30°, 45°, 54°, 60°, 75°, 85° and 90° were performed to account for polarization dependence feature of NEXAFS. For clarification, projection at 90° correspond to an incident beam perpendicular to the sample plane therefore enhancing the σ^*_{C-C} resonance feature. At first glance,

Area Label		Radius (nm)
A_1		0.25
A_2		0.49
A_3		0.74
A_4		0.99
A_5		1.24
A_6		1.48
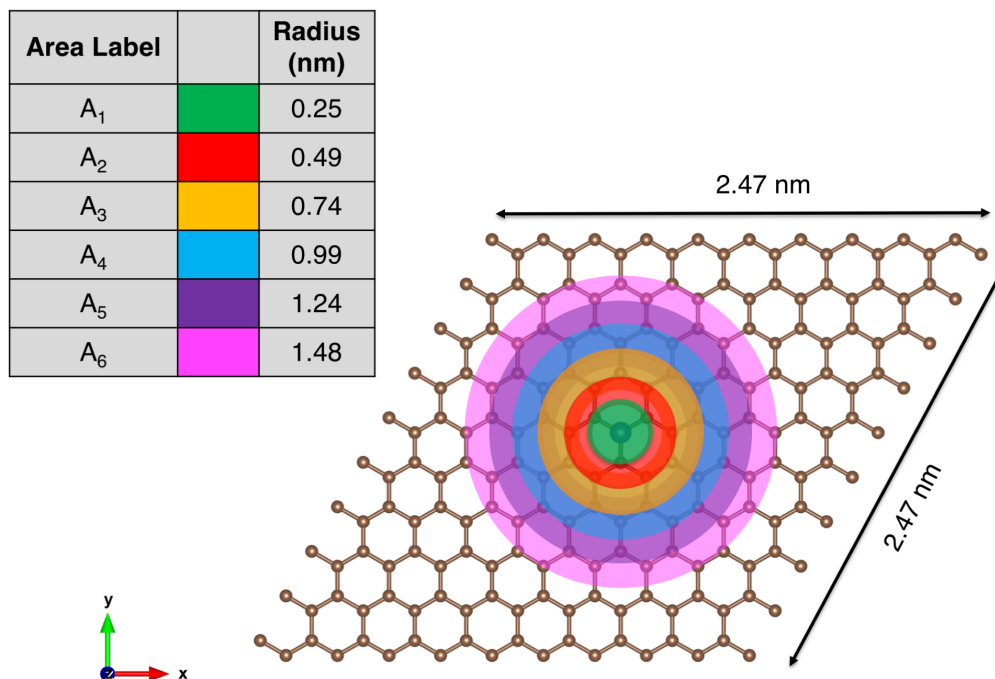
Figure 5.6: Definition of region of interest (ROI). Larger radius of selected ROI includes absorbing atoms of smaller ROI - accumulative feature.

	Area	Area (nm²)	Radius	Radius (nm)	ρ_{SV}, ρ_{SVP}, $\rho_{Cu\text{-}sub}$ (*)	$\rho_{Cu/g}$ (*)
	A_1	0.20	R_1	0.25	15.3	20.4
	A_2	0.75	R_2	0.49	15.9	17.2
	A_3	1.72	R_3	0.74	12.2	12.8
	A_4	3.08	R_4	0.99	11.7	12.0
	A_5	4.83	R_5	1.24	10.6	10.8
	A_6	6.88	R_6	1.48	10.5	10.6
(*) number of absorbing atoms/nm²						

Figure 5.7: Assigned ROI code color, ROI and corresponding radii values, and atomic excitation density (ρ).

Figure 5.8: SVP structure. (a)-(e) Progression of averaged NEXAFS spectra for every ROI and projected at seven incident angles. R as radius of the ROI.

we have observed a restoration of main characteristic $\pi^*_{C=C}$ and σ^*_{C-C} resonances of pristine graphene as ROIs are progressed in size (Figures 5.8-5.10), which are expected since less electronic and geometric perturbations are experienced by absorbing atoms located farther from the point defect.

In the SVP structure the C-H bonds produced very intense resonance peak at ~ 5 eV (Figure 5.8a) and a wide and low intensity σ^*_{C-C} resonance at ~ 7.5 eV. Also, it is observed another feature at ~ 0 eV (Figure 5.8a), which we believe is the $\pi^*_{C=C}$ but shifted to lower energy with respect to Figure 5.8f which resembles to pristine graphene spectra. Indeed, the former peak is shifted to ~ 1.5 eV whereas σ^*_{C-C} and C-H resonances are only reduced in both cases and shaped to unperturbed lineshape, respectively, as ROI has increased (Figures 5.8a-f). It is worth to mention that C-H assigned feature does not disappear even at the largest ROI, evidencing long range of action characteristic.

In contrast, less perturbed effect on NEXAFS spectra is observed in Cu/g struc-
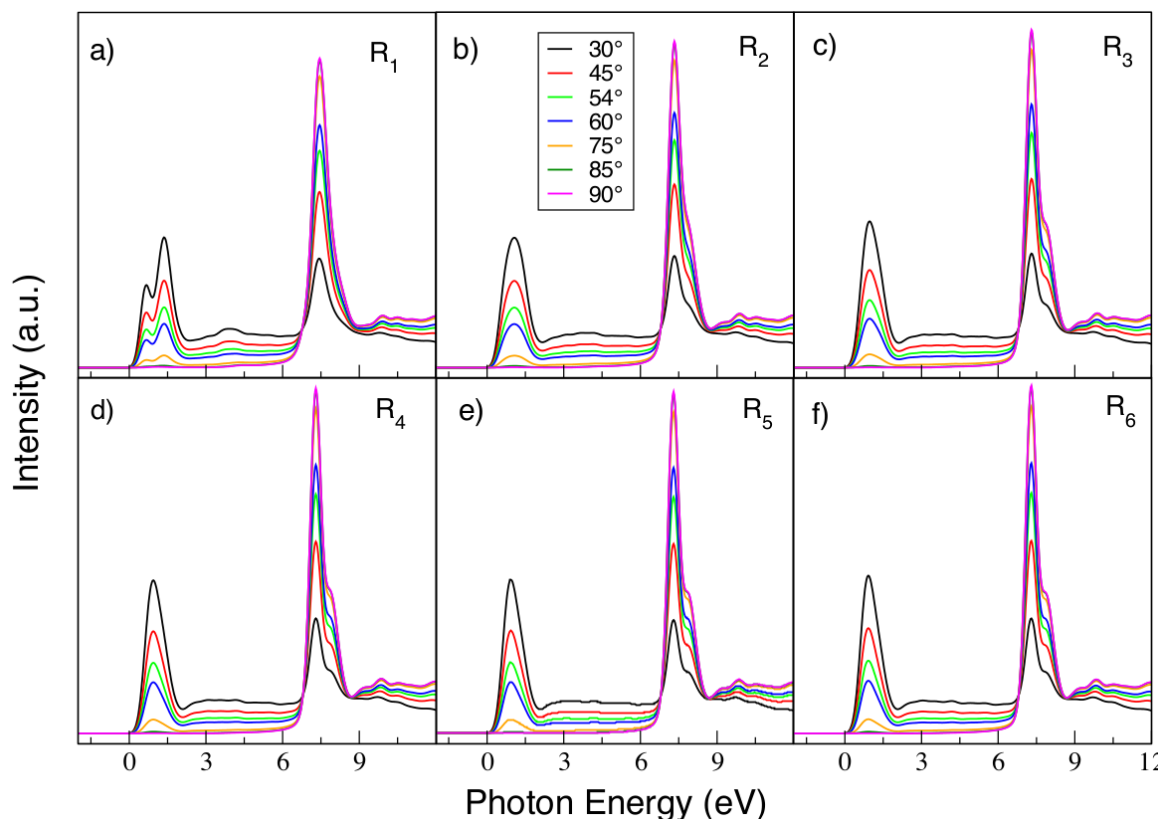
Figure 5.9: Cu/g structure. (a)-(e) Progression of averaged NEXAFS spectra for every ROI and projected at seven incident angles. R as radius of the ROI.

ture, this due to non-covalent bonding of Cu atom with local C atoms try to preserve the original electronic structure. In fact, the extent of effect on NEXAFS is restricted to at least the second ROI, as evidenced in Figure 5.9a-f. Also, the only significant perturbation observed is the double $\pi^*_{C=C}$ resonance in the first ROI (Figure 5.9a). This confirm the short range impact of Cu adatom.

Presence of dangling bonds induced by C vacancy in SV structure has generated a characteristic convoluted feature between -1.5 and 0 eV that is mitigated by progressing sizes of the ROI (Figures 5.10a-f). Conversely, $\pi^*_{C=C}$ and $\sigma^*_{C=C}$ resonances area restored from initial broader and lower intensity lineshapes, but remaining the peak at energy range -1.5 - 0 eV, even at the largest ROI (Figure 5.10f). Finally, despite Cu-sub system (Figure 5.11a-f) showed some interesting features no further analysis is done since it has been considered only for completion and energetically expensivie in experiments, as mentioned earlier in this chapter.
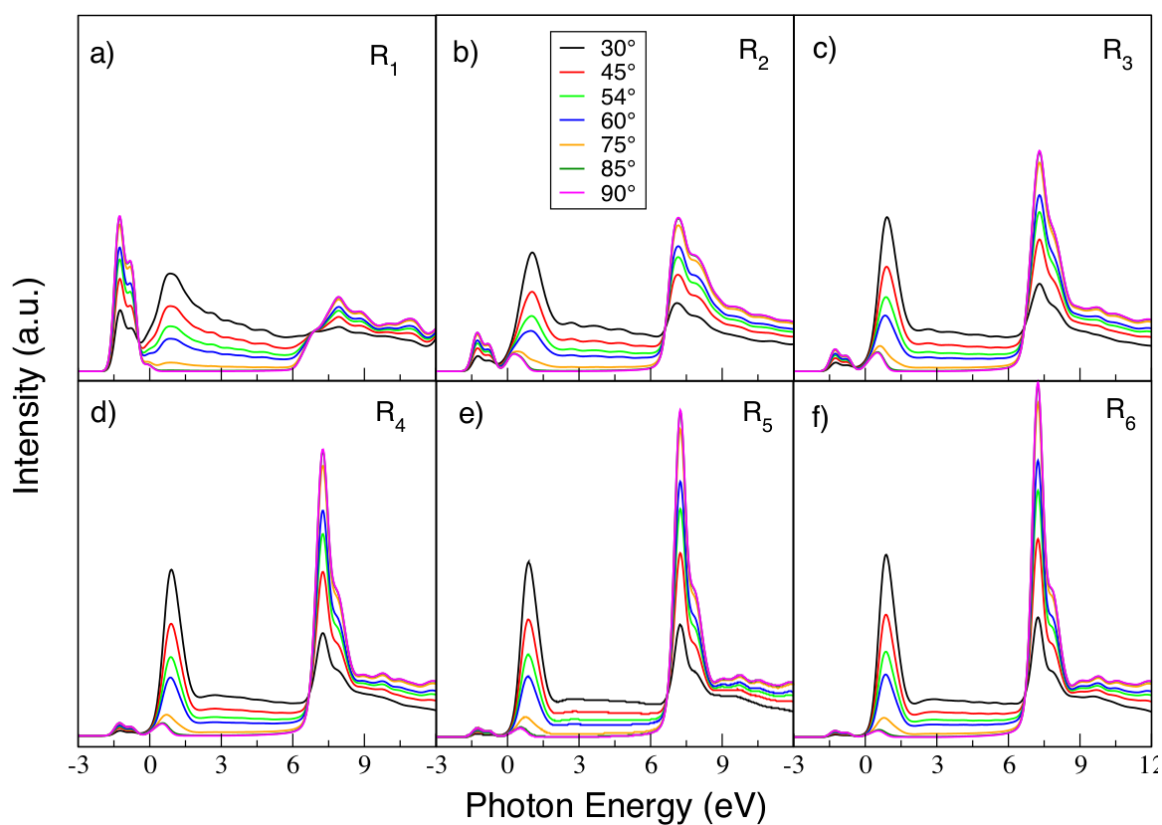
Figure 5.10: SV structure. (a)-(e) Progression of averaged NEXAFS spectra for every ROI and projected at seven incident angles.
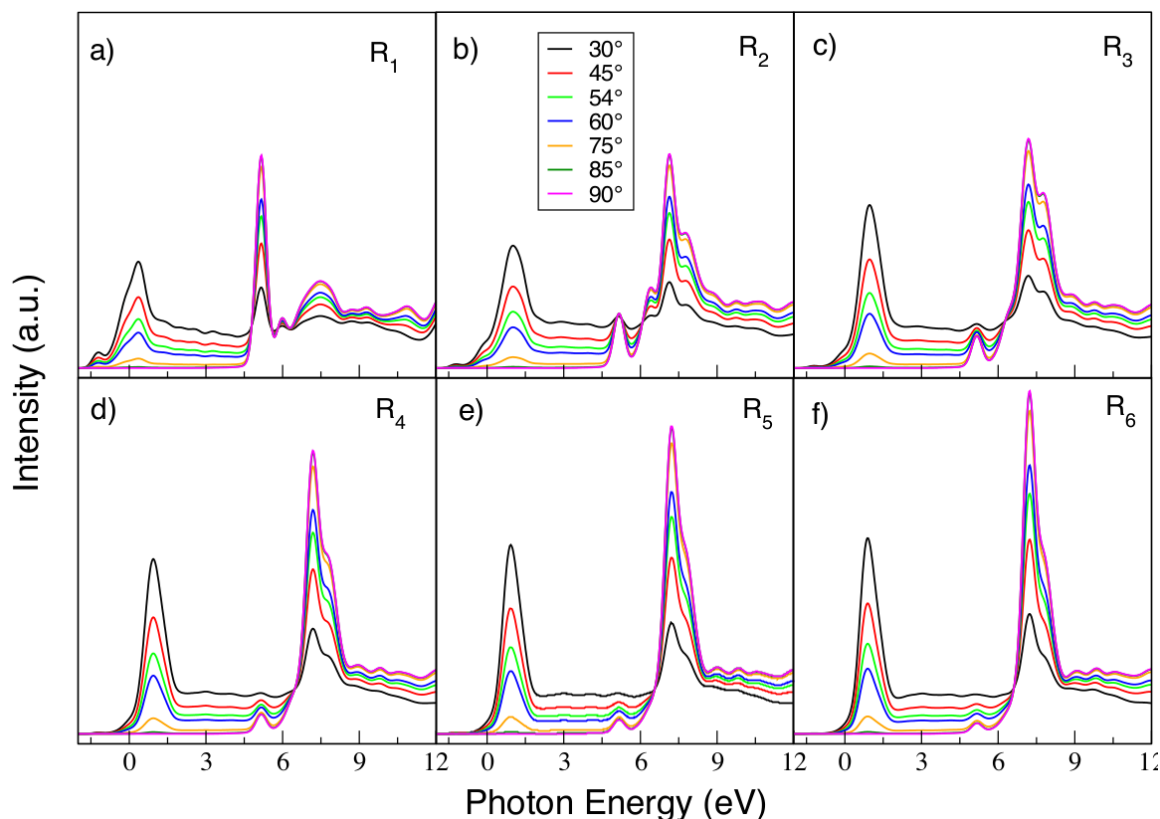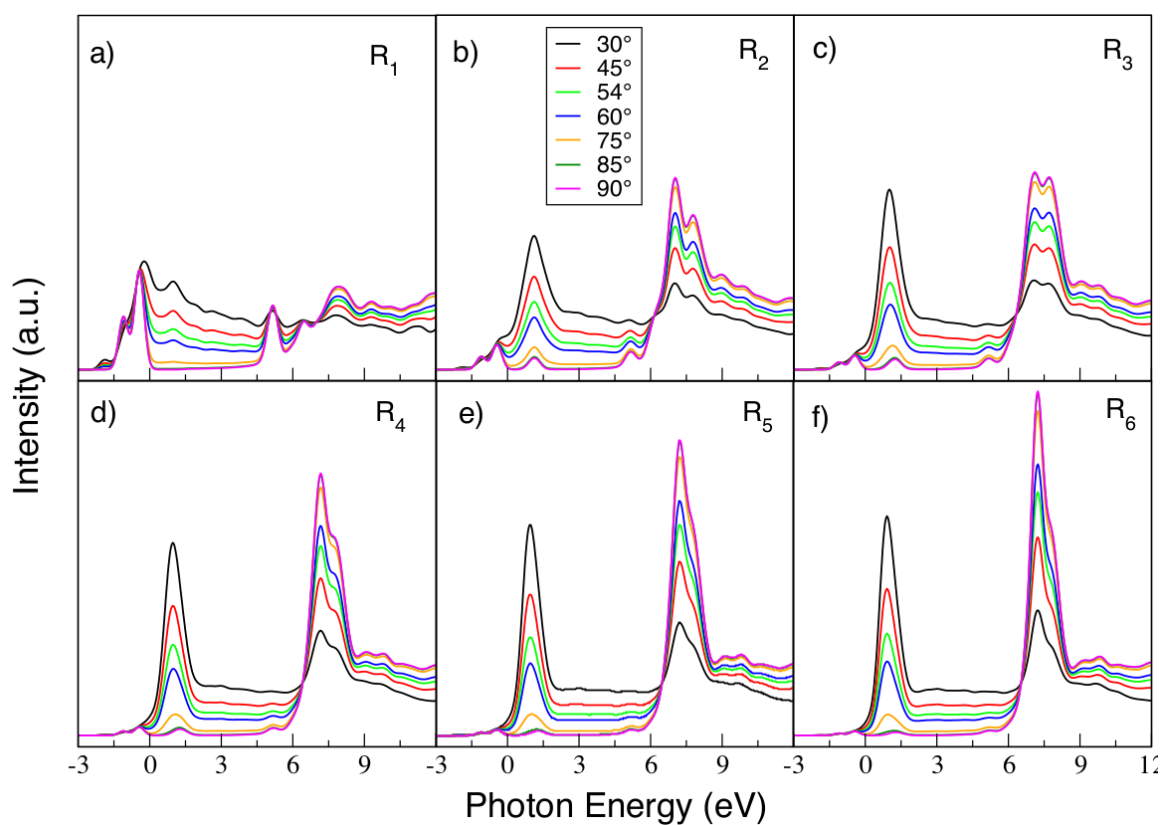
Figure 5.11: Cu-sub structure. (a)-(e) Progression of averaged NEXAFS spectra for every ROI and projected at seven incident angles.

5.5 Fingerprints through Angle-Resolved Spectroscopy for the Identification of Topological Defects

The previous analysis provided several options when it comes to select the ROI, as well as, the capability to enhance peaks intensities by variation of angular projection. Figure 5.12 is plotted at incident angle of 54° to better visualization of NEXAFS spectra as ROI progress in size. This angle is known to be appropriated to enhance both $\pi^*_{C=C}$ and $\sigma^*_{C=C}$ excitations. In this plot (Figure 5.12) it is more evident the degree of influence of defect on the NEXAFS fingerprints. Once again, with Cu/g system as the least perturbed but observable at smaller ROI (Figure 5.12b).
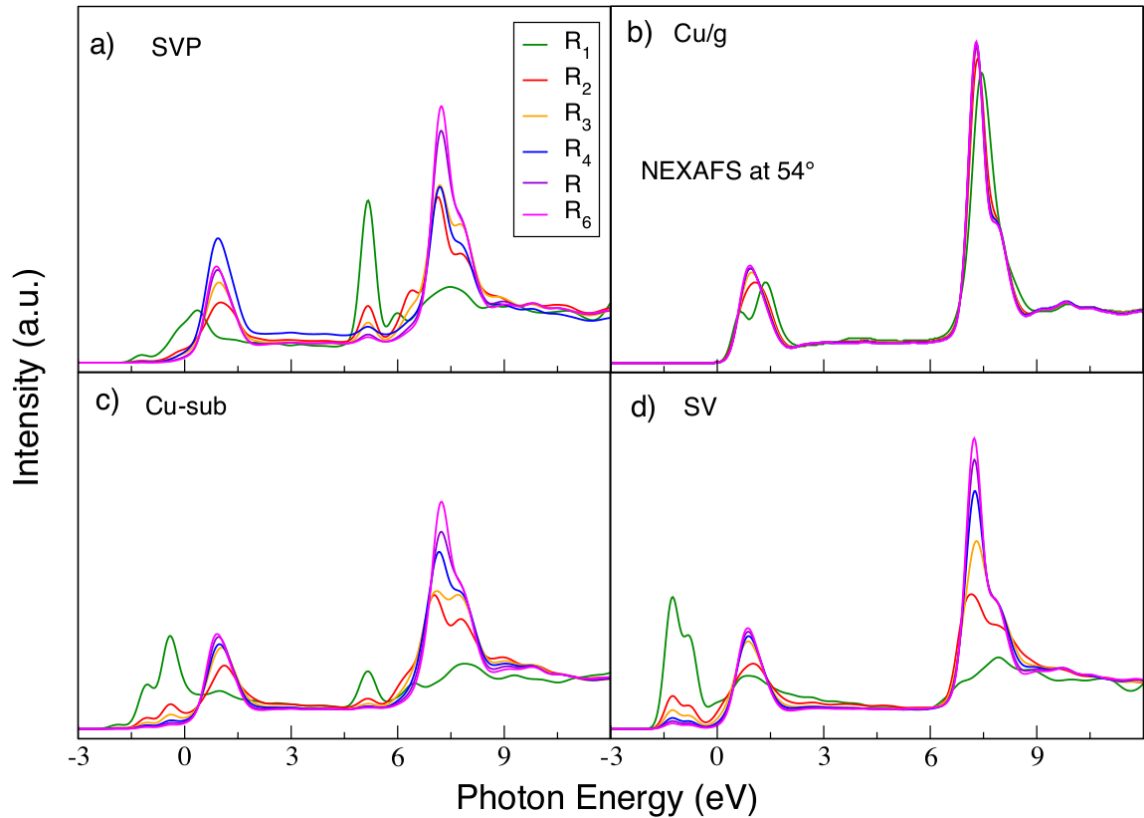
Figure 5.12: Effect of ROI progression on averaged NEXAFS at incident angle of 54° for each topological defect.
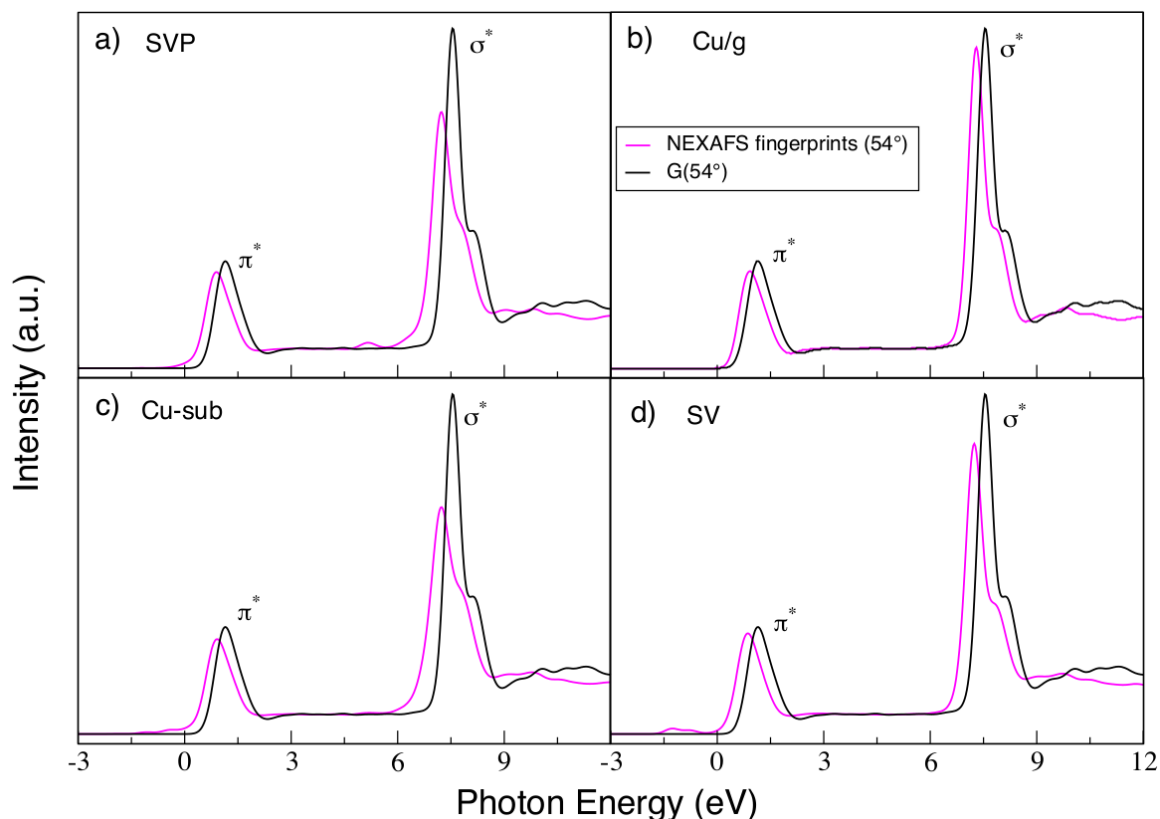
Figure 5.13: Distinctive NEXAFS fingerprints extracted from the largest ROI at incident angle of 54°.

We presented in Figure 5.13a-d the NEXAFS fingerprints extracted from the largest ROI and at 54 ° of incidence. NEXAFS fingerprints are plotted against pristine graphene (G) at same incident angle for the sake of comparison. In all cases NEXAFS fingerprints spectra are shifted with respect to pure graphene. As described before, in SVP structure is still observed a feature assigned due to C-H bonds below 6 eV (Figure 5.13a), while a broad feature is noted above -1.5 eV for SV (Figure 5.13d). Finally, it is noted an subtle increment of slope curvature at raising edge of $\pi^*_{C=C}$ in SVP, SV and Cu-sub (Figures 5.13a,d,c) as a consequence of electronic structures perturbation around the Fermi energy. Finally, in Figure 5.14 is compared angular projection of NEXAFS fingerprints at largest ROI with respect to graphene.
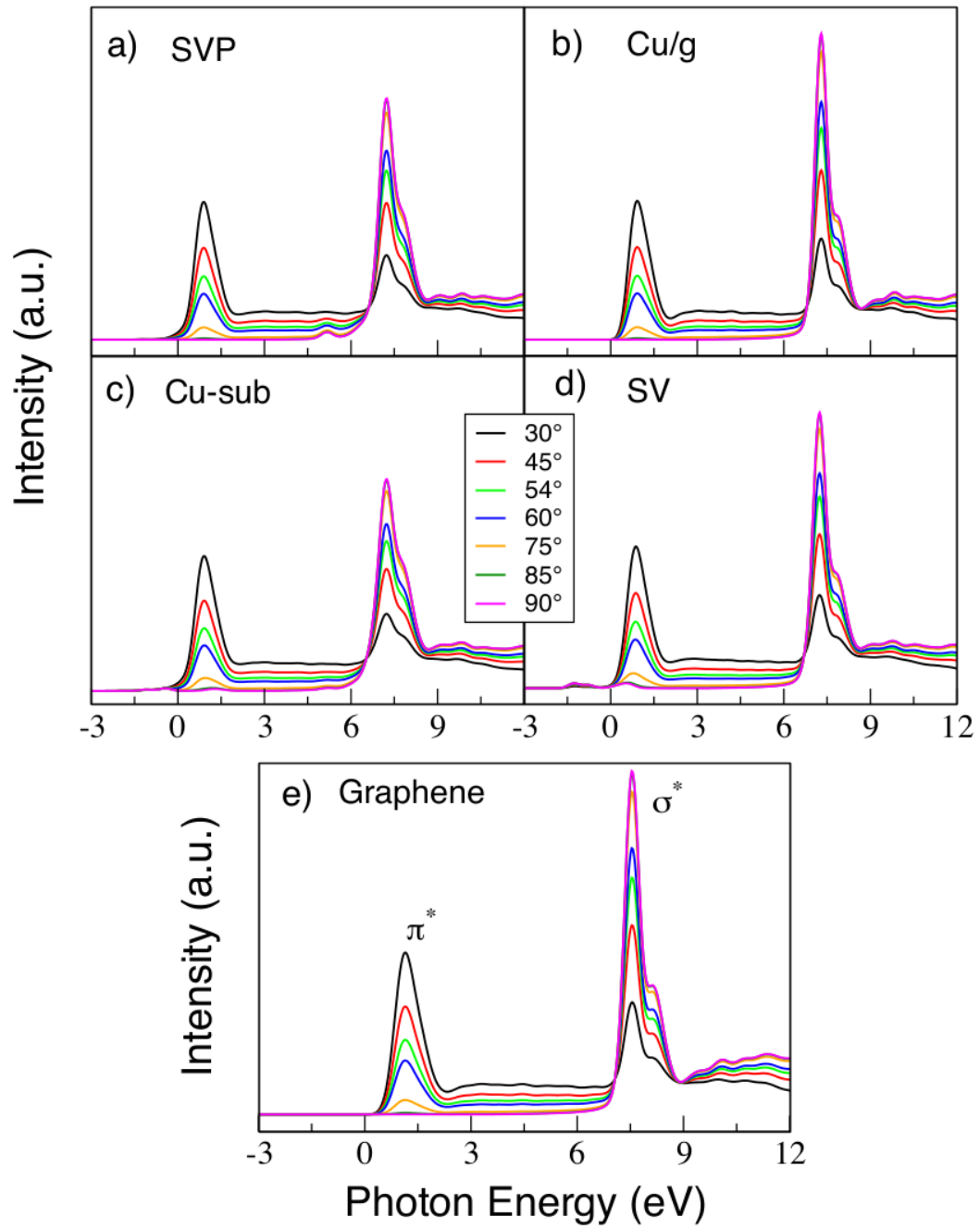
Figure 5.14: Angle-resolved NEXAFS spectra of topological defects - Largest ROI.

5.6 Summary

Sophisticated computational studies of NEXAFS spectra have been presented as the primary tool to characterize and build a database consisting of four topological defects on graphene, with the purpose of characterizing point defects. A simple but practical methodology to build and analyze modeled point defects is proposed. This methodology could be applied to other similar defects, i.e., small adsorbed chemistry radicals, different adsorbed atoms, Stone Wales, etc. Intensity and shape of distinctive pristine graphene resonances (i.e., π^* and σ^*) are directly correlated with the size of ROI. This suggests that further studies including concentration of defects per unit area, in particular for short-range defects, could be beneficial towards the refinement of the original fingerprints.

DFT calculations have been employed to study the implications of charge density and ground state DOS according to the type of defect. Future work will focus on the design of data-centric approaches. These approaches will identify point defects by deploying these fingerprints on experimental hyperspectral data.

6

Conclusions and Further Work

6.1 Conclusions

In summary, this work has demonstrated that combination of first-principles NEX-AFS simulations along with experimental hyperspectral NEXAFS and data analytics is a feasible approach to characterize in-plane and out-of-plane deformations of graphene at wafer scale. The wealth of information embedded in hyperspectral NEXAFS can be further exploited through initial calculations of NEXAFS fingerprints of defects on graphene, combined with statistical and artificial intelligence techniques. The foundation to this approach has been provided here.

Data analytic methods explored in Chapter 3 have shown that 4LG/SiC-C is the most pristine and epitaxially grown graphene is the most deformed (out-of-plane deformations). The orbital vector approximation stood out as the most sensitive methodology. In addition, DBSCAN evidenced variation in the length-scales of corrugations which implies that frequency of defects has more impact in the α parameter. Consequently, further exploitation of such α to correlate out-of-plane deformations with transport properties at wafer scales is envisioned. Indeed, this approach could be employed to monitor multilayer graphene and other bi-dimensional materials as long as characterization of the appropriate simulated and experimental standards is available.

An important contribution of this work is that lattice parameter can be efficiently predicted, and therefore strain can be measured through the correlation between σ^* energy position and lattice parameter obtained from *ab initio* simulations. Such correlation relies on the excitonic nature of σ^* resonance. Results in Chapter 4 suggest the applicability of this method to Cu supported CVD-grown

graphene, and extended to transferred multilayers of graphene as long as existing van der Waals forces are weak. Even more, we can apply this technique to graphene with underlying SiC substrates if details of how substrate interact with graphene are accounted for and understood previously. In principle, variations of this method could be applied to different transition metals substrates but effects of charge transfer and substrate screening need to be assessed in order to isolate the σ^* energy dependence on bond length and strain. Therefore, this technique is promising to analyze other 2D materials, especially with the advent of tabletop X-ray source driven by lasers than can be used to acquire XAS spectra as accurate as those obtained at synchrotrons.[186] To this end, further work is required to analyze the correlation between functionalization and dimensional reduction.

Finally, the case study about the calculation of characteristic angle-resolved NEXAFS spectra (spectral fingerprints) of four defects on graphene has been addressed. Impact of such defects on spectral fingerprints as increased of density of absorbing atoms (i.e., number of absorbing atoms per region of interest), and the level of recovery of the pristine NEXAFS features were effectively investigated through this methodology. In this case study, Cu/g showed the highest level of recovery. Additionally, the angle-resolved analysis of NEXAFS spectra is useful to assess features of particular spectral resonances together with electronic structure studies. The technique presented in Chapter 5 can be easily adapted to other 2D materials and defects with highly localized spatial nature. To this end, further studies including concentration of defects could be beneficial towards the refinement of NEXAFS fingerprints, and consequently contribute to the NEXAFS database as the Materials Genome Initiative states.

6.2 Current and Future Work

An immediate investigation that emerges from what is presented in Chapter 5 is the extension of the set of distinctive NEXAFS spectra to further defective systems, in particular, to those defects involved in manufacturing of reduced graphene oxide, at first place. As a consequence, we envision the use of those spectral fingerprints with available deep learning algorithms to perform analytic characterization of experimentally synthesize reduced graphene oxide for instance. As a matter of fact, preliminary results of additional fourteen new target defective systems comprising

relaxed structures, formation energies and NEXAFS fingerprints are presented in Appendix A.

On the biological realm, further studies through NEXAFS spectroscopy from the combined experiment-theory point of view are being currently undertaken. Those consists of proposing a molecular modeling to estimate charge exchange at interfaces between carbon nanotubes (CNTs) and non-covalent dispersants, i.e., dimethyl sulfoxide (DMSO). In that context and for the sake of simplicity, only results of preliminary simulations (relaxed structures, adsorption energies and NEXAFS spectra) of DMSO-graphene samples are shown in Appendix B, although experimental NEXAFS, Raman and Microscopy characterization has already been performed by Dr. Campo motivated by her earlier studies on bonding dynamics of modified CNTs which have been successfully injected into developing drosophila embryos proving thus to be a in vivo model with high performance to investigate CNT toxicity.[187]

A

Further NEXAFS Fingerprints Database of Defects on Graphene

The following set of defects on graphene presented here are of broad interest in chemical exfoliation techniques to obtain graphene oxide and subsequent reduction. Reduction is typically applied to restore the graphene π-conjugation feature which is damaged by previous oxidation process. Such chemical oxidizing agents add several functional groups (i.e., hydroxyl, carboxyl, epoxy, vacancies, etc) to graphene oxide surface. Also, the use of hydrazine (N_2H_4) and ammonia (NH_3). for reduction add further defects, as well as NEXAFS spectroscopy has been systematically applied to identify and understand local geometry and electronic structure of such defects.[188,189] To this end, the search of computationally assisted angle-resolved NEXAFS fingerprints and their integration with machine learning algorithms to carry out analytic characterizations is of great value.

A.1 Relaxed Structures and Formation Energies

① Stone-Wales (SW)
② B substitutional on graphene (B_{sub})
③ H substitutional on graphene (H_{sub})
④ O substitutional on graphene (O_{sub})
⑤ N substitutional on graphene (N_{sub})
⑥ N substitutional-vacancy on graphene (N_{sub-sv})
⑦ N adsorbed on graphene – bridge (N^{bg}_{ad})
⑧ B adsorbed on graphene – bridge (B^{bg}_{ad})
⑨ B adsorbed on graphene – top (B^{top}_{ad})
⑩ O adsorbed on graphene – bridge (O^{bg}_{ad})
⑪ H adsorbed on graphene – top (H^{top}_{ad})
⑫ H adsorbed on graphene – hollow (H^{ho}_{ad})
⑬ COOH adsorbed on graphene (COOH-G)
⑭ OH adsorbed on graphene (OH-G)

Figure A.1: List of additional defective graphene: stone wales, substitutional and adsorbed atoms.

Relaxed Structures
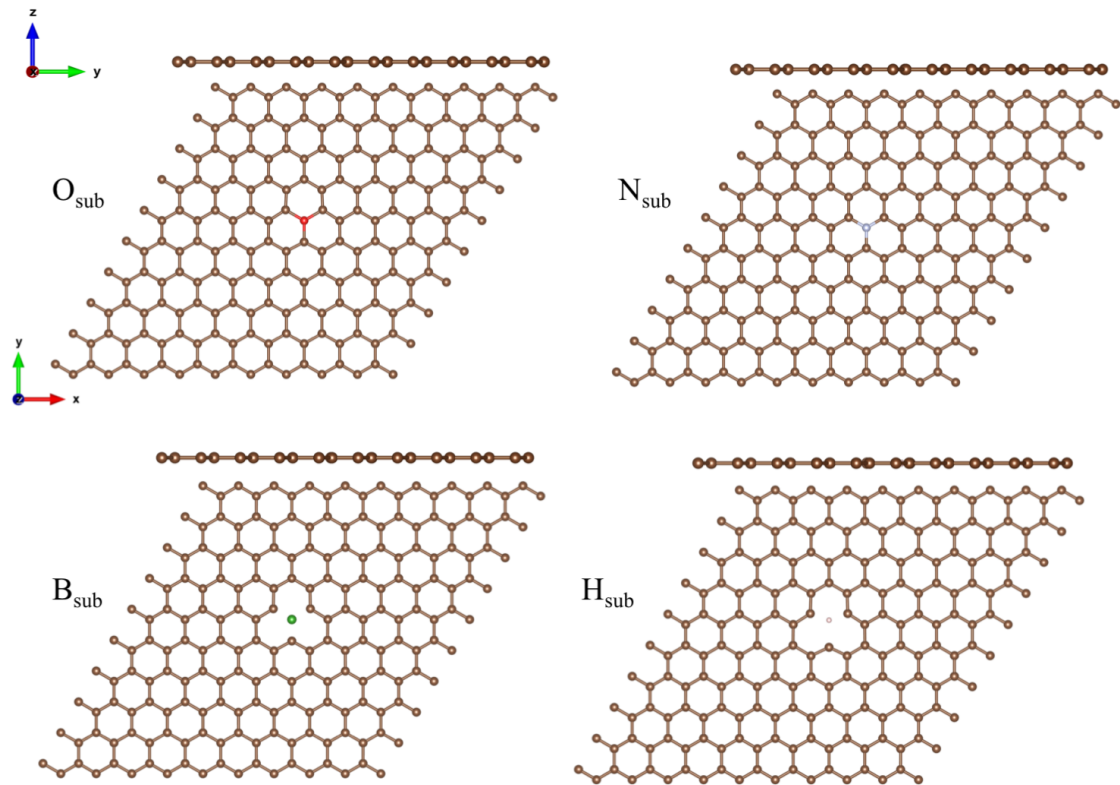
Figure A.2: Top and side views of relaxed substitutional defects on graphene. Only in-plane distortions are observed.
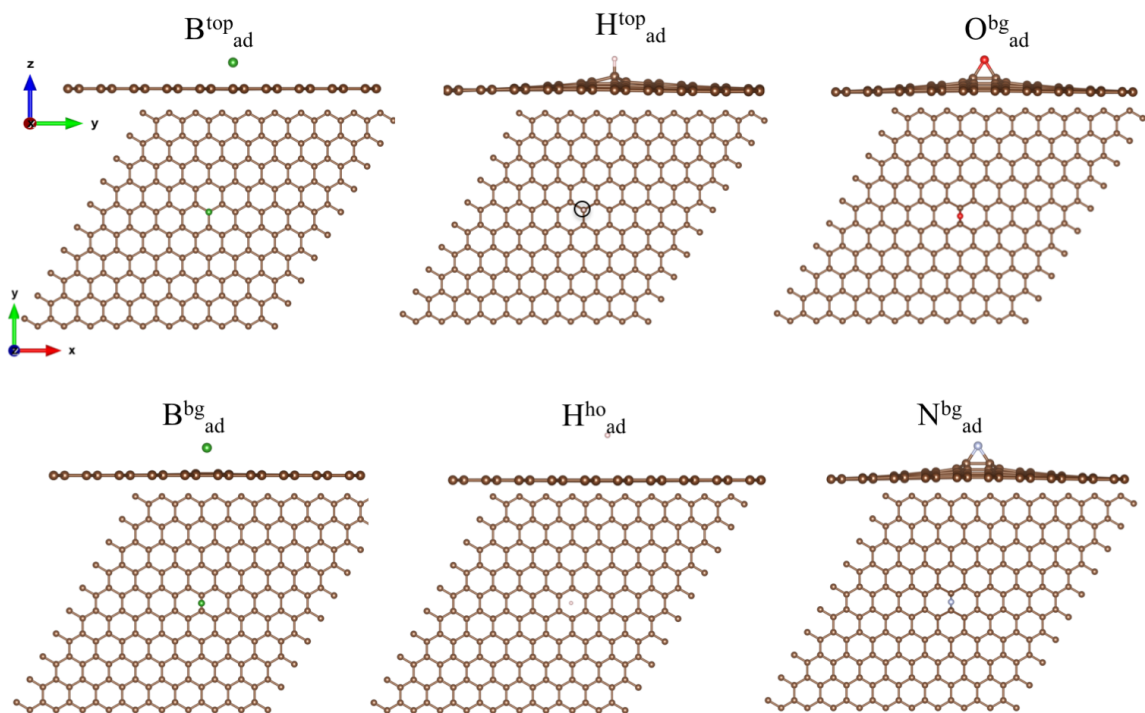
Figure A.3: Top and side views of adsorbed defects on graphene. In-plane and out-of-plane distortions are observed.
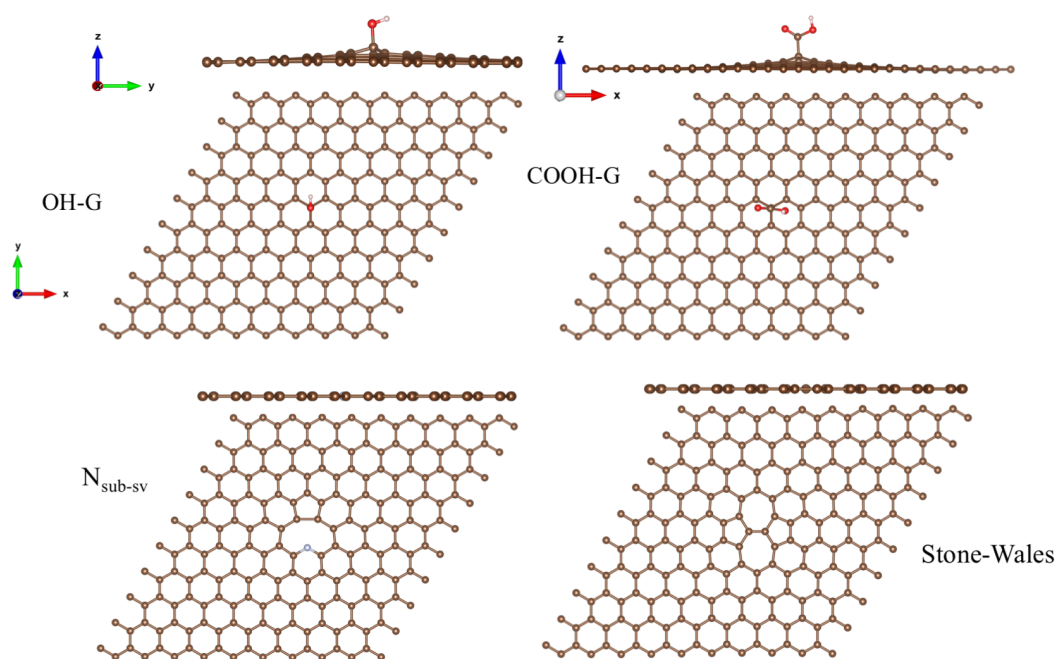
Figure A.4: Top and side views of hydroxyl (OH-G) and carboxyl (COOH-G) functionalized graphene, N substitutional on single-vacancy graphene and Stone Wales defect.

Formation Energies

System	Formation energy (eV)	Formation energy (kcal/mol)	Formation energy (kJ/mol)
N_{Sub}	-7.22	-166.50	-696.62
B_{Sub}	-5.57	-128.45	-537.42
O^{bg}_{ad}	-3.78	-87.17	-364.71
N^{bg}_{ad}	-3.69	-85.09	-356.03
N_{sub-sv}	-2.74	-63.19	-264.37
H^{top}_{ad}	-1.90	-43.82	-183.32
O_{Sub}	-1.74	-40.13	-167.88
OH-G	-1.38	-31.82	-133.15
B^{bg}_{ad}	-1.14	-26.29	-109.99
B^{top}_{ad}	-1.08	-24.91	-104.20
COOH-G	-0.44	-10.15	-42.45
H^{ho}_{ad}	-0.29	-6.69	-27.98
H_{Sub}	4.45	102.62	429.36
SW	4.89	112.77	471.81

Figure A.5: Formation energies arranged in descending order of energetic stability.

A.2 NEXAFS Fingerprints

Adsorbed Systems
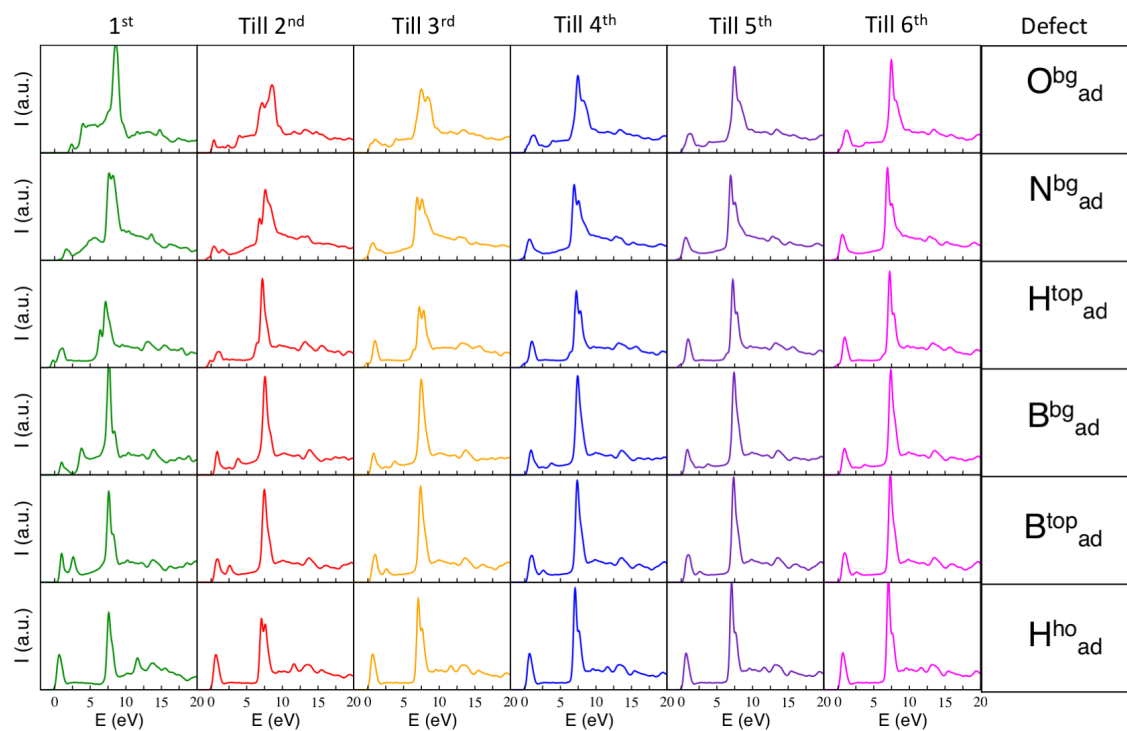
Figure A.6: Progression of distinctive NEXAFS spectra of adsorbed atoms on graphene for every ROI projected at incident angle of 55° incident angle.

Substitutional Systems
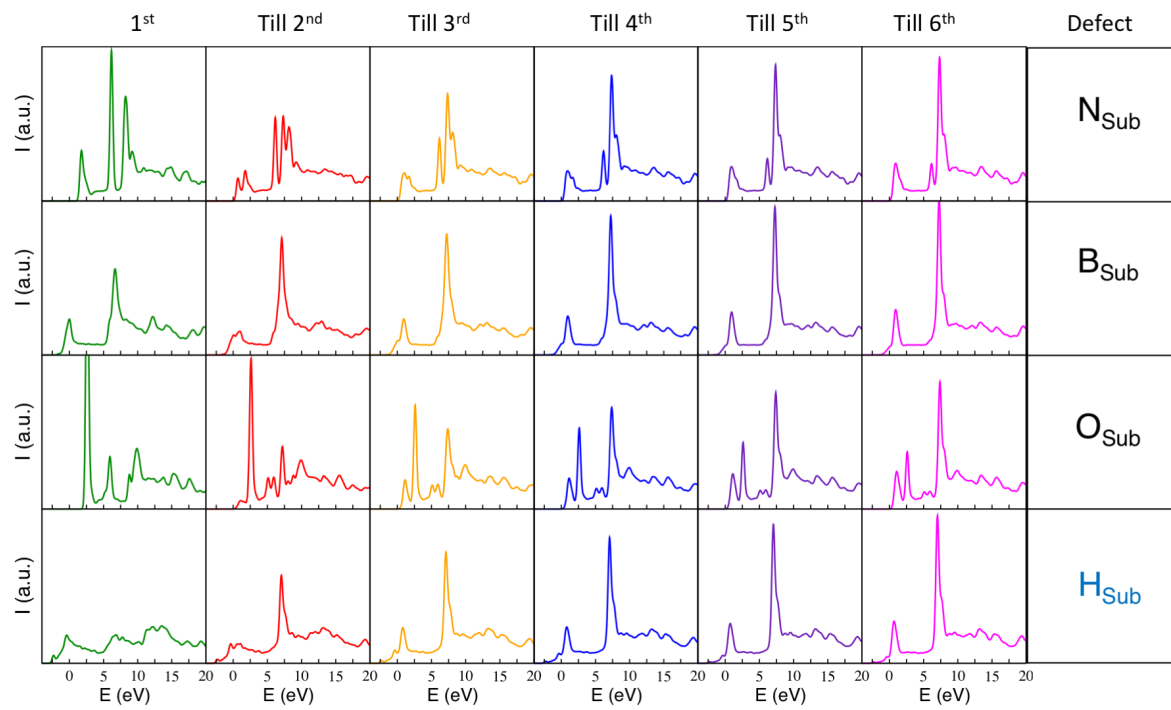
Figure A.7: Progression of distinctive NEXAFS spectra of substitutional atoms on graphene for every ROI projected at incident angle of 55° incident angle.

Other Systems
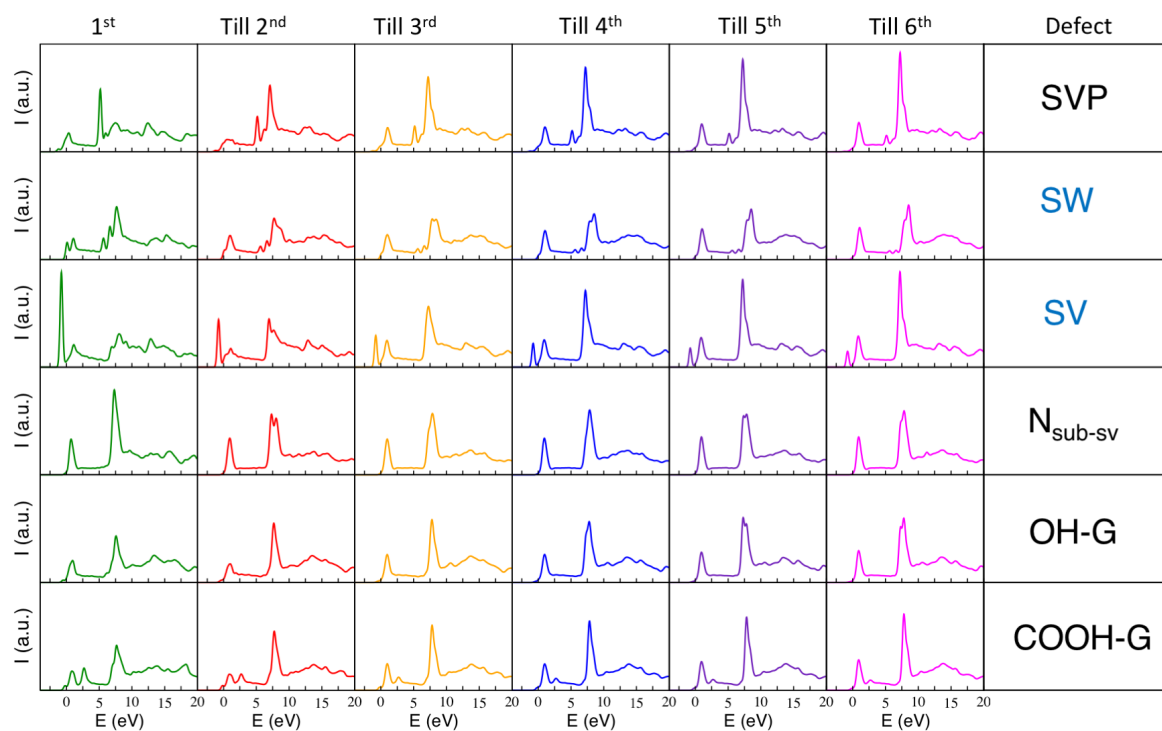
Figure A.8: Progression of distinctive NEXAFS spectra of single vacancy decorated with passivated (SVP), Stone Wales, single vacancy (SV), N substitutional on SV, hydroxyl and carboxyl adsorbed on graphene for every ROI projected at incident angle of 55° incident angle.

K-edge of adsorbed/substituted atoms
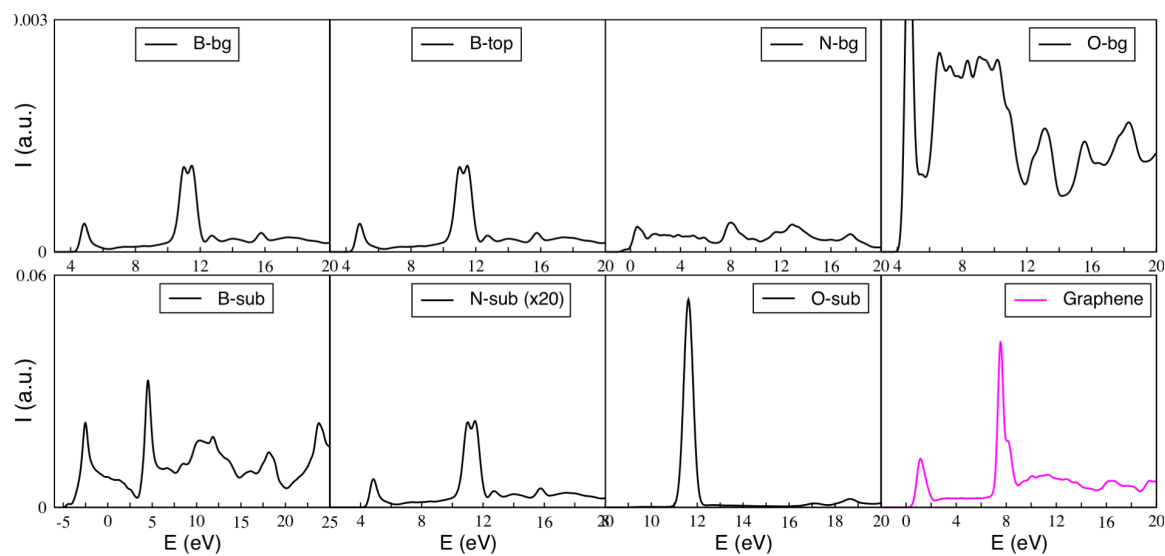
Figure A.9: K-edge NEXAFS spectra of adsorbed and substitutional atoms and pristine graphene (in magenta) projected at incident angle of 55° incident angle.

DMSO-Graphene Interaction for Biological Applications by NEXAFS

B.1   Relaxed Structures and Adsorption Energies

Relaxed Structures: without vdW
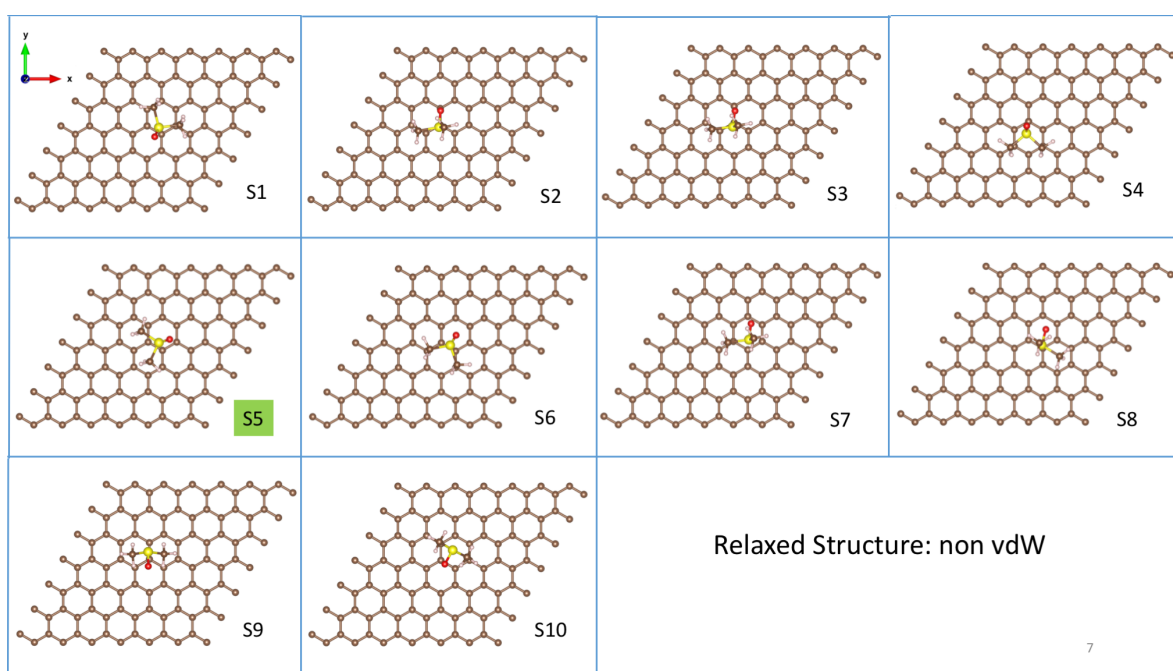
Figure B.1: Top view of relaxed structures of ten different conformation of DMSO on graphene without van der Waals. S5 is the most stable configuration.
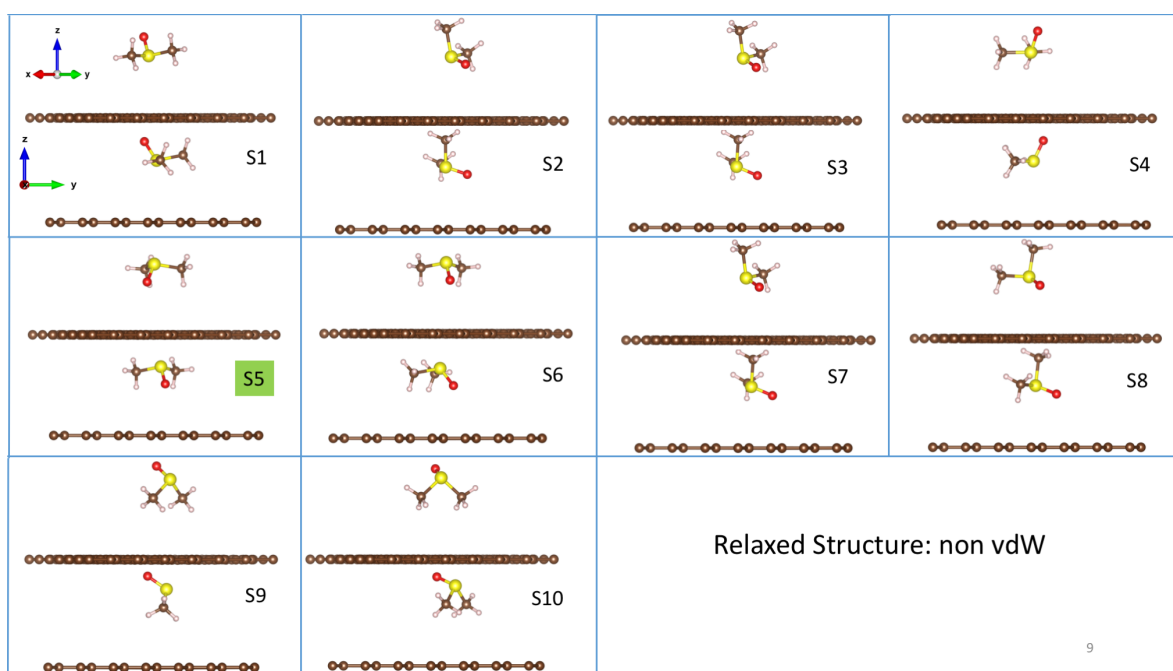
Figure B.2: Two side views of relaxed structures of ten different conformation of DMSO on graphene without van der Waals. S5 is the most stable configuration.

Relaxed Structures: with vdW
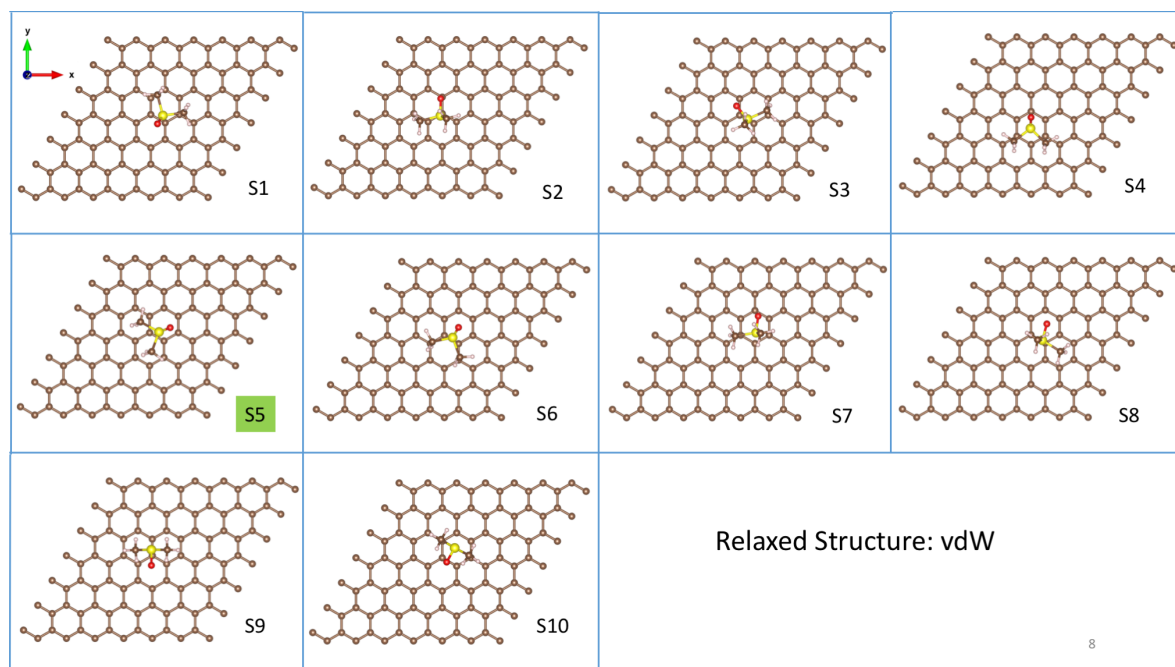
Figure B.3: Top view of relaxed structures of ten different conformation of DMSO on graphene including van der Waals. S5 is the most stable configuration.
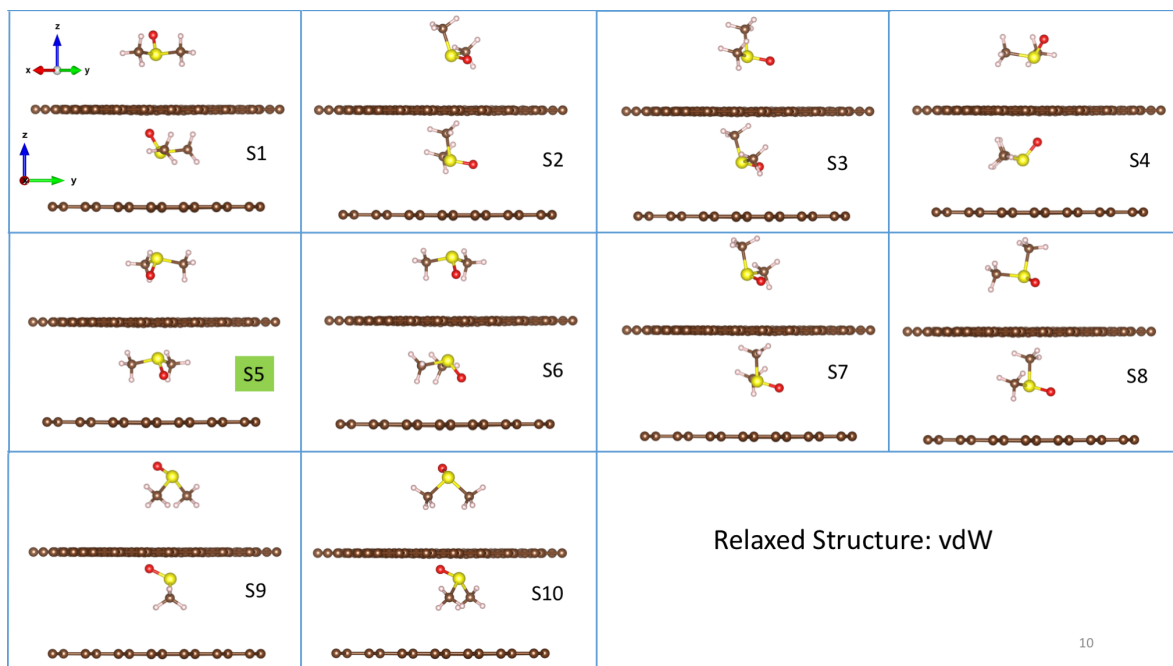
Figure B.4: Two side views of relaxed structures of ten different conformation scenarios of DMSO on graphene including van der Waals. S5 is the most stable configuration.

Adsorption Energies

System	Adsorption Energy (E_{ad}) (meV)	
	non-vdW	vdW
S1	-25.50	-352.75
S2	-36.54	-347.08
S3	-37.05	-344.96
S4	-26.57	-365.84
S5	-44.71	-395.62
S6	-44.30	-391.02
S7	-36.65	-342.93
S8	-39.01	-350.88
S9	-20.00	-319.69
S10	-20.67	-316.68

Figure B.5: Adsorption energies of ten DMSO-graphene systems. S5 is the most stable configuration.

B.2 NEXAFS simulations
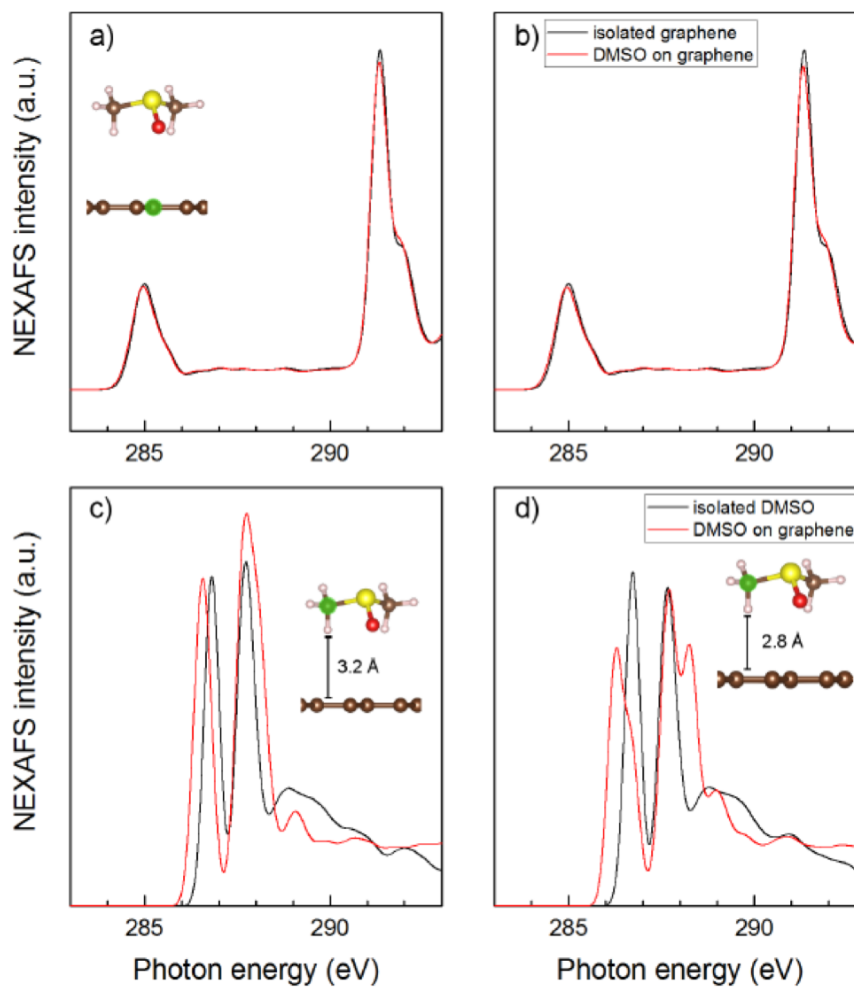
Figure B.6: (a) and (b) are NEXAFS spectra of an absorbing carbon atom of graphene, without and with van der Waals, respectively. (c) and (d) are NEXAFS spectra of an absorbing carbon atom from DMSO, without and with van der Waals, respectively.

Differential Electronic Density $\left(\rho_e^{Diff}\right)$

S5 ρ_e^{Tot} ρ_e^{Diff}

I = 0.0315606

I = 0.0869934

I: Isovalue $\left[\frac{a.u.}{Bohr^3}\right]$

S5   Van der Waals   I = 0.0311256

I = 0.0876208
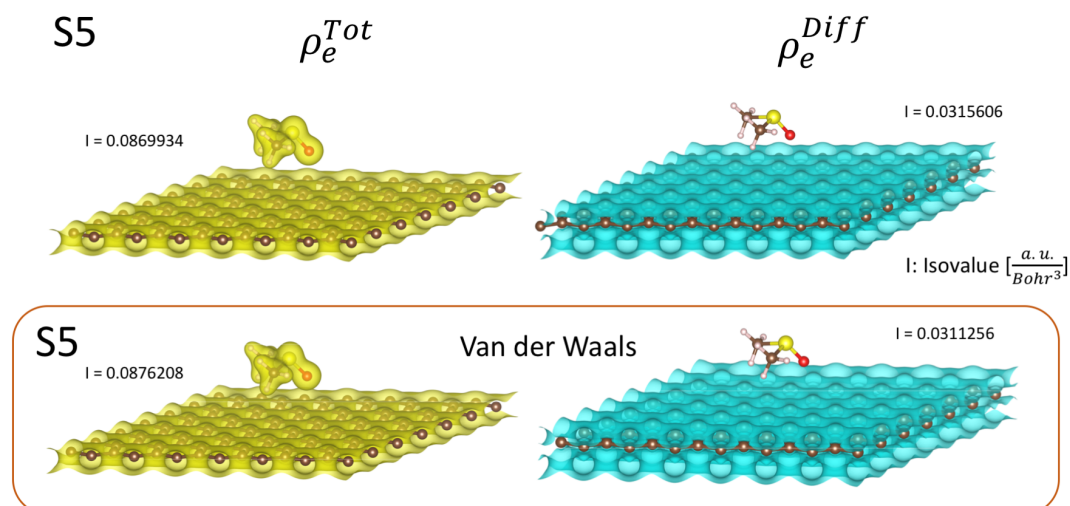
Figure B.7: Total electron density (left) and difference in electronic density (right) isosurfaces of the most stable DMSO-graphene system (S5), with and without van der Waals. Yellow and cyan represent electronic accumulation and depletion, respectively.

C

List of Presentations, Courses and Workshops

Presentations

- *Monitoring Deformation in Graphene Through Hyperspectral Synchrotron Spectroscopy to inform Fabrication*. **Materials Research Society Fall Meeting & Exhibit, 2017, Boston, USA**. [Poster]

- *Strain and bond length dynamics upon growth and transfer of graphene by NEXAFS spectroscopy from first principles and experiment*. **Materials Research Society Fall Meeting & Exhibit, 2017, Boston, USA**. [Poster]

- *Simulations of NEXAFS to study processing effects on Graphene*. **Ninth York Doctoral Symposium on Computer Science & Electronics, University of York, 2016, York, UK**. [Poster]

- *X-ray Absorption Spectroscopy study of processing effects on Graphene: Experiment and Theory*. **Molecular Foundry User Meeting, Lawrence Berkeley National Laboratory, 2016, California, USA**. [Poster]

- *Spin-dependent transport on graphene nanoribbons*. **Summer International Scientific Meeting, National University of Engineering, 2016, Lima, Peru**. [Oral]

- *Simulating Spin-Orbit scattering in nanoscopic systems: the case of graphene nanoribbons*. **Summer Physics Colloquium, National University of San Marcos, 2016, Lima, Peru**. [Oral]

- *First Principles prediction of Near Edge X-ray Absorption Fine Structure from graphene: effects of synthesis and processing.* **Workshop density functional theory and beyond, Fritz-Haber-Institute of the Max Planck Society, 2015, Berlin, Germany**. [Poster]

- *Polymer nanocomposites for structural and smart applications.* **HPCWales-Fujitsu Studentship Meeting, 2014, Gregynog Hall, UK**. [Oral]

- *Electronic Transport Properties of Graphene Nanoribbons under Spin-Orbit Coupling.* **Summer school of materials modelling and world class science communication, 2014, London, UK**. [Poster]

Courses and Workshops

- *Machine Learning with Python for Materials Research BOOTCAM & WORKSHOP.* **University of Maryland, 2017, College Park, USA**.

- *Simulations for the Experimentalist and the Industrialist.* **Diamond Light Source, 2016, Oxfordshire, UK**.

- *Hands-on workshop density functional theory and beyond: Fist-principles simulations of molecules and materials.* **Fritz-Haber-Institute of the Max Planck Society, 2015, Berlin, Germany**.

- *Latinos in the Mathematical Sciences.* **Institute for Pure and Applied Mathematics, 2015, University of California Los Angeles, California, USA**.

- *Training session on calculations of NEXAFS from first-principles.* **Molecular Foundry, Lawrence Berkeley National Laboratory, 2014, California, USA**.

- *Linearized Muffin-Tin Orbitals/Quasi-particle Self-consistent GW Hands On Course - Science & Technology Facilities Council.* **Daresbury Laboratory, 2014, Daresbury, UK**.

Symposium Assistant

- Symposium WW:*Materials by Design-Merging Advanced In-Situ Characterization with Predictive Simulation* and Tutorial WW:*An Introduction to Materials Simulations*. Lead organizer: Dr. Eva Campo. **2014 MRS Spring Meeting, San Francisco, USA**.

D

Research Visits and Mentoring

Research Visits

- *DBSCAN applied to soft X-ray hyperspectral NEXAFS images*. Host: Dr. Apurva Mehta. **SLAC National Accelerator Laboratory, 2016, California, USA**.

- *Modelling of X-ray absorption spectroscopy*. Host: Dr. David Prendergast. **Molecular Foundry, Lawrence Berkeley National Laboratory, 2014/2015/2016, California, USA**.

- *Data acquisition of NEXAFS spectra*. **National Synchrotron Light Source (NSLS), Brookhaven National Laboratory, 2014, New York, USA**.

Mentoring

- *Atomistic simulations of structural and electronics properties of Dimethyl Sulfoxide adsorbed on graphene*.Undergraduate final project of Erik Drescher. **School of Electronic Engineering, Bangor University, 2016, Bangor, UK**.

- *DMSO on graphene - geometry optimization with GAMESS and Quantum Espresso*. Work experience of Dafydd Gwyn from High School Ysgol y Creuddyn, Llandudno, Wales. **School of Electronic Engineering, Bangor University, 2015, Bangor, UK**.

Bibliography

[1] P. R. Wallace, "The band theory of graphite," *Phys. Rev.* **71** (1947) 622–634.

[2] L. D. Landau, "Zur theorie der phasenumwandlungen ii. phys," *Z. Sowjetunion* **11** (1937) 26–35.

[3] R. E. Peierls, "Bemerkungen über umwandlungstemperaturen," *Helv. Phys.* **7** (1937) 81–83.

[4] K. S. Novoselov, A. K. Geim, S. V. Morozov, D. Jiang, Y. Zhang, S. V. Dubonos, I. Grigorieva, and A. Firsov, "Electric field effect in atomically thin carbon films," *Science* **306** no. 5696, (2004) 666–669.

[5] A. K. Geim and K. S. Novoselov, "The rise of graphene," *Nature Materials* **6** (2007) 183–191.

[6] R. Roldan, L. Chirolli, E. Prada, J. A. Silva-Guillen, P. San-Jose, and F. Guinea, "Theory of 2d crystals: graphene and beyond," *Chem. Soc. Rev.* **46** (2017) 4387–4399.

[7] P. Suvarnaphaet and S. Pechprasarn, "Graphene-based materials for biosensors: A review," *Sensors* **17** (2017) 2161.

[8] K. S. Novoselov, A. K. Geim, S. V. Morozov, D. Jiang, M. I. Katsnelson, I. V. Grigorieva, S. V. Dubonos, and A. A. Firsov, "Two-dimensional gas of massless dirac fermions in graphene," *Nature* **438** (2005) 197–200.

[9] K. S. Novoselov, Z. Jiang, Y. Zhang, S. V. Morozov, H. L. Stormer, U. Zeitler, J. C. Maan, G. S. Boebinger, P. Kim, and A. K. Geim, "Room-temperature quantum hall effect in graphene," *Science* **315** no. 5817, (2007) 1379–1379.

[10] J. H. Chen, C. Jang, S. Xiao, M. Ishigami, and M. S. Fuhrer, "Intrinsic and extrinsic performance limits of graphene devices on sio$_2$," *Nanotechnology* **3** (2008) 206–209.

[11] S. V. Morozov, K. S. Novoselov, M. I. Katsnelson, F. Schedin, D. C. Elias, J. A. Jaszczak, and A. K. Geim, "Giant intrinsic carrier mobilities in graphene and its bilayer," *Phys. Rev. Lett.* **100** (2008) 016602.

[12] A. Itoh and H. Matsunami, "Single crystal growth of sic and electronic devices," *Critical Reviews in Solid State and Materials Sciences* **22** no. 2, (1997) 111–197.

[13] J. Jobst, D. Waldmann, F. Speck, R. Hirner, D. K. Maude, T. Seyller, and H. B. Weber, "Quantum oscillations and quantum hall effect in epitaxial graphene," *Phys. Rev. B* **81** (2010) 195434.

[14] C. Lee, X. Wei, J. W. Kysar, and J. Hone, "Measurement of the elastic properties and intrinsic strength of monolayer graphene," *Science* **321** no. 5887, (2008) 385–388.

[15] R. R. Nair, P. Blake, A. N. Grigorenko, K. S. Novoselov, T. J. Booth, T. Stauber, N. M. R. Peres, and A. K. Geim, "Fine structure constant defines visual transparency of graphene," *Science* **320** no. 5881, (2008) 1308–1308.

[16] A. A. Balandin, S. Ghosh, W. Bao, I. Calizo, D. Teweldebrhan, F. Miao, and C. N. Lau, "Superior thermal conductivity of single-layer graphene," *Nano Letters* **8** no. 3, (2008) 902–907.

[17] V. Berry, "Impermeability of graphene and its applications," *Carbon* **62** (2013) 1–10.

[18] J. Liu, J. Tang, and J. J. Gooding, "Strategies for chemical modification of graphene and applications of chemically modified graphene," *J. Mater. Chem.* **22** (2012) 12435–12452.

[19] M. Chen, R. C. Haddon, R. Yan, and E. Bekyarova, "Advances in transferring chemical vapour deposition graphene: a review," *Mater. Horiz.* **4** (2017) 1054–1063.

[20] A. Ciesielski and P. Samori, "Graphene via sonication assisted liquid-phase exfoliation," *Chem. Soc. Rev.* **43** (2014) 381–398.

[21] K. R. Paton, E. Varrla, C. Backes, R. J. Smith, U. Khan, A. O'Neill, C. Boland, M. Lotya, O. M. Istrate, P. King, T. Higgins, S. Barwich, P. May, P. Puczkarski, I. Ahmed, M. Moebius, H. Pettersson, E. Long, J. Coelho, S. E. O'Brien, E. K. McGuire, B. M. Sanchez, G. S. Duesberg, N. McEvoy, T. J. Pennycook, C. Downing, A. Crossley, V. Nicolosi, and J. N. Coleman, "Scalable production of large quantities of defect-free few-layer graphene by shear exfoliation in liquids," *Nature Materials* **13** (2014) 624.

[22] I. Y. Jeon, S. Y. Bae, J. M. Seo, and J. B. Baek, "Scalable production of edge-functionalized graphene nanoplatelets via mechanochemical ball-milling," *Advanced Functional Materials* **25** no. 45, (2015) 6961–6975.

[23] J. N. Coleman, M. Lotya, A. O'Neill, S. D. Bergin, P. J. King, U. Khan, K. Young, A. Gaucher, S. De, R. J. Smith, I. V. Shvets, S. K. Arora, G. Stanton, H. Y. Kim, K. Lee, G. T. Kim, G. S. Duesberg, T. Hallam, J. J. Boland, J. J. Wang, J. F. Donegan, J. C. Grunlan, G. Moriarty, A. Shmeliov, R. J. Nicholls, J. M. Perkins, E. M. Grieveson, K. Theuwissen, D. W. McComb, P. D. Nellist, and V. Nicolosi, "Two-dimensional nanosheets produced by liquid exfoliation of layered materials," *Science* **331** no. 6017, (2011) 568–571.

[24] Y. Zhu, H. Ji, H. M. Cheng, and R. S. Ruoff, "Mass production and industrial applications of graphene materials," *National Science Review* **5** (2018) 90–101.

[25] K. Krishnamoorthy, M. Veerapandian, K. Yun, and S. J. Kim, "The chemical and structural analysis of graphene oxide with different degrees of oxidation," *Carbon* **53** (2013) 38–49.

[26] G. Eda and M. Chhowalla, "Chemically derived graphene oxide: Towards large-area thin-film electronics and optoelectronics," *Advanced Materials* **22** no. 22, 2392–2415.

[27] X. Li, W. Cai, J. An, S. Kim, J. Nah, D. Yang, R. Piner, A. Velamakanni, I. Jung, E. Tutuc, S. K. Banerjee, L. Colombo, and R. S. Ruoff, "Large-area synthesis of high-quality and uniform graphene films on copper foils," *Science* **324** no. 5932, (2009) 1312–1314.

[28] S. Bae, H. Kim, Y. Lee, X. Xu, J. S. Park, Y. Zheng, J. Balakrishnan, T. Lei, H. R. Kim, and Y. I. Song, "Roll-to-roll production of 30-inch graphene films for transparent electrodes," *Nature nanotechnology* **5** no. 8, (2010) 574–578.

[29] K. V. Emtsev, A. Bostwick, K. Horn, J. Jobst, G. L. Kellogg, L. Ley, J. L. McChesney, T. Ohta, S. A. Reshanov, J. R´ohrl, E. Rotenberg, A. K. Schmid, D. Waldmann, H. B. Weber, and T. Seyller, "Towards wafer-size graphene layers by atmospheric pressure graphitization of silicon carbide," *Nature Materials* **8** (2009) 203.

[30] W. Norimatsu and M. Kusunoki, "Epitaxial graphene on sic 0001: advances and perspectives," *Physical Chemistry Chemical Physics* **16** no. 8, (2014) 3501–3511.

[31] F. Schwierz, "Graphene transistors," *Nature nanotechnology* **5** no. 7, (2010) 487–496.

[32] J. N. Coleman, "Liquid exfoliation of defect-free graphene," *Accounts of Chemical Research* **46** no. 1, (2013) 14–22.

[33] D. Li, W. Zhang, X. Yu, Z. Wang, Z. Su, and G. Wei, "When biomolecules meet graphene: from molecular level interactions to material design and applications," *Nanoscale* **8** (2016) 19491–19509.

[34] C. Mattevi, G. Eda, S. Agnoli, S. Miller, K. A. Mkhoyan, O. Celik, D. Mastrogiovanni, G. Granozzi, E. Garfunkel, and M. Chhowalla, "Evolution of electrical, chemical, and structural properties of transparent and conducting chemically derived graphene thin films," *Advanced Functional Materials* **19** no. 16, 2577–2583.

[35] https://www.graphenesq.com.

[36] S. Gorantla, A. Bachmatiuk, J. Hwang, H. A. Alsalman, J. Y. Kwak, T. Seyller, J. Eckert, M. G. Spencer, and M. H. Rummeli, "A universal transfer route for graphene," *Nanoscale* **6** (2014) 889–896.

[37] Y. C. Lin, C. C. Lu, C. H. Yeh, C. Jin, K. Suenaga, and P. W. Chiu, "Graphene annealing: How clean can it be?," *Nano Letters* **12** no. 1, (2012) 414–419.

[38] H. Park, P. R. Brown, V. Bulovi, and J. Kong, "Graphene as transparent conducting electrodes in organic photovoltaics: Studies in graphene morphology, hole transporting layers, and counter electrodes," *Nano Letters* **12** no. 1, (2012) 133–140.

[39] Y. Jia, X. Gong, P. Peng, Z. Wang, Z. Tian, L. Ren, Y. Fu, and H. Zhang, "Toward high carrier mobility and low contact resistance: Laser cleaning of pmma residues on graphene surfaces," *Nano-Micro Letters* **8** no. 4, (2016) 336–346.

[40] J. Sun, H. O. Finklea, and Y. Liu, "Characterization and electrolytic cleaning of poly(methyl methacrylate) residues on transferred chemical vapor deposited graphene," *Nanotechnology* **28** no. 12, (2017) 125703.

[41] X. Liang, B. A. Sperling, I. Calizo, G. Cheng, C. A. Hacker, Q. Zhang, Y. Obeng, K. Yan, H. Peng, Q. Li, X. Zhu, H. Yuan, A. R. Hight Walker, Z. Liu, L. m. Peng, and C. A. Richter, "Toward clean and crackless transfer of graphene," *ACS Nano* **5** no. 11, (2011) 9144–9153.

[42] X. D. Chen, Z. B. Liu, C. Y. Zheng, F. Xing, X. Q. Yan, Y. Chen, and J. G. Tian, "High-quality and efficient transfer of large-area graphene films onto different substrates," *Carbon* **56** (2013) 271 – 278.

[43] J. Kang, S. Hwang, J. H. Kim, M. H. Kim, J. Ryu, S. J. Seo, B. H. Hong, M. K. Kim, and J. B. Choi, "Efficient transfer of large-area graphene films onto rigid substrates by hot pressing," *ACS Nano* **6** no. 6, (2012) 5360–5365.

[44] M. Chen, D. Stekovic, W. Li, B. Arkook, R. C. Haddon, and E. Bekyarova, "Sublimation-assisted graphene transfer technique based on small polyaromatic hydrocarbons," *Nanotechnology* **28** no. 25, (2017) 255701.

[45] R. Stumm von Bordwehr, "A history of x-ray absorption fine structure," *Ann. Phys. Fr.* **14** no. 4, (1989) 377–465.

[46] F. de Groot, "High-resolution x-ray emission and x-ray absorption spectroscopy," *Chemical Reviews* **101** no. 6, (2001) 1779–1808.

[47] M. Simon and T. Schmitt, "Progress in resonant inelastic x-ray scattering," *Journal of Electron Spectroscopy and Related Phenomena* **188** (2013) 1–2.

[48] J. Fink, E. Schierle, E. Weschke, and J. Geck, "Resonant elastic soft x-ray scattering," *Reports on Progress in Physics* **76** no. 5, (2013) 056502.

[49] F. Pulizzi, "Electron and x-ray microscopy," *Nature Materials* **8** no. 5, (2009) 0259.

[50] A. Damascelli, Z. Hussain, and Z. X. Shen, "Angle-resolved photoemission studies of the cuprate superconductors," *Rev. Mod. Phys.* **75** 473–541.

[51] J. H. Hubbell, H. A. Gimm, and I. O/verbo/, "Pair, triplet, and total atomic cross sections (and mass attenuation coefficients) for 1 mev-100 gev photons in elements z=1 to 100," *Journal of Physical and Chemical Reference Data* **9** no. 4, (1980) 1023–1148.

[52] F. Alves Lima, *Investigation of Physiological Solutions of Metalloproteins in a High-Repetition Rate Picosecond X-ray Absorption Experiment*. PhD thesis, Lausanne, 2011.

[53] J. Als-Nielsen and D. McMorrow, *Elements of Modern X-ray Physics*. John Wiley & Sons, 2 ed., 2011.

[54] N. A. Besley and F. A. Asmuruf, "Time-dependent density functional theory calculations of the spectroscopy of core electrons," *Phys. Chem. Chem. Phys.* **12** (2010) 12024–12039.

[55] `https://lightsources.org/lightsources-of-the-world/`.

[56] D. M. Mills, J. R. Helliwell, Å. Kvick, T. Ohta, I. A. Robinson, and A. Authier, "Report of the Working Group on Synchrotron Radiation Nomenclature – brightness, spectral brightness or brilliance?," *Journal of Synchrotron Radiation* **12** no. 3, (2005) 385.

[57] S. Mobilio and A. Balerna, "Introduction to the main properties of synchrotron radiation," *Conference Proceedings-Italian Physical Society* **82** (1999-2003) 1–24.

[58] `http://physicsbuzz.physicscentral.com/2013/05/podcast-sesame.html`.

[59] `https://www.mgi.gov`.

[60] `http://www.prolibraries.com/mrs/?select=new_sessionlist&conferenceID=8&packageID=96`.

[61] M. L. Green, C. L. Choi, J. R. Hattrick-Simpers, A. M. Joshi, I. Takeuchi, S. C. Barron, E. Campo, T. Chiang, S. Empedocles, J. M. Gregoire, A. G. Kusne, J. Martin, A. Mehta, K. Persson, Z. Trautt, J. V. Duren, and A. Zakutayev, "Fulfilling the promise of the materials genome initiative with high-throughput experimental methodologies," *Applied Physics Reviews* **4** no. 1, (2017) 011105.

[62] E. M. Campo, "Education and dissemination: Lab-to-market-to-classroom," *MRS Proceedings* **1583** (2013) mrss13–1583–eee04–09.

[63] C. J. Long, J. Hattrick Simpers, M. Murakami, R. C. Srivastava, I. Takeuchi, V. L. Karen, and X. Li, "Rapid structural mapping of ternary metallic alloy systems using the combinatorial approach and cluster analysis," *Review of Scientific Instruments* **78** no. 7, (2007) 072217.

[64] G. Hautier, C. C. Fischer, A. Jain, T. Mueller, and G. Ceder, "Finding nature's missing ternary oxide compounds using machine learning and density functional theory," *Chemistry of Materials* **22** no. 12, (2010) 3762–3767.

[65] K. Hansen, G. Montavon, F. Biegler, S. Fazli, M. Rupp, M. Scheffler, O. A. von Lilienfeld, A. Tkatchenko, and K. R. Müller, "Assessment and validation of machine learning methods for predicting molecular atomization energies," *Journal of Chemical Theory and Computation* **9** no. 8, (2013) 3404–3419.

[66] V. Botu and R. Ramprasad, "Learning scheme to predict atomic forces and accelerate materials simulations," *Phys. Rev. B* **92** (2015) 094306.

[67] K. T. Butler, D. W. Davies, H. Cartwright, O. Isayev, and A. Walsh, "Machine learning for molecular and materials science," *Nature* **559** (2018) 547–555.

[68] T. Mueller, A. G. Kusne, and R. Ramprasad, *Reviews in Computational Chemistry*. Wiley-Blackwell, 1 ed., 2016.

[69] M. Ester, H.-P. Kriegel, J. Sander, and X. Xu, "A density-based algorithm for discovering clusters in large spatial databases with noise," in *Kdd*, vol. 96, pp. 226–231.

[70] E. Merzbacher, *Quantum mechanics; 2nd ed.* Wiley, New York, NY, 1998.

[71] M. Born and R. Oppenheimer, "Zur quantentheorie der molekeln," *Annalen der Physik* **389** no. 20, (1927) 457–484.

[72] P. Hohenberg and W. Kohn, "Inhomogeneous electron gas," *Phys. Rev.* **136** (1964) B864–B871.

[73] W. Kohn and L. J. Sham, "Self-consistent equations including exchange and correlation effects," *Phys. Rev.* **140** (1965) A1133–A1138.

[74] J. C. Slater, "The theory of complex spectra," *Phys. Rev.* **34** (1929) 1293–1322.

[75] R. G. Parr and Y. Weitao, *Density-Functional Theory of Atoms and Molecules*. Oxford University Press, 1994.

[76] J. P. Perdew, "Density-functional approximation for the correlation energy of the inhomogeneous electron gas," *Phys. Rev. B* **33** (1986) 8822–8824.

[77] P. M. W. Gill and P. F. Loos, "Uniform electron gases," *Theoretical Chemistry Accounts* **131** (2011) 1–9.

[78] D. M. Ceperley and B. J. Alder, "Ground state of the electron gas by a stochastic method," *Phys. Rev. Lett.* **45** (1980) 566–569.

[79] R. M. Martin, *Electronic Structure: Basic Theory and Practical Methods (Vol 1)*. Cambridge University Press, 2004.

[80] J. C. Phillips and L. Kleinman, "New method for calculating wave functions in crystals and molecules," *Phys. Rev.* **116** (1959) 287–294.

[81] B. Bransden and C. Joachain, *Quantum Mechanics*.

[82] D. Griffiths, *Introduction to Quantum Mechanics*.

[83] G. D. Mahan, *Physics of Solids and Liquids, Many Particle Physics*. Springer US, 3 ed., 2000.

[84] W. Hua, *Structure and spectroscopy of bio- and nano-materials from first-principles simulations*. PhD thesis, KTH, Theoretical Chemistry, 2011. QC 20110404.

[85] J. Stöhr, *NEXAFS Spectroscopy*. Springer, 2003.

[86] D. Prendergast and G. Galli, "X-ray absorption spectra of water from first principles calculations," *Physical review letters* **96** no. 21, (2006) 215502.

[87] P. E. Blöchl, "Projector augmented-wave method," *Phys. Rev. B* **50** (1994) 17953–17979.

[88] B. Hetényi, F. De Angelis, P. Giannozzi, and R. Car, "Calculation of near-edge x-ray-absorption fine structure at finite temperatures: Spectral signatures of hydrogen bond breaking in liquid water," *The Journal of Chemical Physics* **120** no. 18, (2004) 8632–8637.

[89] M. Taillefumier, D. Cabaret, A. M. Flank, and F. Mauri, "X-ray absorption near-edge structure calculations with the pseudopotentials: Application to the k edge in diamond and α-quartz," *Phys. Rev. B* **66** (2002) 195107.

[90] L. X. Benedict and E. L. Shirley, "Ab initio calculation of $\epsilon_2(\omega)$ including the electron-hole interaction: Application to gan and $\mathrm{caf_2}$," *Phys. Rev. B* **59** (1999) 5441–5451.

[91] E. L. Shirley, "Optimal basis sets for detailed brillouin-zone integrations," *Phys. Rev. B* **54** (1996) 16464–16469.

[92] W. Y. Rojas, A. D. Winter, J. Grote, S. S. Kim, R. R. Naik, A. D. Williams, C. Weiland, E. Principe, D. A. Fischer, S. Banerjee, D. Prendergast, and E. M. Campo, "Strain and bond length dynamics upon growth and transfer of graphene by nexafs spectroscopy from first-principles and experiment," *Langmuir* **34** no. 4, (2018) 1783–1794.

[93] `http://portal.hpcwales.co.uk/docs/userguide/toc.html`.

[94] `https://sites.google.com/a/lbl.gov/high-performance-computing-services-group/lbnl-supercluster/vulcan`.

[95] `https://sites.google.com/a/lbl.gov/high-performance-computing-services-group/lbnl-supercluster/etna`.

[96] `https://sites.google.com/a/lbl.gov/hpc/home`.

[97] `https://sites.google.com/a/lbl.gov/high-performance-computing-services-group/system/app/pages/subPages?path=/lbnl-supercluster`.

[98] S. S. Kim, Z. Kuang, Y. H. Ngo, B. L. Farmer, and R. R. Naik, "Biotic-abiotic interactions: Factors that influence peptide-graphene interactions," *ACS Applied Materials & Interfaces* **7** no. 36, (2015) 20447–20453.

[99] M. P. Seah and W. A. Dench, "Quantitative electron spectroscopy of surfaces: A standard data base for electron inelastic mean free paths in solids," *Surface and interface analysis* **1** no. 1, (1979) 2–11.

[100] J. Genzer, E. J. Kramer, and D. A. Fischer, "Accounting for auger yield energy loss for improved determination of molecular orientation using soft x-ray absorption spectroscopy," *Journal of applied physics* **92** no. 12, (2002) 7070–7079.

[101] P. Kruit and F. Read, "Magnetic field paralleliser for 2 electron-spectrometer and electron-image magnifier," *Journal of Physics E: Scientific Instruments* **16** no. 4, (1983) 313.

[102] G. Beamson, H. Porter, and D. Turner, "The collimating and magnifying properties of a superconducting field photoelectron spectrometer," *Journal of Physics E: Scientific Instruments* **13** no. 1, (1980) 64.

[103] G. Beamson, H. Porter, and D. Turner, "Photoelectron spectromicroscopy," *Nature* **290** (1981) 556–561.

147

[104] A. Konicek, C. Jaye, M. Hamilton, W. Sawyer, D. Fischer, and R. Carpick, "Near-edge x-ray absorption fine structure imaging of spherical and flat counterfaces of ultrananocrystalline diamond tribological contacts: A correlation of surface chemistry and friction," *Tribology Letters* **44** no. 1, (2011) 99–106.

[105] F. Bonaccorso, Z. Sun, T. Hasan, and A. Ferrari, "Graphene photonics and optoelectronics," *Nature photonics* **4** no. 9, (2010) 611–622.

[106] K. S. Novoselov, A. K. Geim, S. V. Morozov, D. Jiang, Y. Zhang, S. V. Dubonos, I. V. Grigorieva, and A. A. Firsov, "Electric field effect in atomically thin carbon films," *Science* **306** no. 5696, (2004) 666–669.

[107] A. K. Sood, I. Lund, Y. R. Puri, H. Efstathiadis, P. Haldar, N. K. Dhar, J. Lewis, M. Dubey, E. Zakar, and P. Wijewarnasuriya, "Review of graphene technology and its applications for electronic devices,".

[108] Z. Sun, A. Martinez, and F. Wang, "Optical modulators with 2d layered materials," *Nature Photonics* **10** no. 4, (2016) 227–238.

[109] T. Nagatsuma, G. Ducournau, and C. C. Renaud, "Advances in terahertz communications accelerated by photonics," *Nature Photonics* **10** no. 6, (2016) 371–379.

[110] R. Won and F. Xia, "Flat talk," *Nature Photonics* **10** no. 4, (2016) 205–206.

[111] H. Tetlow, J. P. De Boer, I. Ford, D. Vvedensky, J. Coraux, and L. Kantorovich, "Growth of epitaxial graphene: Theory and experiment," *Physics Reports* **542** no. 3, (2014) 195–295.

[112] B. J. Schultz, C. J. Patridge, V. Lee, C. Jaye, P. S. Lysaght, C. Smith, J. Barnett, D. A. Fischer, D. Prendergast, and S. Banerjee, "Imaging local electronic corrugations and doped regions in graphene," *Nature communications* **2** (2011) 372.

[113] A. Zurutuza and C. Marinelli, "Challenges and opportunities in graphene commercialization," *Nature nanotechnology* **9** no. 10, (2014) 730–734.

[114] M. Katsnelson and A. Geim, "Electron scattering on microscopic corrugations in graphene," *Philosophical Transactions of the Royal Society of London A: Mathematical, Physical and Engineering Sciences* **366** no. 1863, (2008) 195–204.

[115] H. Hattab, A. T. NDiaye, D. Wall, C. Klein, G. Jnawali, J. Coraux, C. Busse, R. van Gastel, B. Poelsema, and T. Michely, "Interplay of wrinkles, strain, and lattice parameter in graphene on iridium," *Nano letters* **12** no. 2, (2012) 678–682.

[116] N. J. Couto, D. Costanzo, S. Engels, D.-K. Ki, K. Watanabe, T. Taniguchi, C. Stampfer, F. Guinea, and A. F. Morpurgo, "Random strain fluctuations as dominant disorder source for high-quality on-substrate graphene devices," *Physical Review X* **4** no. 4, (2014) 041019.

[117] A. Fasolino, J. Los, and M. I. Katsnelson, "Intrinsic ripples in graphene," *Nature materials* **6** no. 11, (2007) 858–861.

[118] Y. Park, J. S. Choi, T. Choi, M. J. Lee, Q. Jia, M. Park, H. Lee, and B. H. Park, "Configuration of ripple domains and their topological defects formed under local mechanical stress on hexagonal monolayer graphene," *Scientific reports* **5** (2015) .

[119] V. Lee, C. Park, C. Jaye, D. A. Fischer, Q. Yu, W. Wu, Z. Liu, J. Bao, S. S. Pei, C. Smith, P. Lysaght, and S. Banerjee, "Substrate hybridization and rippling of graphene evidenced by near-edge x-ray absorption fine structure spectroscopy," *The Journal of Physical Chemistry Letters* **1** no. 8, (2010) 1247–1253.

[120] G. X. Ni, Y. Zheng, S. Bae, H. R. Kim, A. Pachoud, Y. S. Kim, C. L. Tan, D. Im, J. H. Ahn, and B. H. Hong, "Quasi-periodic nanoripples in graphene grown by chemical vapor deposition and its impact on charge transport," *ACS nano* **6** no. 2, (2012) 1158–1164.

[121] S. Deng and V. Berry, "Wrinkled, rippled and crumpled graphene: an overview of formation mechanism, electronic properties, and applications," *Materials Today* **19** no. 4, (2016) 197–212.

[122] W. Kohn and L. J. Sham, "Self-consistent equations including exchange and correlation effects," *Physical Review* **140** no. 4A, (1965) A1133.

[123] J. P. Perdew, K. Burke, and M. Ernzerhof, "Generalized gradient approximation made simple," *Physical review letters* **77** no. 18, (1996) 3865.

[124] P. Giannozzi, S. Baroni, N. Bonini, M. Calandra, R. Car, C. Cavazzoni, D. Ceresoli, G. L. Chiarotti, M. Cococcioni, and I. Dabo, "Quantum espresso: a modular and open-source software project for quantum simulations of materials," *Journal of Physics: Condensed Matter* **21** no. 39, (2009) 395502.

[125] A. D. Winter, K. Czanikova, E. Larios, V. Vishniyakov, C. Jaye, D. A. Fischer, M. Omastova, and E. M. Campo, "Interface dynamics in strained polymer nanocomposites: Stick-slip wrapping as a prelude to mechanical backbone twisting derived from sonication-induced amorphization," *The Journal of Physical Chemistry C* **119** (2015) 20091–20099.

[126] J. E. Baio, C. Jaye, D. A. Fischer, and T. Weidner, "Multiplexed orientation and structure analysis by imaging near-edge x-ray absorption fine structure (mosaix) for combinatorial surface science," *Analytical chemistry* **85** no. 9, (2013) 4307–4310.

[127] D. Outka, J. Stöhr, J. Rabe, and J. Swalen, "The orientation of langmuir-blodgett monolayers using nexafs," *The Journal of chemical physics* **88** no. 6, (1988) 4076–4087.

[128] B. J. Schultz, R. V. Dennis, V. Lee, and S. Banerjee, "An electronic structure perspective of graphene interfaces," *Nanoscale* **6** no. 7, (2014) 3444–3466.

[129] J. J. Velasco-Velez, C.-H. Wu, B.-Y. Wang, Y. Sun, Y. Zhang, J.-H. Guo, and M. Salmeron, "Polarized x-ray absorption spectroscopy observation of electronic and structural changes of chemical vapor deposition graphene in contact with water," *The Journal of Physical Chemistry C* **118** no. 44, (2014) 25456–25459.

[130] V. Lee, L. Whittaker, C. Jaye, K. M. Baroudi, D. A. Fischer, and S. Banerjee, "Large-area chemically modified graphene films: electrophoretic deposition and characterization by soft x-ray absorption spectroscopy," *Chemistry of Materials* **21** no. 16, (2009) 3905–3916.

[131] H. Lu, D. Zeysing, M. Kind, A. Terfort, and M. Zharnikov, "Structure of self-assembled monolayers of partially fluorinated alkanethiols with a fluorocarbon part of variable length on gold substrate," *The Journal of Physical Chemistry C* **117** no. 37, (2013) 18967–18979.

[132] S. Frey, V. Stadler, K. Heister, W. Eck, M. Zharnikov, M. Grunze, B. Zeysing, and A. Terfort, "Structure of thioaromatic self-assembled monolayers on gold and silver," *Langmuir* **17** no. 8, (2001) 2408–2415.

[133] H. Peisert, I. Biswas, M. Knupfer, and T. Chassé, "Orientation and electronic properties of phthalocyanines on polycrystalline substrates," *physica status solidi (b)* **246** no. 7, (2009) 1529–1545.

[134] X. Duan, F. Yang, E. Antono, W. Yang, P. Pianetta, S. Ermon, A. Mehta, and Y. Liu, "Unsupervised data mining in nanoscale x-ray spectro-microscopic study of ndfeb magnet," *Scientific Reports* **6** (2016) 34406.

[135] Y. Liu, F. Meirer, P. A. Williams, J. Wang, J. C. Andrews, and P. Pianetta, "Txm-wizard: a program for advanced data collection and evaluation in full-field transmission x-ray microscopy," *Journal of synchrotron radiation* **19** no. 2, (2012) 281–287.

[136] W. Zhu, T. Low, V. Perebeinos, A. A. Bol, Y. Zhu, H. Yan, J. Tersoff, and P. Avouris, "Structure and electronic transport in graphene wrinkles," *Nano letters* **12** no. 7, (2012) 3431–3436.

[137] `https://www.photonics.com/Article.aspx?AID=60862&PID=5&VID=135&IID=893`.

[138] B. Zhan, C. Li, J. Yang, G. Jenkins, W. Huang, and X. Dong, "Graphene field-effect transistor and its application for electronic sensing," *Small* **10** no. 20, (2014) 4042–4065.

[139] P. Avouris, "Graphene: electronic and photonic properties and devices," *Nano letters* **10** no. 11, (2010) 4285–4294.

[140] C. Mattevi, H. Kim, and M. Chhowalla, "A review of chemical vapour deposition of graphene on copper," *Journal of Materials Chemistry* **21** no. 10, (2011) 3324–3334.

[141] W. Jung, D. Kim, M. Lee, S. Kim, J. Kim, and C. Han, "Ultraconformal contact transfer of monolayer graphene on metal to various substrates," *Advanced Materials* **26** no. 37, (2014) 6394–6400.

[142] L. Colombo, R. M. Wallace, and R. S. Ruoff, "Graphene growth and device integration," *Proceedings of the IEEE* **101** no. 7, (2013) 1536–1556.

[143] A. Ambrosi and M. Pumera, "The cvd graphene transfer procedure introduces metallic impurities which alter the graphene electrochemical properties," *Nanoscale* **6** no. 1, (2014) 472–476.

[144] A. D. Winter, E. Larios, C. Jaye, D. A. Fischer, M. Omastov, and E. M. Campo, "Thermo-active polymer nanocomposites: a spectroscopic study," in *SPIE NanoScience+ Engineering*, pp. 917003–917003–7. International Society for Optics and Photonics.

[145] A. D. Winter, C. Jaye, D. Fischer, M. Omastov, and E. M. Campo, "Prestrain relaxation in non-covalently modified ethylene-vinyl acetate — pychol — multiwall carbon nanotube nanocomposites," *APL Materials* **2** no. 6, (2014) 066105.

[146] A. D. Winter, E. Larios, F. M. Alamgir, C. Jaye, D. Fischer, and E. M. Campo, "Near-edge x-ray absorption fine structure studies of electrospun poly (dimethylsiloxane)/poly (methyl methacrylate)/multiwall carbon nanotube composites," *Langmuir* **29** no. 51, (2013) 15822–15830.

[147] A. D. Winter, W. Y. Rojas, A. D. Williams, S. S. Kim, F. Ouchen, D. A. Fischer, C. Weiland, E. Principe, S. Banerjee, and C. Huynh, "Monitoring deformation in graphene through hyperspectral synchrotron spectroscopy to inform fabrication," *The Journal of Physical Chemistry C* **121** no. 29, (2017) 15653–15664.

[148] B. J. Schultz, C. Jaye, P. S. Lysaght, D. A. Fischer, D. Prendergast, and S. Banerjee, "On chemical bonding and electronic structure of graphene-metal contacts," *Chemical Science* **4** no. 1, (2013) 494–502.

[149] J. Sheehy, T. Gil, C. Winstead, R. Farren, and P. Langhoff, "Correlation of molecular valenceand kshell photoionization resonances with bond lengths," *The Journal of chemical physics* **91** no. 3, (1989) 1796–1812.

[150] C. Neumann, S. Reichardt, P. Venezuela, M. Dr͗ogeler, L. Banszerus, M. Schmitz, K. Watanabe, T. Taniguchi, F. Mauri, B. Beschoten, S. V. Rotkin, and C. Stampfer, "Raman spectroscopy as probe of nanometre-scale strain variations in graphene," *Nature Communications* **6** no. 25, (2015) 8429.

[151] Z. Ni, Y. Wang, T. Yu, and Z. Shen, "Raman spectroscopy and imaging of graphene," *Nano Research* **1** no. 4, (2008) 273–291.

[152] Y. Y. Wang, Z. H. Ni, T. Yu, Z. X. Shen, H. M. Wang, Y. H. Wu, W. Chen, and A. T. Shen Wee, "Raman studies of monolayer graphene: the substrate effect," *The Journal of Physical Chemistry C* **112** no. 29, (2008) 10637–10640.

[153] S. Latil and L. Henrard, "Charge carriers in few-layer graphene films," *Physical Review Letters* **97** no. 3, (2006) 036803.

[154] M. Fuentes-Cabrera, M. I. Baskes, A. V. Melechko, and M. L. Simpson, "Bridge structure for the graphene/ni (111) system: a first principles study," *Physical Review B* **77** no. 3, (2008) 035405.

[155] Z. Xu and M. J. Buehler, "Interface structure and mechanics between graphene and metal substrates: a first-principles study," *Journal of Physics: Condensed Matter* **22** no. 48, (2010) 485301.

[156] A. Kasry, M. A. Kuroda, G. J. Martyna, G. S. Tulevski, and A. A. Bol, "Chemical doping of large-area stacked graphene films for use as transparent, conducting electrodes," *ACS nano* **4** no. 7, (2010) 3839–3844.

[157] M. Pedio, A. Giglia, N. Mahne, S. Nannarone, S. Giovannini, C. Cepek, F. Boscherini, R. Carboni, M. Benfatto, and S. Della Longa, "C k-edge nexafs of 6h-sic and 3c-sic systems," *Physica Scripta* **2005** no. T115, (2005) 308.

[158] S. Banerjee, T. Hemraj-Benny, and S. S. Wong, "Covalent surface chemistry of single-walled carbon nanotubes," *Advanced Materials* **17** no. 1, (2005) 17–29.

[159] D. C. Bell, M. C. Lemme, L. A. Stern, J. R. Williams, and C. M. Marcus, "Precision cutting and patterning of graphene with helium ions," *Nanotechnology* **20** no. 45, (2009) 455301.

[160] E. M. Campo, E. Larios, C. Huynh, and M. Ananth, "Helium ion microscopy of electrospun cnt-polymer composites," *Journal of Materials Research* **30** no. 01, (2015) 130–140.

[161] H. Ågren, O. Vahtras, and V. Carravetta, "Near-edge core photoabsorption in polyacenes: model molecules for graphite," *Chemical physics* **196** no. 1-2, (1995) 47–58.

[162] P. A. Brühwiler, A. J. Maxwell, C. Puglia, A. Nilsson, S. Andersson, and N. Mrtensson, "π^* and σ^* excitons in c 1 s absorption of graphite," *Physical review letters* **74** no. 4, (1995) 614.

[163] V. Lee, R. V. Dennis, B. J. Schultz, C. Jaye, D. A. Fischer, and S. Banerjee, "Soft x-ray absorption spectroscopy studies of the electronic structure recovery of graphene oxide upon chemical defunctionalization," *The Journal of Physical Chemistry C* **116** no. 38, (2012) 20591–20599.

[164] R. F. W. Bader, *Atoms in Molecules: A Quantum Theory*. International Ser. of Monogr. on Chem. Clarendon Press, 1994.

[165] P. O. Löwdin, "Quantum theory of many-particle systems. i. physical interpretations by means of density matrices, natural spin-orbitals, and convergence problems in the method of configurational interaction," *Physical Review* **97** no. 6, (1955) 1474.

[166] P. Khomyakov, G. Giovannetti, P. Rusu, G. v. Brocks, J. Van den Brink, and P. Kelly, "First-principles study of the interaction and charge transfer between graphene and metals," *Physical Review B* **79** no. 19, (2009) 195425.

[167] S. Gottardi, K. Müller, L. Bignardi, J. C. Moreno-López, T. A. Pham, O. Ivashenko, M. Yablonskikh, A. Barinov, J. Bjork, and P. Rudolf, "Comparing graphene growth on cu (111) versus oxidized cu (111)," *Nano letters* **15** no. 2, (2015) 917–922.

[168] A. L. Walter, S. Nie, A. Bostwick, K. S. Kim, L. Moreschini, Y. J. Chang, D. Innocenti, K. Horn, K. F. McCarty, and E. Rotenberg, "Electronic structure of graphene on single-crystal copper substrates," *Physical Review B* **84** no. 19, (2011) 195443.

[169] J. Avila, I. Razado, S. Lorcy, R. Fleurier, E. Pichonat, D. Vignaud, X. Wallart, and M. C. Asensio, "Exploring electronic structure of one-atom thick polycrystalline graphene films: A nano angle resolved photoemission study," *Scientific reports* **3** (2013) .

[170] C. Coletti, C. Riedl, D. S. Lee, B. Krauss, L. Patthey, K. von Klitzing, J. H. Smet, and U. Starke, "Charge neutrality and band-gap tuning of epitaxial graphene on sic by molecular doping," *Physical Review B* **81** no. 23, (2010) 235401.

[171] G. Gui, J. Li, and J. Zhong, "Band structure engineering of graphene by strain: first-principles calculations," *Physical Review B* **78** no. 7, (2008) 075435.

[172] T. Olsen, J. Yan, J. J. Mortensen, and K. S. Thygesen, "Dispersive and covalent interactions between graphene and metal surfaces from the random phase approximation," *Physical review letters* **107** no. 15, (2011) 156401.

[173] N. Ferralis, R. Maboudian, and C. Carraro, "Evidence of structural strain in epitaxial graphene layers on 6h-sic (0001)," *Physical review letters* **101** no. 15, (2008) 156801.

[174] S. Chaitoglou and E. Bertrán, "Control of the strain in cvd grown graphene over copper via the h2 flow," *The Journal of Physical Chemistry C* (2016) .

[175] R. He, L. Zhao, N. Petrone, K. S. Kim, M. Roth, J. Hone, P. Kim, A. Pasupathy, and A. Pinczuk, "Large physisorption strain in chemical vapor deposition of graphene on copper substrates," *Nano letters* **12** no. 5, (2012) 2408–2413.

[176] T. Schumann, M. Dubslaff, M. H. Oliveira Jr, M. Hanke, J. M. J. Lopes, and H. Riechert, "Effect of buffer layer coupling on the lattice parameter of epitaxial graphene on sic (0001)," *Physical Review B* **90** no. 4, (2014) 041403.

[177] V. Y. Aristov, G. Urbanik, K. Kummer, D. V. Vyalikh, O. V. Molodtsova, A. B. Preobrajenski, A. A. Zakharov, C. Hess, T. Hanke, and B. Buchner, "Graphene synthesis on cubic sic/si wafers. perspectives for mass production of graphene-based electronic devices," *Nano letters* **10** no. 3, (2010) 992–995.

[178] K. J. Kim, J. Choi, H. Lee, H. K. Lee, T. H. Kang, Y. H. Han, B. C. Lee, S. Kim, and B. Kim, "Effects of 1 mev electron beam irradiation on multilayer graphene grown on 6h-sic (0001)," *The Journal of Physical Chemistry C* **112** no. 34, (2008) 13062–13064.

[179] K. J. Kim, H. Lee, J. Choi, H. Lee, T. Kang, B. Kim, and S. Kim, "Temperature dependent structural changes of graphene layers on 6h-sic (0001) surfaces," *Journal of Physics: Condensed Matter* **20** no. 22, (2008) 225017.

[180] A. Gloter, V. Badjeck, L. Bocher, N. Brun, K. March, M. Marinova, M. Tenc, M. Walls, A. Zobelli, O. Stphan, and C. Colliex, "Atomically resolved mapping of eels fine structures," *Materials Science in Semiconductor Processing* **65** (2017) 2 – 17. Advanced transmission electron microscopy for semiconductor and materials science.

[181] T. Hemraj-Benny, S. Banerjee, S. Sambasivan, M. Balasubramanian, D. Fischer, G. Eres, A. A. Puretzky, D. B. Geohegan, D. H. Lowndes, W. Han, J. A. Misewich, and S. S. Wong, "Near-edge x-ray absorption fine structure spectroscopy as a tool for investigating nanomaterials," *Small* **2** no. 1, (2006) 26–35.

[182] L. R. De Jesus, R. V. Dennis, S. W. Depner, C. Jaye, D. A. Fischer, and S. Banerjee, "Inside and outside: X-ray absorption spectroscopy mapping of chemical domains in graphene oxide," *The Journal of Physical Chemistry Letters* **4** no. 18, (2013) 3144–3151.

[183] M. Amft, S. Lebgue, O. Eriksson, and N. V. Skorodumova, "Adsorption of cu, ag, and au atoms on graphene including van der waals interactions," *Journal of Physics: Condensed Matter* **23** no. 39, 395001.

[184] M. Wu, E. Z. Liu, M. Y. Ge, and J. Z. Jiang, "Stability, electronic, and magnetic behaviors of cu adsorbed graphene: A first-principles study," *Applied Physics Letters* **94** no. 10, (2009) 102505.

[185] F. Banhart, J. Kotakoski, and A. V. Krasheninnikov, "Structural defects in graphene," *ACS Nano* **5** no. 1, (2011) 26–41.

[186] D. Popmintchev, B. R. Galloway, M. C. Chen, F. Dollar, C. A. Mancuso, A. Hankla, L. Miaja Avila, G. O'Neil, J. M. Shaw, G. Fan, S. Ališauskas, G. Andriukaitis, T. Balčiunas, O. D. Mücke, A. Pugzlys, A. Baltuška, H. C. Kapteyn, T. Popmintchev, and M. M. Murnane, "Near- and extended-edge x-ray-absorption fine-structure spectroscopy using ultrafast coherent high-order harmonic supercontinua," *Phys. Rev. Lett.* **120** (2018) 093002.

[187] B. Liu, E. M. Campo, and T. Bossing, "Drosophila embryos as model to assess cellular and developmental toxicity of multi-walled carbon nanotubes (mwcnt) in living organisms," *PLOS ONE* **9** no. 2, (2014) 1–9.

[188] R. V. Dennis, B. J. Schultz, C. Jaye, X. Wang, D. A. Fischer, A. N. Cartwright, and S. Banerjee, "Near-edge x-ray absorption fine structure spectroscopy study of nitrogen incorporation in chemically reduced graphene oxide," *Journal of Vacuum Science & Technology B* **31** no. 4, (2013) 041204.

[189] B. J. Schultz, R. V. Dennis, J. P. Aldinger, C. Jaye, X. Wang, D. A. Fischer, A. N. Cartwright, and S. Banerjee, "X-ray absorption spectroscopy studies of electronic structure recovery and nitrogen local structure upon thermal reduction of graphene oxide in an ammonia environment," *RSC Adv.* **4** (2014) 634–644.